RICE UNIVERSITY

Synthesis, Characterization, and Biological uses of Carbon Nanoparticles

by

Daniela C. Marcano

A THESIS SUBMITTED
IN PARTIAL FULFILLMENT OF THE
REQUIREMENTS FOR THE DEGREE

Doctor of Philosophy

APPROVED, THESIS COMMITTEE

James M. Tour, Chair
T. T. and W. F. Chao Professor of Chemistry, Professor of Mechanical Engineering & Materials Science and Professor of Computer Science

W. E. Billups
Professor of Chemistry

Antonios G. Mikos
Louis Calder Professor of Chemical Engineering, Dir, Ctr for Excellence in Tissue Engr, Dir, J.W. Cox Lab for Biomedical Engineering

HOUSTON, TEXAS
August 2012

ABSTRACT

Synthesis, Characterization, and Biological uses of Carbon Nanoparticles

by

Daniela C. Marcano

This dissertation demonstrates the radical scavenging properties of poly(ethylene glycol)-functionalized hydrophilic carbon clusters (PEG-HCCs, ~50 nm size) *in vitro* and *in vivo*. Also, it describes the new synthesis of improved graphene oxide (IGO, 5-10 μm).

Many diseases have been associated with oxidative stress (OS) which is caused when the production of reactive oxygen species (ROS), such as superoxide ($O_2^{\bullet-}$) and hydroxyl radical ($^{\bullet}OH$), overcome the scavenging efficiency of living organisms. It is known that ROS production is worsened during traumas related to ischemic events and subsequent reperfusion in which the treatment with fast and effective antioxidants is critical to prevent cell and tissue damage. PEG-HCCs are carbon nanoparticles that showed $O_2^{\bullet-}$ and $^{\bullet}OH$ scavenging properties according to electron paramagnetic resonance (EPR) experiments and peroxyl scavenging properties based on oxygen radical absorbance capacity (ORAC) assays. The $O_2^{\bullet-}$ quenching capability was also examined *in vivo* using a mild traumatic brain injury (mTBI) model complicated with hypotension. As result of the PEG-HCCs treatment, the cerebral blood flow (CBF) was restored while normalizing $O_2^{\bullet-}$ and nitric oxide ($NO^{\bullet}$) levels, primarily in the cerebral vasculature.

Presently, Hummers' method ($KMnO_4$, $NaNO_3$, H_2SO_4) is the most common procedure used for preparing graphene oxide. The improved method developed and described in this dissertation is based on the exclusion of $NaNO_3$, an increased amount of $KMnO_4$, and the addition of H_3PO_4 (9:1 mixture of H_2SO_4:H_3PO_4), providing a greater amount of hydrophilic oxidized graphene material as compared to Hummers' method. Even though the GO produced by this new method is more oxidized than that prepared by Hummers' method, when both are reduced in the same chamber with hydrazine, chemically converted graphene (CCG) produced from this new method is equivalent in its electrical conductivity. In contrast to Hummers' method, the new procedure does not generate toxic gas and the temperature is easily controlled. This improved synthesis of GO may be important for large-scale production of GO as well as the construction of devices composed of the subsequent CCG.

Acknowledgments

First and foremost, I want to thank God for all his blessings.

I wish to express my most sincere gratitude to my advisor Dr. James Tour for all his guidance, encouragement, and help throughout my PhD studies and training.

I want to thank Rice University and the Department of Chemistry for giving me the opportunity to learn and develop my scientific skills in their graduate program.

I would like to thank all the graduate students, technicians, post-docs, and collaborators that contributed to this dissertation. Special thanks to Dr. Jacob Berlin, Dr. Thomas Kent, Dr. Dustin James, Dr. Ah-Lim Tsai, Dr. Vladimir Berka, Dr. Robia Pautler, Dr. Brittany Bitner, Dr. David Baskin, Dr. Martyn Sharpe, Dr. Dmitry Kosynkin, Dr. Zhengzong Sun, Dr. Jazmin Godoy, and Dr. Ashley Leonard. My appreciation also extends to all past and current members of the laboratory, whose work has been the inspiration and building blocks of my research. Also, I would like to acknowledge the help and support of my brother, Elio Marcano, and friends Andres Benitez, Claudia Gonzaga, Amir Sánchez, Ricardo Gallardo, Wei Lu, Chih-Chua Hwang, Gabriel Ceriotti, Samuel Loic, Gedeng Ruan, Haiyan Zheng, Polly Rocha, Jeniffer Masy, and Tam Pham.

Last but not least; I would like to thank the rest of my committee members Dr. W. E. Billups and Dr. Antonios Mikos for their help, comments and suggestions to my graduate work.

Contents

List of Figures ……..……...…… ix

**List of Tables ……..…….....…….....…….....

List of Figures

List of Tables

List of Equations

List of Symbols and Abbreviations

AAPH	α, α' -axodiisobutyramidine dihydrochloride
ABTS	2,2'-azino-bis(3-ethylbenzothiazoline-6-sulphonic acid)
AFM	atomic force microscopy
Ar	argon
AUC	area under the curve
BBB	blood brain barrier
BCA	Bicinchoninic acid
b.End.3	murine brain endothelial cells
C	Carbon
°C	degrees Celsius
CBF	cerebral blood flow
CCCP	carbonyl cyanide m-chlorophenyl hydrazone
CCG	chemically converted graphene
CCHG	chemically converted Hummers' graphene
CCHG+	chemically converted modified-Hummers' graphene
CCIG	chemically converted improved graphene
ClO_2	chlorine dioxide
cm	centimeter
cm^{-1}	inverse centimeters
CO	carbon monoxide
CO_2	carbon dioxide
conc	concentration

Cu	copper
$CuSO_4$	copper (II) sulfate
d	day(s)
DCC	*N*,*N*′-dicyclohexylcarbodiimide
DEPMPO	5-(diethoxyphosphoryl)-5-methyl-1-pyrroline N-oxide
DEPMPO-OH	hydroxyl radical spin adduct
DEPMPO-OOH	superoxide radical spin adduct
DFO	deferoxamine
D/G	diamondoid-to-graphitic ratio
DHE	dihydroethidine
DI	deionized water
DMAP	4-(dimethylamino)pyridine
DMEM	Dulbecco's modified Eagle's medium
DMF	*N*,*N*-dimethylformamide
DMSO	dimethyl sulfoxide
Doc	docetaxel
DTPA	diethylene triamine pentaacetic acid
EDTA	ethylenediaminetetraacetic acid
EGF	epidermal growth factor
EGFR	epidermal growth factor receptor
EPR	electron paramagnetic resonance spectroscopy
equiv	equivalent
FBS	fetal bovine serum

FDA	Food and Drug Administration
$FeCl_3$	iron (III) chloride
$FeSO_4$	iron (II) sulfate
FITC	fluorescein isothiocyanate
Fl	fluorescein
g	gram(s)
GBM	glioblastoma multiforme
GFAP	glial fibrillary acidic protein
GI	gastrointestinal
GO	graphene oxide
GONRs	graphene oxide nanoribbons
h	hour(s)
H_2O	water
H_2O_2	hydrogen peroxide
H_2SO_4	sulfuric acid
H_3PO_4	phosphoric acid
HADES	hydrophilic carbon cluster antibody drug enhancement system
HbO_2	oxo-hemoglobin
HCCs	hydrophilic carbon cluster(s)
HCl	hydrochloric acid
HCN	human cortical neurons
HGO	Hummers' graphene oxide
HGO+	modified-Hummers' graphene oxide

HiPco	high pressure carbon monoxide
HNO_3	nitric acid
HPR	HiPco reactor
HRP	horseradish peroxidase
HX	hypoxanthine
ICP	inductively coupled plasma
ICP-OES	inductively coupled plasma optical emission spectrometry
IgG	immunoglobulin G antibodies
IGO	improved graphene oxide
IL-13R	interleukin-13 receptor
In	indium
i.v.	intravenous
K	Kelvin
KH_2PO_4	potassium phosphate monobasic
$KMnO_4$	potassium permanganate
KO_2	potassium superoxide
L	liter(s)
LogP	partition coefficient
μL	microliter
M	molar or moles per liter
μm	micrometer
MeOH	methanol
mequiv	milliequivalent

metHb	methehemoglobin
mg	milligram(s)
min	minute(s)
mL	milliliter
mm	millimeter
MnO_2	manganese dioxide
mol	mole
mTBI	mild traumatic brain injury
MTT	methylthiazolyldiphenyl-tetrazolium bromide
MW	molecular weight
MWCNTs	multi walled carbon nanotubes
MWCO	molecular weight cut off
N	nitrogen
N_2	nitrogen gas
N_2O_4	nitrogen tetroxide
$NaClO_4$	sodium perchlorate
$NaNO_2$	sodium nitrite
$NaNO_3$	sodium nitrate
NaOH	sodium hydroxide
NHA	human astrocytes
nm	nanometer
NO	nitric oxide radical
$NO^{\bullet}$	nitric oxide radical

NO_2	nitro group
O	oxygen
$O_2^{\bullet-}$	superoxide radical
OD	optical density
$^{\bullet}OH$	hydroxyl radical
$ONOO^-$	peroxinitrite
ORAC	oxygen radical absorbance capacity
%	percent
p-SWCNTs	purified single-walled carbon nanotubes
PBN	N-tert-butylnitrone
PBS	phosphate buffered saline
PEG	poly(ethylene glycol)
PEG-HCCs	poly(ethylene glycol)-functionalized hydrophilic carbon cluster
PEG-SOD	poly(ethylene glycol)-functionalized superoxide dismutase
PFA	paraformaldehyde
pH	power of hydrogen
PMMA	poly(methyl methacrylate)
PTFE	polytetrafluoroethylene
PTX	paclitaxel
RBM	radial breathing modes
ROS	reactive oxygen species
rpm	revolutions per minute
rt	room temperature

s	second
SA	sodium salicylate
SAED	selected area electron diffraction
SEM	scanning electron microscope
SiO_2	silica oxide
SO	superoxide radical
SOD	superoxide dismutase
SN-38	7-Ethyl-10-hydroxy-camptothecin
SWCNTs	single-walled carbon nanotube(s)
TBI	traumatic brain injury
TEA	triethanolamine
TEM	transmission electron microscopy
tert-butyl	tertiary butyl group
TGA	thermogravimetric analysis
THF	tertrahydrofuran
TME	trolox mass equivalent
U	enzyme unit (amount of the enzyme that catalyzes the conversion of 1 μmol of substrate/min)
US-SWCNT	ultra-short single-walled carbon nanotube(s)
UV	ultraviolet
Vin	vinblastine
vis	visible
wt	weight

wt%	weight percent
X	xanthine
XO	xanthine oxidase
XPS	X-ray photoelectron spectroscopy
XRD	X-ray diffraction

Chapter 1

Antioxidant efficacy of PEGylated Carbon Particles

1.1. Introduction

It has been reported that approximately 5% of inhaled oxygen is metabolized by cells and converted to reactive oxygen species (ROS) such as superoxide ($O_2^{\bullet-}$), hydrogen peroxide (H_2O_2) and organic peroxides, and hydroxyl radical ($^{\bullet}OH$).[1,2] These ROS are necessary for the signaling pathways in biological processes[3,4] such as cell migration, circadian rhythm, stem cell proliferation, and neurogenesis.[5] In healthy systems, the ROS are efficiently removed by the defensive enzymes superoxide dismutase (SOD), catalase, and antioxidants like glutathione, vitamin A, ascorbic acid, uric acid, hydroquinones, and vitamin E.[6] When the production of ROS overwhelms the scavenging ability of the defense system, oxidative stress occurs, causing dysfunctions in cell metabolism. Additionally, the ROS-induced oxidation of macromolecules such as lipoproteins, DNA

and RNA, compromises cellular integrity.[7,8] It is still uncertain whether the uncontrolled generation of ROS is the cause or a consequence of several diseases[9] but the oxidative stress that they cause has been associated with cardiovascular dysfunction,[10,11] cancer,[12,13] rheumatoid arthritis,[14,15] inflammatory response,[16] diabetes,[17] aging,[18] and neurodegenerative[19] conditions including Alzheimer's disease[20,21] and Parkinson's disease.[21] The overproduction of ROS is also observed in injuries caused by ischemia and blood reperfusion, heat, trauma, freezing, severe exercise, toxins, radiation and infection pathologies.[2]

In cells, $O_2^{\bullet-}$ is generated by different oxidases including xanthine oxidase (XO) and NADPH oxidases. H_2O_2, which is produced by oxidases or by the SOD-assisted dismutation of $O_2^{\bullet-}$, is a long lived, membrane permeable molecule, able to migrate away from the site of production.[2] The problem begins when H_2O_2 interacts with transition metals such as copper and/or iron released from metalloproteins during ischemic pathologies, to produce $^{\bullet}OH$ (the Fenton reaction).[22] In addition to ROS, reactive nitrogen species (RNS) such as nitric oxide ($NO^{\bullet}$), nitrogen dioxide, and dinitrogen trioxide are present in all organisms. $NO^{\bullet}$ is an important molecule produced by nitric oxide synthase (NOS) enzymes.[23] It is involved in neurotransmission, blood pressure regulation, smooth muscle relaxation and immune regulation processes. During an inflammatory event, the production of $O_2^{\bullet-}$ and $NO^{\bullet}$ is triggered, and under these conditions, both radicals may react to produce peroxynitrite ($ONOO^-$), a very potent oxidizing molecule which causes protein nitration and DNA fragmentation.[9]

One way to treat these detrimental pathologies is by supplying antioxidant molecules or particles that rebalance the disturbed oxidative condition.[3] We recently developed a biocompatible carbon particle, the PEGylated hydrophilic carbon cluster (PEG-HCC)[24] that has shown the ability to scavenge oxyradicals[25] due to its graphitic domains. These PEG-HCCs are about 50 nm in size and are 85% PEG by weight.[24,26] It has been reported that PEG chains can interact with $^{\bullet}OH$ primarily through H abstraction ($k = 2.4 \times 10^8\ M^{-1}s^{-1}$).[27] PEG chains also have the ability to sequester transition metal ions which are responsible for the Fenton reaction. Hence, there is a question whether the antioxidant activity of the PEG-HCCs is primarily due to the PEG addends where they act as pre-antioxidants by trapping metal ions and/or they interact with $^{\bullet}OH$. In this work, we evaluated the $^{\bullet}OH$, $O_2^{\bullet-}$, $NO^{\bullet}$, and $ONOO^-$ scavenging properties of PEG-HCCs using electron paramagnetic spectroscopy (EPR), oxy-hemoglobin, cytochrome c, and pyrogallol red decomposition assays to elucidate the mechanisms by which PEG-HCCs might inhibit ROS.

1.2. Experimental Procedures

5-(Dietoxyphosphoryl)-5-methylpyrrole-N-oxide (DEPMPO) was obtained from Santa Cruz Labs (cat # sc-202132). Ferrous sulfate heptahydrate ($FeSO_4 \cdot 7\ H_2O$, cat # M1-03965-0500), cupric sulfate pentahydrate ($CuSO_4 \cdot 5H_2O$, cat # C493-500), nitric acid (HNO_3, cat #A200-212), H_2O_2 (30% in water, cat # MHX06351), potassium phosphate monobasic (KH_2PO_4, cat # P284-500), potassium permanganate ($KMnO_4$, cat # P279-

500), ethanol (EtOH, cat # 04-355-222), sulfuric acid (H_2SO_4, cat # A300-212), and sodium hydroxide (NaOH, cat # S318) were purchased from Fisher Scientific. Potassium phosphate dibasic (K_2HPO_4, cat # 3252-01) was purchased from J. T Baker. Methoxypolyethylene glycol amine (PEG, cat # 06679, MW 5000), Chelex (Cat # C7901), ethylenediaminetetraacetic acid tetrasodium salt hydrate (EDTA, cat # E5391), catalase from bovine liver (cat # C40), triethanolamine (TEA, cat # 90279), methylsulfoxide (DMSO, cat # W387509), sodium perchlorate ($NaClO_4$, cat # 410241), horseradish peroxidase (HRP, cat # P8375), deferoxamine mesylate (DFO, cat # D9533), 2,2'-azino-bis(3-ethylbenzothiazoline-6-sulfonic acid) diammonium salt (ABTS, cat # A9941), pyrogallol (cat # P0381), sodium nitrite ($NaNO_2$, cat # 237213), ascorbic acid (acid form, cat # A7506), caffeic acid (cat # C0625), (±)-6-hydroxy-2,5,7,8-tetramethylchromane-2-carboxylic acid (trolox, cat # 238813), hypoxanthine (HX, cat # H9636), cytochrome *c* from equine heart (cat # C4186), xanthine oxidase (XO, cat # X4875), and superoxide dismutase (SOD, cat # S9697) were purchased from Sigma-Aldrich. Potassium superoxide (KO_2, cat # 355420250) was obtained from Acros Organics. The inductively couple plasma (ICP) standard for iron (cat # ICP-AM-6) and the dialysis membrane (MWCO 1000 and MWCO 5000) were purchased from High-purity standards and Biotech respectively.

PEG-HCCs were prepared, purified, and characterized as reported previously.[24] Briefly, HCCs were prepared from single-walled carbon nanotubes (SWCNTs), which are 1 nm wide and have a high solubility in oleum (400 ppm), by an oxidative procedure in which oleum and nitric acid mixture was employed. The SWCNTs (250 mg) were dissolved in oleum (125 mL) in a three-neck, 1 L round-bottomed flask with all joints

sealed with Teflon and stirred for 5 days to disentangle them. The solution was then cooled to 0 °C with an ice bath, and an ice cold 1:1 mixture of oleum and nitric acid (62.5 mL/62.5 mL) was added in 20 mL portions. During the addition of this mixture, the temperature of the solution was monitored to ensure that it never exceeded 60°C. When 60 °C was reached, the mixture was allowed to cool until the temperature returned to 10 °C before adding the next portion. The addition process took approximately 1 h. The final proportion of oleum/nitric acid was 3:1. When the addition of the acidic mixture was completed, the ice bath was removed and the solution was heated to 65 °C and stirred for 90 min. The solution was then cooled to room temperature and carefully poured onto ice (400 mL) to quench the reaction. The resulting solution was filtered through a PTFE membrane (0.45 μm pore size). The pH of the liquid coming through the filter is checked until it reaches pH 6. At this point, the addition of water is terminated and all of the liquid is removed by filtration, but the solid still remains moist. Methanol (150 mL) is slowly added to dissolve the solid, then ether (500 mL) is added to precipitate the solid and the liquid is removed by filtration. The final evaporation of the ether was done by placing the moist HCCs in a 50 mL beaker and using a hot plate, slowly allowing the HCCs to heat while continually pulverizing them with a Teflon spatula resulting in a fine, dry powder that was dried in a vacuum desiccator for 12 h to yield 112 mg of HCCs. PEG-HCCs were prepared by coupling 5,000 MW methoxy(polyethylene glycol) amine (PEG) to the carboxylic acids on the HCCs. In general, HCCs (25 mg, 2.08 mmol of carbon) were added to DMF (25 mL), and the mixture was bath sonicated for 30 min until all of the HCCs were dissolved. DCC (172 mg, 0.835 mmol), DMAP (2 flakes), and PEG (208 mg, 0.042 mmol) were added and stirred for 24 h. The solution was purified by dialysis

in DMF and then water (50,000 MW cutoff dialysis bag, Membrane Filtration Products, Inc.), followed by passage through a PD-10 column(GE Healthcare) and rotavap to furnish 40 mL of PEG-HCCs with a carbon core concentration of 0.500 mg/mL (Figure A1, Appendix A). The nanoparticle concentration was estimated based on the carbon core absorbance at 763 nm using an extinction coefficient of 0.01040 L/mg. This wavelength was not used for biological assays. Thermogravimetric analysis (TGA) showed an 84% weight loss (100 – 850 ºC at 5 ºC/min rate under Ar). The pronounced weight loss at 400 ºC (70%) corresponded to the C-O functionalities of the PEG. The presence of carbon-carbon double bonds from the PEG-HCC core was confirmed by the peak at 284.5 eV in the C(1s) region of the X-ray photoelectron spectrum (XPS). The strong signal at 286.0 eV corresponded to the C-O bonds of the PEG chains. The Raman spectrum of the PEG-HCCs clearly showed the G peak at ~1560 cm^{-1} which is associated with the planar configuration of sp^2 bonded carbon in the graphitic domains of the PEG-HCCs core. Dynamic light scattering (DLS) measurements showed that a neutral pH the PEG-HCCs were 60 ± 0.8 nm in size (Figure 1A, Appendix A).

Samples were analyzed for ROS scavenging effect following EPR and spectrophotometric assays described below.

1.2.1. $O_2^{\bullet-}$ Scavenging Assay

To analyze the $O_2^{\bullet-}$ scavenging property, the following reagents were mixed in a 2 mL microcentrifuge tube: potassium phosphate buffer (PBS, 50 mM, supplemented with 0.1 mM EDTA and 200 U/mL catalase;[28] DEPMPO (20 mM); either PEG-HCCs (0.07 mg/mL), PEG (0.07 mg/mL) or water; then KO_2 dissolved in DMSO (~3.0 mM). The

final concentration of each reagent is indicated in parentheses. KO_2/DMSO was prepared following a modified reported procedure.[29,30] Briefly, 5 g of KO_2 was suspended in 5 mL of anhydrous DMSO, stirred for 15 min, then centrifuged for 1 min. The supernatant phase contained the dissolved KO_2. This procedure was repeated every 2 h and a quality control sample was taken every three runs in order to evaluate the decomposition of the KO_2 mixture. Time = 0 was set as the time at which KO_2 was added since it is the radical generator. Subsequently, the mixture was transferred to a capillary tube, sealed with Critoseal, and placed it in the EPR instrument. Due to the time required for sample transfer to the capillary tube and then to the EPR cavity, the earliest that the EPR spectrum could record was at 70 s. EPR measurements were recorded in a Bruker EMX spectrometer using the following parameters: 3315 G as center field, 200 G sweep width, microwave frequency 9.3 GHz, microwave power 40 mW, receiver gain 6.32×10^5, modulation frequency 100 KHz, modulation amplitude 0.50 G, signal channel conversion 163.8 ms, time constant 327.7 ms, and sweep time 167.8 s.

1.2.2. $^{\bullet}$OH Scavenging Assay

To measure the $^{\bullet}$OH scavenging property, the following reagents were mixed in a 2 mL microcentrifuge tube: PBS (50 mM, pre-treated with Chelex 100); DEPMPO (3.53 mM); $FeSO_4 \cdot 7\ H_2O$ (2.94 mM); either PEG-HCCs (0.06 mg/mL), PEG (0.06 mg/mL) or water; then the H_2O_2 (3.53 mM). The final concentration of each reagent is indicated in parentheses. Time = 0 was set as the time at which H_2O_2 was added, since it is the initiator of the reaction. Subsequently, the mixture was transferred to a capillary tube, sealed with Critoseal, and placed it in the EPR instrument. Due to the time required for

sample transfer to the capillary tube and then to the EPR cavity; the earliest that the EPR spectrum could be recorded was at 90 s. The concentration of Fe^{2+} also affects radical production, therefore several samples with different concentrations of the Fe^{2+} were run in order to select the concentration that produced the best EPR signal at 90 s. All EPR spectra obtained in this section were recorded using the same instrument, using the following parameters: 3315 G as center field, 200 G sweep width, microwave frequency 9.3 GHz, microwave power 20 mW, receiver gain 7.1×10^4, modulation frequency 100 KHz, modulation amplitude 0.50 G, signal channel conversion 163.8 ms, time constant 327.7 ms, and sweep time 167.8 s.

1.2.3. Spin Concentration Using Copper Standard

Five different batches of PEG-HCCs (0.05 mg/mL) were frozen in small glass tubes using liquid nitrogen. The EPR spectra of the five samples and a $CuSO_4$ (1 mM) standard solution were recorded at low temperature using the following parameters: 3310 G as center field, 2000 G sweep width, microwave frequency 9.3 GHz, microwave power 1 mW, receiver gain 7.1×10^3, modulation frequency 100 KHz, modulation amplitude 1.0 G. Since the copper standard and the PEG-HCCs solutions were recorded under the same conditions, no corrections were necessary. The copper standard solution was supplemented with EDTA (10 mM) and $NaClO_4$ (100 mM) to make a homogeneous Cu-EDTA tetrahedral copper complex and uniform structure when frozen.

1.2.4. Chelation Assay

PEG-HCCs (0.120 mg/mL) were stirred with $FeSO_4$ (5.88 mM) for 3 h. The ratio between the PEG-HCCs and the $FeSO_4$ were chosen based on the proportion that was used for EPR experiments. Then, the samples were dialyzed using a constant flow of DI water and a cellulose membrane (MWCO 5000 and MWCO 1000) for 48 h. Finally, samples were diluted 5× in 1% HNO_3, sterile-filtered using a 0.20 μm pore size membrane, and analyzed by inductively coupled plasma optical emission spectrometry (ICP-OES).

1.2.5. Oxidation of ABTS by H_2O_2 catalyzed by HRP

The ratios between H_2O_2 and PEG-HCCs for this experiment were based on the EPR experiments in which the Fenton reaction was used. ABTS (0.900 mM) was prepared in a citrate-phosphate buffer pH 5. H_2O_2 (0.300 mM), HRP (50 μg/mL) and PEG-HCCs (0.024 mg/mL) were prepared in PBS pH 7.4. H_2O_2, PEG-HCCs or PBS (control), and ABTS co-substrate were incubated for 10 min at room temperature. Then, the HRP solution was added in order to catalyze ABTS oxidation. The increase in the absorbance at 414 nm[31] due to the $ABTS^{\bullet+}$ radical cation formation was monitored using a TECAN M-1000 plate reader. The experiment was run in triplicate in a 96 well-plate.

1.2.6. $NO^{\bullet}$ Scavenging Assay

Oxyhemoglobin (HbO_2; Fe^{+2}, 8 μM based on heme content, ε_{425nm}=125 M^{-1} s^{-1})[32] was dissolved in TEA buffer (50 mM, pH 7.5). The $NO^{\bullet}$ solution was prepared by bubbling NaOH trap-purified 99.9% pure $NO^{\bullet}$ gas (Matheson), through 10 mL of anaerobic TEA (50 mM, pH 7.5) for 10 min. A ~2 mM solution of $NO^{\bullet}$ was obtained and

kept in a glass tonometer.[33] The HbO_2 and the PEG-HCCs were mixed in the quartz cuvette before initiating the reaction with the addition of the $NO^{\bullet}$. Therefore, if the PEG-HCCs react with the $NO^{\bullet}$ the absorbance difference of the reaction mixture will be lower than the control without PEG-HCCs because they would be preventing the formation of methemoglobin (metHb; Fe^{+3}) by competing with HbO_2 for $NO^{\bullet}$. The α (570 nm) and β (536 nm) peaks are hallmarks for control-HbO_2 rather than metHb. Final metHb concentration was 9.7 ± 0.3 μM ($\varepsilon_{401\text{-}411nm}$ = 38 $mM^{-1}cm^{-1}$),[32] and 0.02 mg/mL of both PEG-HCCs and PEG. The UV spectra were measured using a Hewlett-Packard diode array spectrophotometer model 8452.

1.2.6.1. Anaerobic Sequential Stopped-Flow – Pre-Incubation of the $NO^{\bullet}$ with PEG-HCCs

$NO^{\bullet}$ radicals were incubated with the PEG-HCCs at three different aging time before mixing with HbO_2 using the sequential mode of an Applied Photophysics model SX-18MV stopped flow instrument with rapid-scan diode array accessory. The instrument was located inside an anaerobic chamber model 110 V equipped with a gas analyzer model 10 (Coy Laboratory Products) for tracking the H_2 and O_2 levels. The chamber was filled with 10% H_2 in N_2.[34] The following stock solutions were prepared using TEA (50 mM, pH 7.4): PEG-HCCs (0.08 mg/mL) in aerobic buffer, $NO^{\bullet}$ (20 μM) in anaerobic buffer and HbO_2 (15 μM) in air-saturated buffer. Either buffer (control) or PEG-HCCs were incubated with $NO^{\bullet}$ in a 1:1 ratio for 20 ms, 1 s, or 1 min in the aging loop after first mixing. This solution was then further mixed with HbO_2 in a 1:1 ratio in the detector chamber. Note that 0.04 mg/mL was the concentration of the PEG-HCCs

when it was incubated with $NO^{\bullet}$, and 0.02 mg/mL when it was mixed with HbO_2, thus an overall 4× dilution after two-stage mixing.

1.2.7. Cytochrome c Assay

The $O_2^{\bullet-}$ scavenging efficiency was also determined using the method described by Quick *et al*.[35] Briefly, three reaction solutions were prepared, A-C. Solution A contained catalase (320 μL; 6000 U/mL), HX (320 μL; 10 mM solution in 30 mM NaOH), cytochrome *c* (755 μL; 1.95 mM solution in PBS), and 14.6 mL of PBS. Solution B consisted of XO (57 μL; 167.5 mU/mL in PBS) and PBS (743 μL). Additional B solutions were prepared with PEG-HCCs, replacing the PBS in volumes ranging from 1-743 μL. All solution B preparations were 800 μL, enough solution to run four replicates of each PEG-HCC concentration. Solution C included XO (57 μL; 167.5 mU/mL in PBS), SOD (90 μL; 10200 U/mL in PBS), and PBS (653 μL) to allow determination of non- $O_2^{\bullet-}$-dependent reduction of cytochrome c (total volume 800 μL). The assay was performed in a 96-well plate with a final reaction volume of 325 μL per well. Each plate contained samples with the following conditions, using four wells for each condition: (1) a water blank (325 μL per well), (2) solution B *without* PEG-HCCs (the control reaction; 162.5 μL per well), (3) solution B *with* the PEG-HCCs (162.5 μL per well), and (4) solution C, containing SOD (162.5 μL per well). After all of the above solutions have been added to the plate, 162.5 μL of solution A was rapidly added to each well except for the water blanks. 2 min after the addition of solution A, a BIO-TEK Powerwave XS spectrophotometer (Winooski, VT) supported by SOFTmax Pro software (Molecular Devices, Sunnyvale, CA) was used to read the plate at 550 nm on a basic

kinetic protocol to measure absorbance every 45 s, for a total reaction time of 8 min. The reaction rate (OD/min) was determined and then plotted against the log of the concentration of the test compound. IC_{50} was determined using a nonlinear regression analysis (GraphPad Prism software version 5.0, La Jolla, CA).

1.2.8. $ONOO^-$ Scavenging Assay

Manganese dioxide (MnO_2) was prepared by dissolving 8 g of $KMnO_4$ in 50 mL water, forming a purple solution. 500 mL of 95% EtOH was slowly added, turning the mixture brown. The reaction was stirred overnight then vacuum filtered. The dark brown precipitate was washed with water and allowed to dry for several d.[36] Separately, a 125 mL aqueous solution containing 4 g $NaNO_2$ was added to a 125 mL aqueous solution containing 7.5 mL 35% H_2O_2 and 2 mL 96% H_2SO_4. This mixture was immediately poured into 250 mL solution containing 12.5 g NaOH. To remove unreacted H_2O_2, MnO_2 was added to the final mixture and allowed to stand for 15 min. The concentration of $ONOO^-$ was determined to be 1.73 mM using the absorbance maximum at 302 nm (ε = 1670 M^{-1} cm^{-1}). $ONOO^-$ was portioned into 1.5 mL aliquots and frozen; during use, the $ONOO^-$ was kept on ice. Solutions of antioxidants (ascorbic acid, caffeic acid, PEG-HCCs, trolox) were prepared at 0.100 mg/mL in phosphate buffer. Pyrogallol red was prepared at 5 mM in phosphate buffer. Assays were done in methacrylate cuvettes. Typically, 25 µL of pyrogallol red stock solution was added to the cuvette, followed by phosphate buffer, antioxidant (10, 30, 50, 100 or 200 µL) and finally $ONOO^-$ (the final volume was 1.5 mL). The cuvette was inverted several times after the addition of the $ONOO^-$. The absorbance spectrum from 300 – 700 nm was measured. Each assay was

carried out in triplicate. Control samples were the pyrogallol red in the absence of antioxidant and $ONOO^-$, as well as pyrogallol red in the presence of $ONOO^-$ without antioxidant. The absorbance change at 540 nm ($\varepsilon = 2.4 \times 10^4\ M^{-1}\ cm^{-1}$) was used in inhibition calculations.[36-38]

1.3. Results and Discussion

In order to evaluate the scavenging capacity of the PEG-HCCs, EPR experiments were done using DEPMPO as a spin trap. DEPMPO forms stable adducts upon reaction with $^{\bullet}OH$[3,4,39,40] and $O_2^{\bullet-}$.[6,41,42] $O_2^{\bullet-}$ will be generated using KO_2 in DMSO[30] and the $^{\bullet}OH$ radicals will be generated by the Fenton reaction. The short lifetime of these radicals makes them undetectable at physiological conditions. However, reaction with a spin trap such as DEPMPO produces a relatively stable paramagnetic adduct that is spin active at room temperature.[39,43] It was postulated that if the PEG-HCCs scavenge these radicals, the signal of the spin-adduct should be less intense when the PEG-HCCs are present. As this system was based on a competition reaction between the spin trap and the PEG-HCCs, and the $^{\bullet}OH$ and $O_2^{\bullet-}$ radicals have a very short life time; the spin trap must be present with the PEG-HCCs before the initiation of the reaction. In the case of $O_2^{\bullet-}$, the buffer was supplemented with catalase to prevent the formation of $^{\bullet}OH$ due to the reaction between H_2O_2 and traces of iron from the buffer.

Figure 1.1 shows that the EPR amplitudes of the PEG-HCCs-treated systems were the lowest. This outcome can be explained in two ways: the PEG-HCCs could be

interacting with the radicals under study, or the radical-spin trap reaction could be uninhibited and the PEG-HCCs are interacting with the formed spin adduct. In order to rule out the second possibility, further experiments were performed. Notably, a peak ~3315 G was detected that came from the PEG-HCCs during the $O_2^{\bullet-}$ scavenging experiments. The stability of the PEG-HCCs EPR signal will be also discussed later in this chapter. In order to compare the spin-adduct amplitudes associated with the $O_2^{\bullet-}$ scavenging, the EPR signal of the PEG-HCCs-treated system was corrected by subtracting the signal obtained from the PEG-HCCs alone (Figure A2, Appendix A).

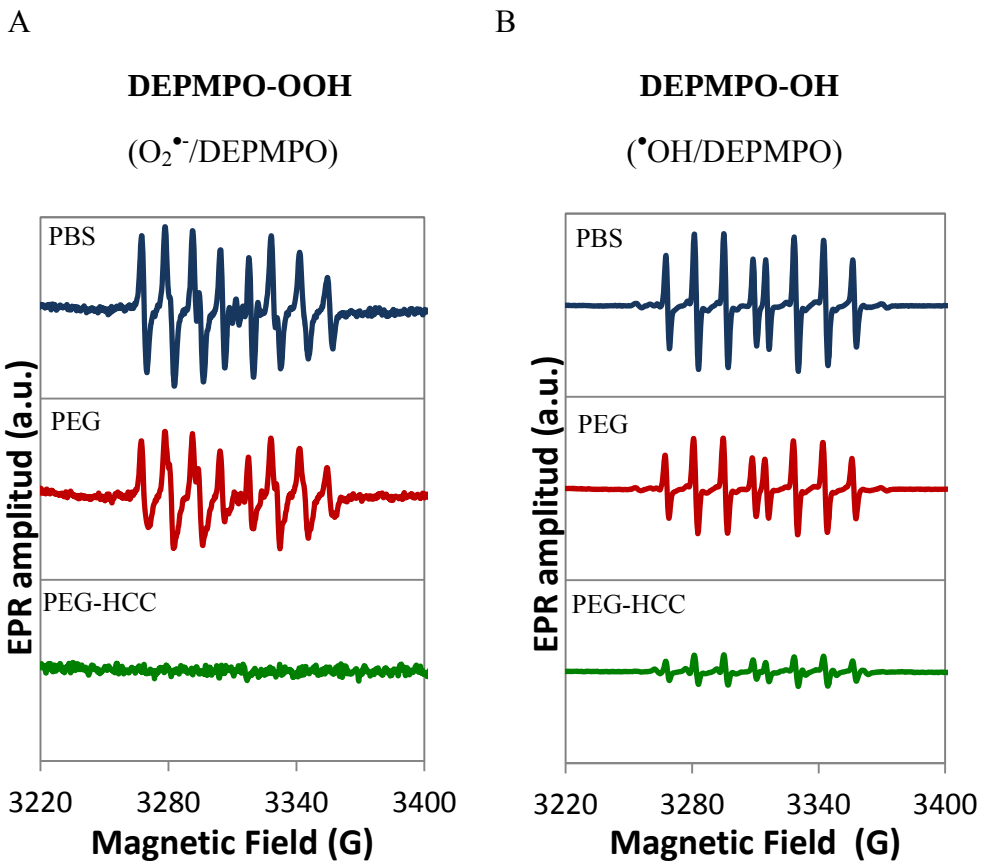

Figure 1.1. EPR spectra at pH 7.4 and room temperature corresponding to the $O_2^{\bullet-}$ and $^{\bullet}OH$ experiments. (A) EPR spectra obtained from the $O_2^{\bullet-}$ system or DEPMPO-OOH adduct. Spectra were recorded after 70 s of the KO_2 addition. PEG-HCCs spectrum was corrected by subtracting the signals of the PEG-HCCs alone (Figure A2, Appendix A). (B) EPR spectra obtained from the $^{\bullet}OH$ system or DEPMPO-OH. Spectra were recorded after 90 s of the H_2O_2 addition. No correction was necessary for the $^{\bullet}OH$ scavenging experiments.

The possible interaction between the PEG or PEG-HCCs with the spin-adduct was studied by adding them 10 s after the addition of KO_2 or 20 s after the addition of H_2O_2. If either PEG or the PEG-HCCs are reacting with the spin-adduct, then a drop in the signal would be observed with respect to the signal of the PBS addition sample (control) at the corresponding experiment.

As Figure 1.2 shows, there was no reduction in the signal and, therefore, no interaction between the PEG-HCCs and the adduct nor PEG and the adduct. In fact, for the $O_2^{\bullet-}$ experiments, there was a small increase in the signal intensity when the PEG and the PEG-HCCs were used. One plausible explanation was that the PEG-HCCs delayed the decomposition of the DEPMPO-OOH adduct. No signal related to DEPMPO-OOH adduct formation was observed when DEPMPO and PEG-HCCs were mixed in the presence of buffer and pure DMSO (Figure A3, Table A1, Appendix A), and so it can be concluded that the signal enhancement was not a result of the formation of $O_2^{\bullet-}$ by the PEG-HCCs or PEG under these conditions. The decomposition of DEPMPO-OH was

tracked for 30 min (Figure A5 and Figure A6, Appendix A). The results verified that neither the PEG nor PEG-HCCs promote decomposition of the DEPMPO-OH.

The spin trap, DEPMPO, was mixed with the all the reagents that were used for both $O_2^{\bullet-}$ and $^{\bullet}OH$ scavenging experiments and the EPR spectra was recorded with the purpose of verifying whether there was any significant signal that could affect the results (Table A1, Table A2, Figure A3, and Figure A7; Appendix A). Remarkably, a peak ~3315 G was detected that came from the PEG-HCCs (the DEPMPO-OOH adduct does not have any signal at this magnetic field strength). This peak was not observed during the $^{\bullet}OH$ radical evaluation because the microwave power and the receiver gain were lower (Figure A2 and Figure A8, Appendix A). Using a copper standard solution, it was determined that ~12% of the PEG-HCCs contain unpaired electrons. This value was obtained based on 5 different batches of PEG-HCCs, including batches that were 3 months old; this indicates that they are exceedingly stable. The stability of the PEG-HCC EPR signal was followed at different concentrations and pHs at room temperature. A citrate buffer (50 mM, pH 4) was used for acidic conditions, PBS (50 mM, pH 7.4) for physiological conditions, and sodium borate buffer (50 mM, pH 9) for basic conditions. Time = 0 was set as the moment that the PEG-HCCs were mixed with the buffers. The EPR signal of the PEG-HCCs was stable after 5 h at physiological pH and pH 9. At pH 4, the EPR signal started decreasing (Figure A8, Appendix A).

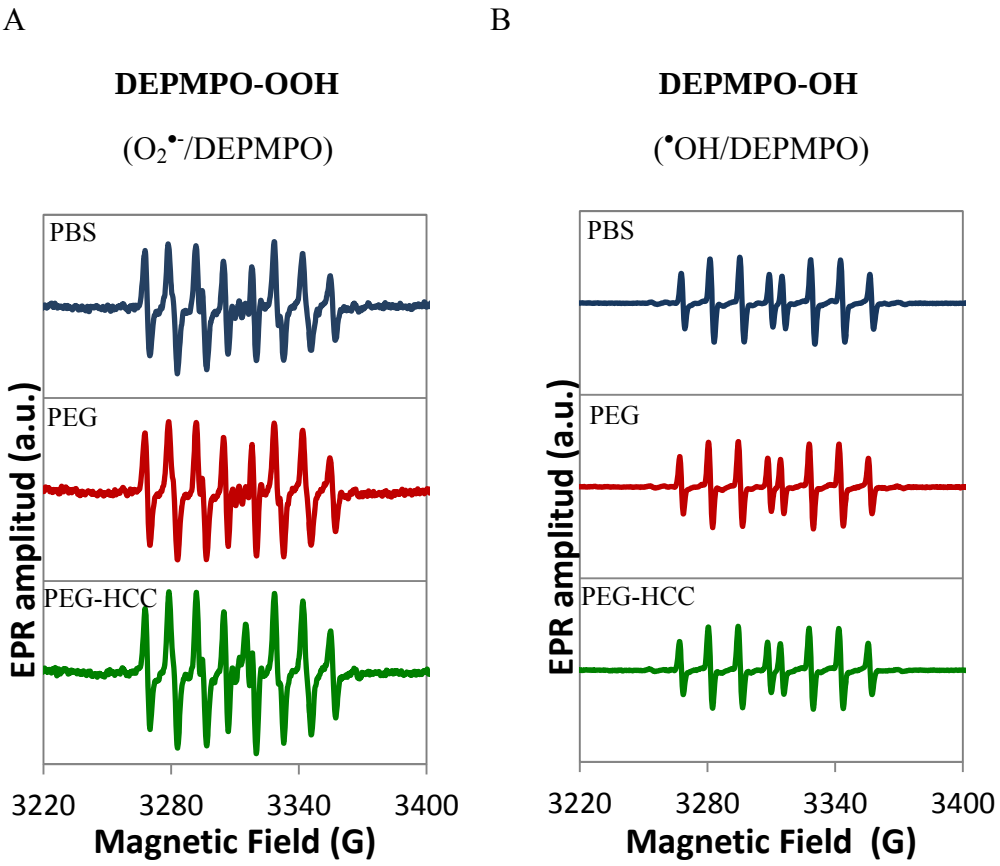

Figure 1.2. EPR spectra obtained when PBS, PEG or PEG-HCCs were added after the DEPMPO-OOH (A) or DEPMPO-OH (B) adducts formed. (A) EPR spectra obtained from the $O_2^{\bullet-}$ system or DEPMPO-OOH adduct. (B) EPR spectra obtained from the $^{\bullet}$OH system or DEPMPO-OH adduct. No corrections were performed for any of the spectra.

The $O_2^{\bullet-}$ specificity[44] of the assay was confirmed by SOD, which is a fast enzyme to disproportionate $O_2^{\bullet-}$ to H_2O_2 and O_2.[45,46] The same procedure, as was used for the previous experiments, was followed but instead of adding the PEG-HCCs, SOD was

added. As expected, dismutation of the $O_2^{\bullet-}$ was signaled by a decrease in the intensity of the 8-hyperfine line pattern of the adduct (Figure 1.3).

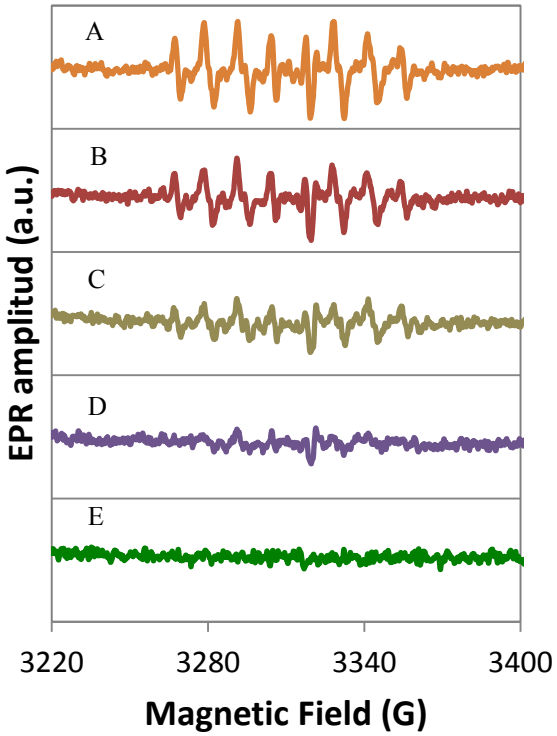

Figure 1.3. EPR spectra of the samples treated with SOD instead of the PEG-HCCs. The dismutation of the $O_2^{\bullet-}$ radicals is being catalyzed by SOD causing a signal drop. (A) SOD 0.01 U/mL (B) SOD 0.10 U/mL (C) 1.00 U/mL (D) SOD 10.00 U/mL (E) PEG-HCCs (0.07 mg/mL, which is the same concentration used in Figure 1.1A). Spectrum E was corrected by subtracting the EPR signal of the PEG-HCCs (Figure A4, Appendix A).

Comparison of the spectra shows that PEG-HCCs have a quenching effect similar to that of 10.0 U/mL SOD. Since the concentration of the PEG-HCCs was 0.07 mg/mL,

the value for the quenching effect was 10.0 U/0.07 mg of PEG-HCCs. This value is similar to the total SOD activity value found in the entire rat brain, which is 13 U/mg of protein,[35] and is higher than the SOD activity value reported for post-mortem human spinal cord, which is between 4-6 U/mg protein.[35] It is noteworthy that similar SOD activity was achieved using 70 μg of PEG-HCCs or in other words 143 U/mg of the PEG-HCCs.

The antioxidant capacity of the PEG-HCCs was evaluated based on the EPR amplitude.[6] Using the EPR amplitude located at 3278 G (the 2nd peak from the far left) for the $O_2^{\bullet-}$ system and 3308 G (the 4th peak from left to right) for the $^{\bullet}OH$ system, PEG-HCCs showed antioxidant activity of about 98% and 73% (Table 1) against $O_2^{\bullet-}$ and $^{\bullet}OH$ radicals, respectively. $O_2^{\bullet-}$ is immediately produced when KO_2 is added to the aqueous media, and it was concluded that the quenching effect was due to the direct reaction between the $O_2^{\bullet-}$ radicals and DEPMPO. For this reason, the *k* value related to the reaction between the PEG-HCCs and $O_2^{\bullet-}$ must be higher than 0.53 $M^{-1}s^{-1}$,[47] which is the *k* value associated with DEPMPO-OOH formation. However, in the case of the $^{\bullet}OH$ studies, two more considerations have to be studied: the PEG-HCCs may interact with iron or with H_2O_2, thereby preventing or decreasing the formation of $^{\bullet}OH$.

Table 1. Relative % of antioxidant activity calculated from [% = ((Control amplitude – PEG-HCCs or PEG amplitude)/Control amplitude) ×100 %].

		Average of the EPR amplitude[a]	Standard deviation	Standard error	Relative % of antioxidant activity
$O_2^{\bullet-}$	**Control**	28782	3833	2213	NA
	PEG	23774	6408	3700	13 ± 30[c]
	PEG-HCCs[b]	433	320	185	98 ± 16[c]
$^{\bullet}OH$	**Control**	15242	3594	2075	NA
	PEG[d]	12277	1488	1052	19 ± 5[c]
	PEG-HCCs	4165	499	288	73 ± 20[c]

Experiments were carried out in triplicate. Quality control sample was run every three samples. [a]EPR amplitude of the signal at 3278 G and 3308 G for the $O_2^{\bullet-}$ and $^{\bullet}OH$ scavenging experiments, respectively. [b]Absolute value. [c]Error propagation from arithmetic calculations using standard deviations. [d]Experiment ran by duplicate.

Iron chelation could be the mechanism that explains the antioxidant properties of the PEG-HCCs in the $^{\bullet}OH$ scavenging experiments. Previously, the chelation or trapping ability of the PEG-HCCs was studied by two reported chelation assays: the ascorbic acid and the benzoate hydroxylation assay[25] (Chapter 2). The ascorbate oxidation assay is based on the reduction of Fe^{3+} by ascorbic acid. The benzoate hydroxylation assay involves preventing the hydroxylation of the substrate by chelating iron, and therefore affecting the Fenton reaction. It was found that the PEG-HCCs oxidized ascorbic acid without any metal assistance, an indication of the oxidant properties of the PEG-HCCs in the presence of this type of compound. As the benzoate hydroxylation assay is based on

the Fenton reaction, no chelation information was obtained.[25] That is the subject of Chapter 2.

Additionally, the chelation of the PEG and PEG-HCCs after being mixed with $FeSO_4$ was studied by ICP-OES using the same proportions that were employed for the former EPR experiments. Figure1.4A shows that only 14.8 ± 1.9% of the iron was contained by the PEG-HCCs. This iron retention is due mostly to the PEG chains of the nanoparticle since experiments of the PEG-treated system showed that they were able to retain 11.0 ± 0.3% of the iron after 48 h dialysis. These results indicate that the iron chelation is not the main factor that causes the signal loss during EPR experiments. Hence, there is no significant pre-antioxidant property in the PEG-HCCs due to iron-chelation.

As was mentioned earlier, the drop in the EPR signal of the PEG-HCC-treated system might be caused by the interaction between H_2O_2 and PEG-HCCs because the interaction might prevent the $^{\bullet}OH$ formation. This possible interaction was investigated following the production of the radical cation $ABTS^{\bullet+}$ from the H_2O_2 oxidation of ABTS in the catalyzed by HRP enzyme by UV/Vis. The increase absorbance at 414 nm was used to monitor the reaction.[31] PEG-HCCs were incubated with H_2O_2 using the same ratio that was used for the EPR experiments. Figure 1.4B illustrates that only 5% of the H_2O_2 interacts with the PEG-HCCs. Again, the drop in the signal could be caused by the reaction between the radical cation $ABTS^{\bullet+}$ and PEG-HCCs. Figure 1.4B showed that there was no reaction between the PEG-HCCs and the product cation. Since only 5% of the H_2O_2 interacts with the PEG-HCCs, it is concluded that the loss of intensity in the

EPR signal was due principally to the reaction between the PEG-HCCs and the •OH generated. Thus, the rate constant of this reaction must be higher than the rate constant of the DEPMPO-OH formation, which is 7.8×10^9 M^{-1} s^{-1}.[48]

A

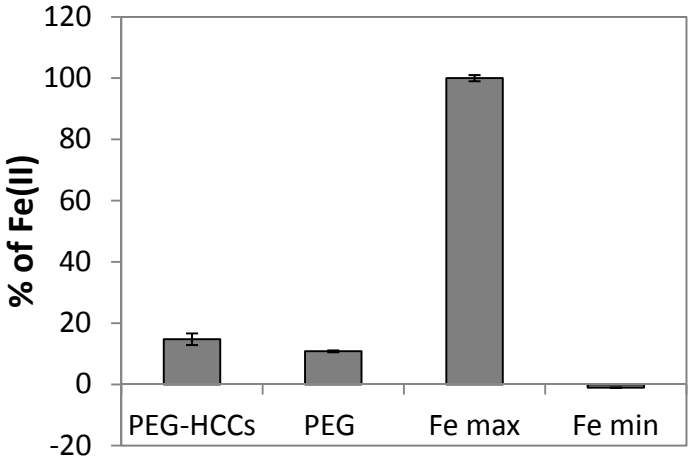

B

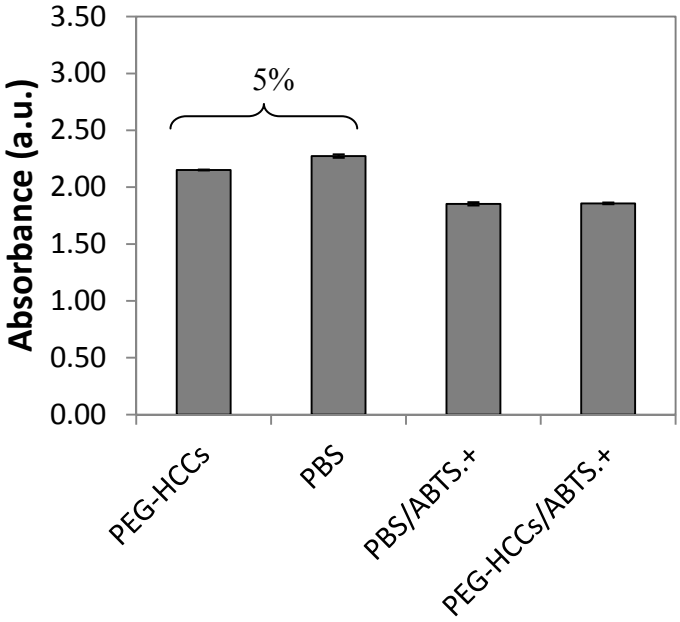

Figure 1.4. Interaction between the PEG-HCCs and Fenton reaction reagents. (A) % of Fe retained by the PEG-HCCs detected by ICP-OES. Either PEG-HCCs or PEG were mixed with $FeSO_4$ for 3 h and then dialyzed in a constant water flow for 48 h. "Fe max" is the maximum iron amount used in the experiment (no dialysis). "Fe min" corresponds to the amount of iron remaining inside the membrane after being dialyzed for 48 h. (B) ABTS oxidation catalyzed by HRP followed by UV/Vis analysis. The absorbance of the oxidation product, $ABTS^{\bullet+}$, was measured at 414 nm. Only ~5 % of the H_2O_2 interacts with the PEG-HCCs. No interaction between the PEG-HCCs and the cation product was observed since PBS/$ABTS^{\bullet+}$ and PEG-HCCs/$ABTS^{\bullet+}$ systems behave equally when PBS or PEG-HCCs were added after the cation was formed. Experiments were run in triplicate.

The ability of the PEG-HCCs to quench ROS extracellularly was also evaluated by exposing the PEG-HCCs to $O_2^{\bullet-}$ generated by the metabolism of HX/XO. The concentration of the superoxide anion was determined using a microplate assay[35] based on the SOD-inhibitable reduction of ferricytochrome *c*,[49] and followed as absorbance at 550 nm. It has been suggested that the carbon cores of the PEG-HCCs are responsible for their peroxyl radical scavenger properties,[25] and so their ability to inhibit the reduction of cytochrome *c* was calculated on this basis. PEG-HCCs were effective antioxidants and they achieved inhibition equivalent to half of the positive control (IC_{50}), which was a large excess of SOD. The IC_{50} value of the PEG-HCCs was 0.20 ± 0.01 mg/mL (Figure 1.5). The IC_{50} concentration for the PEG-HCCs is well within the concentration range shown to be acutely non-toxic.[24,26]

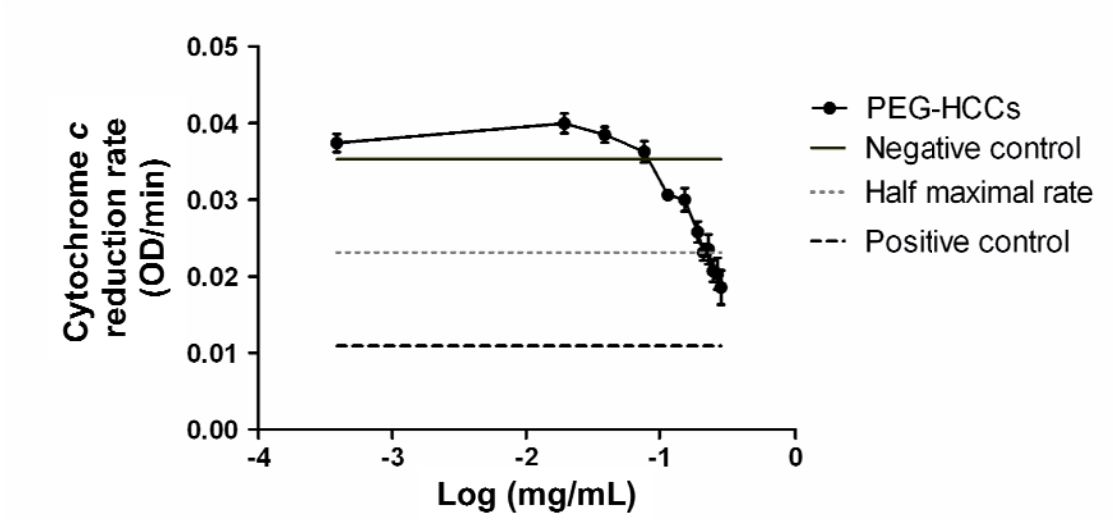

Figure 1.5. The antioxidant ability of the nanomaterials based on the SOD-inhibitable reduction of ferricytochrome *c*.

$NO^{\bullet}$ is a gas with milimolar water solubility and can act as an oxidant or reducing agent depending on the environment.[50] This diatomic molecule is more stable than other radicals (4-15 s lifetime in tissue),[51] and it is synthesized in small amounts *in vivo*.[50,55] $NO^{\bullet}$ is a potent vasodilator that also has an important role in neurotransmission and thrombosis.[50,51,55] Because of its biological impact and the low concentration found *in vivo*, it is important to prevent the alteration of the $NO^{\bullet}$ levels in biological systems avoiding the aggravation of several pathologies including ischemic/reperfusion events. A hemoglobin assay was used to determine whether PEG-HCCs scavenge this radical.

The oxidation of the HbO_2 by $NO^{\bullet}$ radical is a fast (~10^8 $M^{-1}s^{-1}$),[50] quantitative,[32] and irreversible[29] reaction in which metHb and nitrate ion are produced.[29,52] This reaction

can be spectrophotometrically monitored because the change in the oxidation state of iron from +2 to +3 causes a blue shift[23] of the Soret absorption peak of the hemeprotein from 415 nm (HbO_2)[52] to 401 nm (metHb).[32,52,53] In general, $NO^{\bullet}$ can be indirectly determined in aerobic aqueous systems by the production of metHb, which is estimated by the absorbance differences ($\Delta A_{401\text{-}411nm}$).[32,53] HbO_2 and the PEG-HCCs were mixed in a quartz cuvette before initiating the reaction by addition of $NO^{\bullet}$. If the PEG-HCCs and HbO_2 react with the radical at comparable rate, the absorbance difference will be lower than in the absence of PEG-HCCs, as the PEG-HCCs would be preventing the formation of metHb; the α (~570 nm) and β (~536 nm) peaks would show intensities similar to the control-HbO_2 spectrum instead of the metHb spectrum. Figure 1.6 indicated that neither the absorbance of the HbO_2 nor metHb was affected by the presence of the PEG-HCCs at low concentrations (0.02 mg/mL). However, when concentrations of 0.08 mg/mL are used, the heme group was destroyed. PEG-HCC concentrations of 0.04 mg/mL are also suitable for this assay (data not shown). Importantly*, in vivo*, HbO_2 is encapsulated in red blood cells,[54] so there is no evidence that suggests that the PEG-HCCs destroy HbO_2 *in vivo*. Figure 1.7 shows the difference spectrum of metHb and HbO_2 in the absence (blue) and presence of the PEG-HCCs (0.02 mg/mL, red). As the difference between the $\Delta A_{401\text{-}411nm}$ values of the control and the $\Delta A_{401\text{-}411nm}$ values of the PEG-HCCs differs in less than 10% (experimental error), it can be concluded that either the PEG-HCCs are not quenching the $NO^{\bullet}$ radicals or that the reaction rate between the $NO^{\bullet}$ and the PEG-HCCs is much slower than the $NO^{\bullet}$ and HbO_2 reaction.

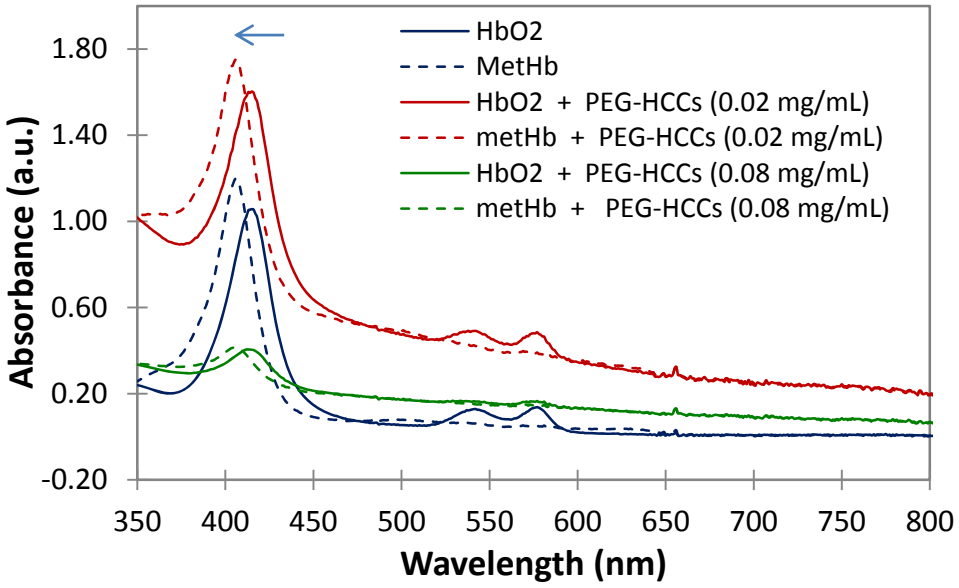

Figure 1.6. Optical spectra of the starting material (HbO_2) and final product (metHb) after being mixed with H_2O (blue set) or several concentrations of PEG-HCCs (red and green sets). Experiments were carried out in triplicate. The arrow indicates the blue shift of the Soret peak. α (~550 nm) and β (~590 nm) peaks of the HbO_2 decrease in intensity during conversion to metHb. Low concentration of the PEG-HCCs (0.02 mg/mL) does not decompose the HbO_2 (red set), however, higher concentrations of the PEG-HCCs (0.08 mg/mL) destroy the heme group (green set).

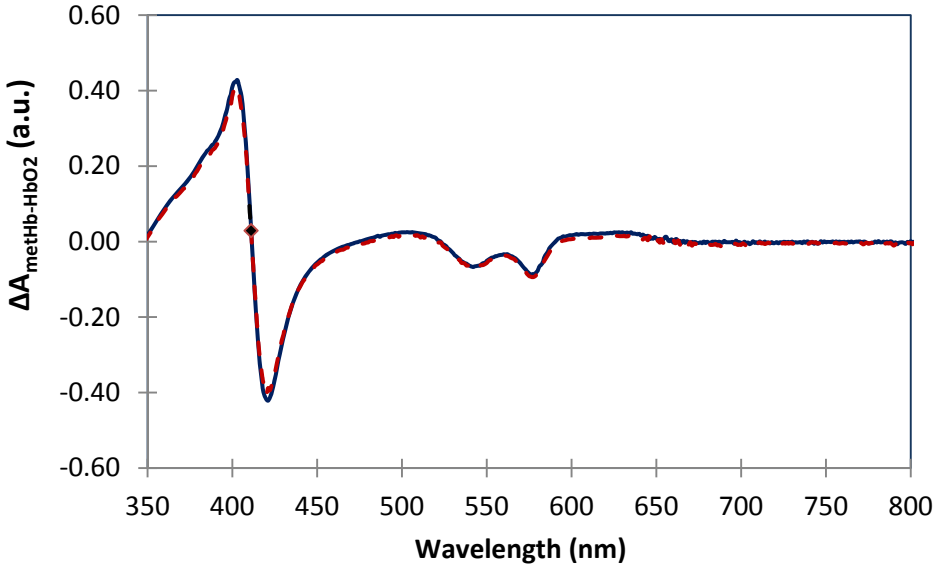

Figure 1.7. Difference spectrum of metHb and HbO_2 in the absence (blue) and presence of the PEG-HCCs (0.02 mg/mL, red). The difference between the $\Delta A_{401\text{-}411nm}$ values of the control and the $\Delta A_{401\text{-}411nm}$ values of PEG-HCCs treated system is lower than the experimental error. The experiment was done in triplicate. Control or PBS treated (blue, —). PEG-HCCs treated (red, ----).

In order to compare the rates of reaction between both PEG-HCCs and HbO_2 with $NO^{\bullet}$, the $NO^{\bullet}$ radicals were incubated with the PEG-HCCs at three different time points before the addition of the HbO_2.[34] Either buffer (control) or PEG-HCCs were incubated with $NO^{\bullet}$ in a 1:1 ratio for 20 ms, 1 s, or 1 min in the aging loop of the sequential stopped-flow. This solution was then mixed with HbO_2 in a 1:1 ratio in the detector chamber. Note that 0.04 mg/mL was the concentration of the PEG-HCCs when it was incubated with $NO^{\bullet}$, and 0.02 mg/mL when it was mixed with HbO_2. Figure 1.8 as well

as Figure A9 and Figure A10 (Appendix A) demonstrate that there is no interaction between the PEG-HCCs and $NO^{\bullet}$ radicals even after 1 min of incubation. Further, they show that $NO^{\bullet}$ radicals do not decay or decompose in these conditions. Since there was no effect with the PEG-HCCs, no experiments with PEG alone were performed as it is deemed unnecessary.

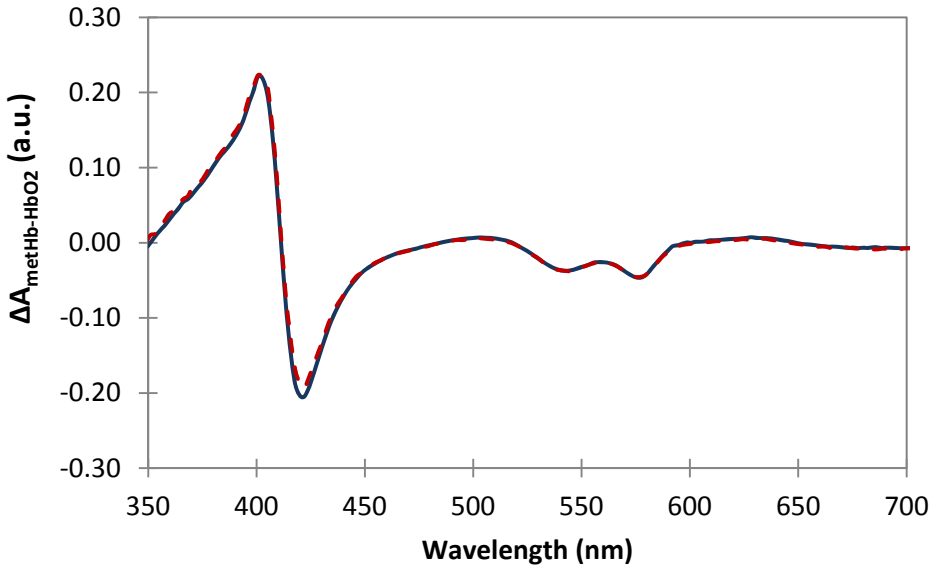

Figure 1.8. Difference spectrum of metHb and HbO_2 in the absence (blue) and presence of the PEG-HCCs (red) after being incubated with $NO^{\bullet}$ for 1 m. The difference between the $\Delta A_{401\text{-}411nm}$ values of the control and the $\Delta A_{401\text{-}411nm}$ values of PEG-HCCs treated system is lower than the experimental error. The experiment was carried out in triplicate. PBS treated (blue, —) and PEG-HCCs treated (red, ----).

$NO^{\bullet}$ reacts quickly with $O_2^{\bullet-}$ forming $ONOO^-$. Thus, the interaction between the $ONOO^-$ and the PEG-HCCs was also studied using the $ONOO^-$-induced quenching of the dye pyrogallol red. It was hypothesized that the PEG-HCCs would inhibit the quenching of the dye if they react with $ONOO^-$. Ascorbic acid, caffeic acid and trolox all inhibit the quenching reaction in a manner consistent with reported results,[38] but PEG-HCCs had no effect (Figure 1.9). Bearing in mind that $NO^{\bullet}$ is constantly produced *in vivo* and is freely diffusible, production of $ONOO^-$ is more likely to occur in regions in which there is a high local concentration of $O_2^{\bullet-}$. As was previously demonstrated, PEG-HCCs do scavenge $O_2^{\bullet-}$ and this upstream scavenging will necessarily decrease the amount of $ONOO^-$ produced *in vivo*.

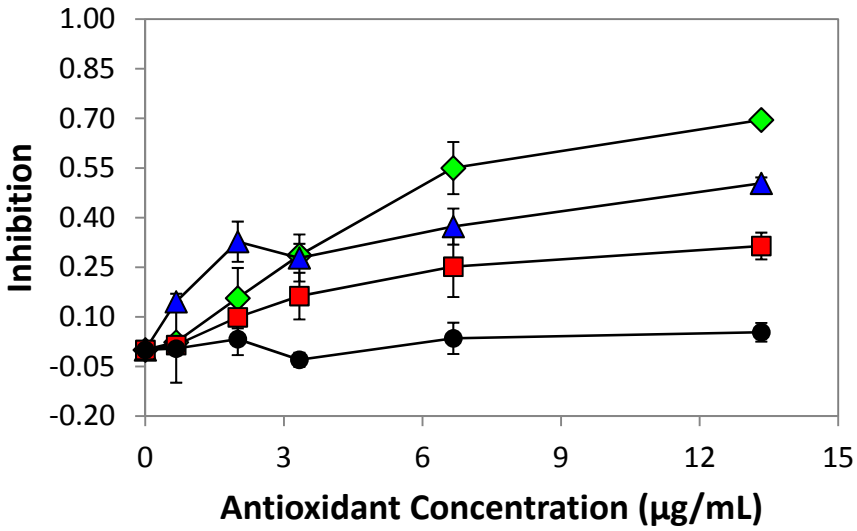

Figure 1. 9.- Inhibition of the pyrogallol red decomposition assay. (▲, blue) Caffeic acid. (♦, green) Ascorbic acid. (■, red) Trolox. (●, black) PEG-HCCs.

1.4. Conclusions

In summary, it has been demonstrated that PEG-HCCs quench ROS. 73% of $^{\bullet}OH$ species were scavenged by the PEG-HCCs with a *k* comparable with the DEPMPO-OH formation *k* (7.8×10^9 M^{-1} s^{-1}).[48] In this case, while iron chelating capability and the interaction of H_2O_2 with the PEG-HCCs might be small contributing factors to the quenching, they are not the main features responsible for the antioxidant properties observed. Remarkably, 98% of $O_2^{\bullet-}$ species were quenched by the PEG-HCCs with a *k* higher than 0.53 $M^{-1}s^{-1}$, which is the *k* corresponding to the DEPMPO-OOH formation.[47] Amazingly, based on the EPR measurements, 1 mg of the PEG-HCCs has the similar effect of 143 U/mg of SOD, which is 28 times the average value of the SOD activity reported for post-mortem human spinal cord.[35] In addition, PEG-HCCs were inert to $NO^{\bullet}$. These scavenging properties make the PEG-HCCs a highly suitable antioxidant treatment during ischemic/reperfusion events in which the production of $O_2^{\bullet-}$ dramatically increases and the levels of $NO^{\bullet}$ might decrease.[56] Therefore, a $NO^{\bullet}$-inert scavenger will help to stabilize the $NO^{\bullet}$ levels, thereby, improving the vascular homeostasis and contributing to the healing process. Finally, PEG-HCCs were also inert to $ONOO^-$. However, the production of $ONOO^-$ is more likely to occur in regions in which there is a high local concentration of $O_2^{\bullet-}$. Thus, a decrease in the levels of $O_2^{\bullet-}$ as we show here will also decrease the levels of $ONOO^-$.

1.5. Acknowledgements

Funding came from the Alliance for NanoHealth through a subcontract from the University of Texas Health Science Center, Houston (Department of Defense, W8XWH-09-2-0139); the Traumatic Brain Injury Consortium, funded by the United States Army (W81XWH-08-2-0141 and W81XWH-08-2-0143); and the Nanoscale Science and Engineering Initiative of the National Science Foundation under NSF Award EEC-0647452 for funding through the NSF Center for Biological and Environmental Nanotechnology.

1.6. References

1. Kulkarni, R. R.; Virkar, A. D.; D'mello, P. Antioxidant and antiinflammatory activity of *vitex negundo. Indian J Pharm Sci.,* **2008**, *70*, 838–840.
2. Bandyopadhyay, U.; Das, D.; Banerjee, R. K. Reactive oxygen species: oxidative damage and pathogenesis. *Curr Sci.,* **1999**, *77*, 658-666.
3. Zivkovic, J.; Zekovic, Z.; Mujie, I.; Godevac, D.; Mojovic, M.; Mujie, A.; Spasojevic, I. EPR Spin-trapping and spin-probing spectroscopy in assessing antioxidant properties: example on extracts of catkin, leaves, and spiny burs of *Castanea sativa*. *Food Biophysics*, **2009**, 4, 126-133.
4. Spasojevic, I.; Mojovic, M.; Blagojevic, D.; Spasic, S. D.; Jones, D. R.; Nikolic-Kokic, A.; Spasic, M. B. Relevance of the capacity of phosphorylated fructose to scavenge the hydroxyl radical. *Carbohydr. Res.*, **2009**, *344*, 80-84.
5. Dickinson, B. C.; Chang, C. J. Chemistry and biology of reactive oxygen species in signaling or stress responses. *Nat. Chem. Biol.,* **2011**, *7*, 504-511.

6. Jia, Z.; Zhu, H.; Misra, B. R.; Mahaney, J. E.; Li, Y.; Misra, H. P. EPR studies on the superoxide-scavenging capacity of the nutraceutical resveratrol. *Mol. Cell Biochem.,* **2008**, *313*, 187-194.

7. Cooke, M. S.; Evans, M. D.; Dizdaroglu, M.; Lunec, J. Oxidative DNA damage: mechanisms, mutation, and disease. *The FASEB Journal*, **2003**, *17*, 1195-1214

8. Sedelnikova, O. A.; Redon, C. E.; Dickey, J. S.; Nakamura, A. J.; Georgakilas, A. G.; Bonner, W. M. Role of oxidatively induced DNA lesions in human pathogenesis. *Mutat. Res.,* **2010**, *704*, 152–159.

9. Valko, M.; Leibfritz, D.; Moncol, J.; Cronin, M. T. D.; Mazur, M.; Telser, J. Free radicals and antioxidants in normal physiological functions and human disease. *Int. J. Biochem. Cell Biol.,* **2007**, *39*, 44-84.

10. Higashi, Y.; Noma, K.; Yoshizumi, M.; Kihara, Y. Endothelial function and oxidative stress in cardiovascular diseases. *Circ. J.,* **2009**, *73*, 411-418

11. Rocha, M.; Apostolova, N.; Hernandez-Mijares, A.; Herance, R.; Victor, V. M. Oxidative stress and endothelial dysfunction in cardiovascular disease: mitochondria-targeted therapeutics. *Curr. Med. Chem.,* **2010**, *17*, 3827-3841

12. Poulsen, H. E.; Loft, S. Cancer risk and oxidative DNA damage in man. *J. Mol. Med.,* **1996**, *74*, 297-312

13. Waris, G.; Ahsan, H. Reactive oxygen species: Role in the development of cancer and various chronic conditions. *J. Carcinog.,* **2006**, *5*, 14.

14. Phillips, D. C.; Dias, H. K.; Kitas, G. D.; Griffiths, H. R. Aberrant reactive oxygen and nitrogen species generation in rheumatoid arthritis (RA): causes and

consequences for immune function, cell survival, and therapeutic intervention. *Antioxid. Redox Signal,* **2010**, *12*, 743-785.

15. Mirshafiey, A.; Mohsenzadegan, M. The role of reactive oxygen species in immunopathogenesis of rheumatoid arthritis. *Iran J. Allergy Asthma Immunol.*, **2008**, *7*, 195-202.
16. Wiseman, H.; Halliwell, B. Damage to DNA by reactive oxygen and nitrogen species: role in inflammatory disease and progression to cancer. *Biochem J.*, **1996**, *313*, 17-29.
17. Rains, J. L.; Jain, S. K. Oxidative stress, insulin signaling, and diabetes. *Free Radic. Biol. Med.,* **2011**, *50*, 567-575.
18. Kondratova, A. A.; Kondratov, R. V. The circadian clock and pathology of the ageing brain. *Nat. Rev. Neurosci.,* **2012**, *13*, 325-335.
19. Uttara, B.; Singh, A. V.; Zamboni, P.; Mahajan, R. T. Oxidative stress and neurodegenerative diseases: a review of upstream and downstream antioxidant therapeutic options. *Curr. Neuropharmacol.,* **2009**, *7*, 65-74.
20. Pimentel, C.; Batista-Nascimento, L.; Rodrigues-Pousada, C.; Menezes, R. A. Oxidative stress in Alzheimer's and Parkinson's diseases: insights from the yeast *Saccharomyces cerevisiae*. *Oxid. Med. Cell Longev.,* **2012**, 132146.
21. Barnham, K. J.; Masters, C. L.; Bush, A. I. Neurodegenerative diseases and oxidative stress. *Nat. Rev. Drug Discov.,* **2004**, *3*, 205-214.
22. Chevion, M.; Jiang, Y.; Har-El, R.; Berenshtein, E.; Uretzky, G.; Kitrossky, N. Copper and iron are mobilized following myocardial ischemia: possible predictive criteria for tissue injury. *Proc. Nat. Acad. Sci.*, **1993**, *90*, 1102-1106.

23. Berka, V.; Palmer, G.; Cheng, P.; Tsai, A. Effects of various imidazole ligands on heme conformation in endothelial nitric oxide synthase. *Biochemistry*, **1998**, *37*, 6136-6144.

24. Berlin, J. M.; Pham, T. T.; Sano, D., Milas, Z.; Marcano, D.; Leonard, A. D.; Kosynkin, D. V.; Price, B. K.; Lucente-Shultz, R.; Myers, J. N.; Tour, J. M. Effective drug delivery, in vitro and in vivo, by carbon-based nanovectors non-covalently loaded with paclitaxel. *ACS Nano*, **2010**, *4*, 4621-4636.

25. Marcano, D. C.; Bitner, B. R.; Berlin, J. M.; Jarjour, J.; Lee, J. M.; Jacob, A.; Fabian, R. H.; Kent, T. A.; Tour, J. M. Design of poly(ethylene glycol)-functionalized hydrophilic carbon clusters for targeted therapy of cerebrovascular dysfunction in mild traumatic brain injury. *J. Neurotrauma*, **2012**, accepted.

26. Bitner, B. R.; Marcano, D. C.; Berlin, J. M.; Fabian, R. H.; Cherian, L.; Culver, J. C.; Dickinson, M. E.; Robertson, C. S.; Pautler, R. G.; Kent, T. A.; Tour, J. M. Antioxidant carbon particles improve cerebrovascular dysfunction following traumatic brain injury. *ACS Nano*, **2012**, accepted.

27. Samuni, A.; Carmichael, A. J.; Russo, A.; Mitchell, J. B.; Riesz. P. On the spin trapping and ESR detection of oxygen-derived radicals generated inside the cells. *Proc. Nat. Acad. Sci.*, **1986**, *83*, 7593-7597.

28. Galbusera, C.; Orth, P.; Fedida, D.; Spector, T. Superoxide radical production by allopurinol and xanthine oxidase. *Biochem. Pharmacol.,* **2006**, *71*, 1747-1752.

29. Lärfars, G.; Gyllenhammar, H. Measurement of methemoglobin formation from oxyhemoglobin. A real-time, continuous assay of nitric oxide release by human polymorphonuclear leukocytes. *J. Immunol. Methods,* **1995**, *184*, 53-62.

30. Bolojan, L.; Takacs, I. M.; Miclaus, V.; Damian, G. An EPR study of superoxide radicals from potassium superoxide solutions. *Appl. Magn. Reson*. **2012**, *42*, 333-341

31. Kadnikova, E. N.; Kostic, N. M. Oxidation of ABTS by hydrogen peroxide catalyzed by horseradish peroxidase encapsulated into sol-gel glass. Effects of glass matrix on reactivity. *J. Mol. Catal. B Enzym.,* **2002**, *18*, 39-48.

32. Feelisch, M.; Noack, E. A. Correlation between nitric oxide formation during degradation of organic nitrates and activation of guanylatecyclase. *Eur. J. Pharmacol*., **1987**, *139*, 19-30.

33. Sanders, S. P.; Harrison, S. J.; Kuppusamy, P.; Sylvester, J. T.; Zweier, J. L. A comparative study of EPR spin trapping and cytochrome c reduction techniques for the measurement of superoxide anions. *Free Radic. Biol. Med.,* **1994**, *16*, 753-761.

34. Tsai, A. L.; Berka, V.; Sharina, I.; Martin, E. Dynamic ligand exchange in soluble guanylylcyclase (sGC): implications for sGC regulation and desensitization. *J. Biol. Chem.,* **2011**, *286*, 43182-43192.

35. Quick, K. L.; Hardt, J. I.; Dugan, L. L. Rapid microplate assay for superoxide scavenging efficiency. *J. Neurosci. Methods,* **2000**, *97*, 139-144.

36. Balavoine, G. G.; Geletii, Y. V. Peroxynitrite scavenging by different antioxidants. Part I: Convenient assay. *Nitric Oxide*, **1999**, *3*, 40-54.

37. Papée, H. M.; Petriconi, G. L. Formation and decomposition of alkaline ‘pernitrite’. *Nature*, **1964**, *204*, 142 –144.

38. Robaszkiewicz, A.; Bartosz, G. Estimation of antioxidant capacity against pathophysiologically relevant oxidants using Pyrogallol Red. *Biochem. Biophys. Res. Commun.,* **2009**, *390*, 659-661.

39. Ivan, S.; Miloš, M.; Aleksandar, I.; Goranc, B. The role of EPR spectroscopy in studies of the oxidative status of biological systems and the antioxidative properties of various compounds. *J. Serb. Chem. Soc.,* **2011**, *76*, 647-677.

40. Livposky, A.; Tzitrinovich, Z.; Friedmann, H.; Applerot, G.; Gedanken, A.; Lubart, R. EPR Study of Visible Light-Induced ROS Generation by Nanoparticles at ZnO. J. *Phys. Chem C,* **2009**, *113*, 15997-16001.

41. Frejaville, C.; Karoui, H.; Tuccio, B.; LeMoigne, F.; Culcasi, M.; Pietri, S.; Laurocella, R.; Tordo, P. 5-Diethoxyphosphoryl-5-methyl-1-pyrroline *N*-Oxide (DEPMPO): a new phosphorylated nitrone for the efficient *in vitro* and *in vivo* spin trapping of oxygen-centred Radicals. *J. Chem. Soc. Chem. Commun.,* **1999**, 1793-1794.

42. Singh, R. J.; Karoui, H.; Gunther, M. R.; Beckman, J. S.; Mason, R. P.; Kalyanaraman, B. Reexamination of the mechanism of hydroxyl radical adducts formed from the reaction between familial amyotrophic lateral sclerosis-associated Cu, Zn superoxide dismutase mutants and H_2O_2. *Proc. Natl. Acad. Sci. USA*, **1998**, *95*, 6675-6680.

43. Miller, C. J.; Rose, A. L.; Waite, D. T. Phthalhydrazide chemiluminescence method for determination of hydroxyl radical production: modifications and adaptations for use in natural systems. *Anal. Chem.,* **2011**, *83*, 261-268.

44. Cohen, G.; Heikkila, R. E. The generation of hydrogen peroxide, superoxide radical, and hydroxyl radical by 6-hydroxydopamine, dialuric acid, and related cytotoxic agents. *J. Biol. Chem.,* **1974**, *249*, 2447-52.

45. Liochev, S. I.; Fridovich, I. The effects of superoxide dismutase on H_2O_2 formation. *Free Radic. Biol. Med.,* **2007**, *42*, 1465-1469.

46. Mruk, D. D.; Silvestrini, B.; Mo, M. Y.; Cheng, C. Y. Antioxidant superoxide dismutase - a review: its function, regulation in the testis, and role in male fertility. *Contraception,* **2002**, *65*, 305-311.

47. Keszler, A.; Kalyanaraman, B.; Hogg, N. Comparative investigation of superoxide trapping by cyclic nitrone spin traps: the use of singular value decomposition and multiple linear regression analysis. *Free Radic. Biol. Med.,* **2003**, *35*, 1149-1157.

48. Myhre, O.; Vestad, T. A.; Sagstuen, E.; Aarnes, H.; Fonnum, F. The effects of aliphatic (n-nonane), naphtenic (1,2,4 - trimethylcyclohexane), and aromatic (1,2,4 - trimethylbenzene) hydrocarbons on respiratory burst in human neutrophil granulocytes. *Toxicol. Appl. Pharmacol.,* **2000**, *167*, 222-230.

49. McCord, J. M.; Fridovich, I. Superoxide dismutase, an enzymic function for erythrocuprein (hemocuprein). *J. Biol. Chem.,* **1969**, *244*, 6049-6055.

50. Yasmin, S.; Andrews, S. C.; Moore, G. R.; Le Brun, N. E. A new role for heme, facilitating release of iron from the bacterioferritin iron biomineral. *J. Biol. Chem.,* **2011**, *286*, 3473-3483.

51. Archer, S. Measurement of nitric oxide in biological models. *FASEB J.* **1993**, *7*, 349-360.

52. Noak, E; Kubitzek, D.; Kojda, G. "Spectrophotometric Determination of Nitric Oxide Using Hemoglobin. *Neuroprotocols,* **1992**, *1*, 133-139.

53. Kelm, M.; Dahmann, R.; Wink, D.; Feelisch, M. The nitric oxide/superoxide assay. Insights into the biological chemistry of the NO/O_2^-. Interaction. *J. Biol. Chem.,* **1997**, *272*, 9922-9932.

54. Azarov, I.; Liu, C.; Reynolds, H.; Tsekouras, Z.; Lee, J. S.; Gladwin, M. T.; Kim-Shapiro, D. B. Mechanisms of slower nitric oxide uptake by red blood cells and other hemoglobin-containing vesicles. *J. Biol. Chem.,* **2011**, *286*, 33567-33579.

55. Gladwin, M. T.; Kim-Shapiro, D. B. The functional nitrite reductase activity of the heme-globins. *Blood*, **2008**, *112*, 2636-2647.

56. Perrelli, M.; Pagliaro, P.; Penna, C. Ischemia/reperfusion injury and cardioprotective mechanisms: Role of mitochondria and reactive oxygen species. *World J Cardiol.,* **2011**, *3*, 186-200.

1.7. Experimental Contributions

I performed and analyzed the data related to EPR, chelation, oxidation of the ABTS, and oxo-hemoglobin experiments. Dr. Berka assisted with the EPR and hemoglobin experiments. Errol L. Samuel and Austin Potter worked on the inhibition of the pyrogallol red decomposition assay and characterization of the PEG-HCCs. Dr. Bitner performed the cytochrome *c* experiments.

Chapter 2

Design of Poly(ethylene glycol)-functionalized Hydrophilic Carbon Clusters for Targeted Therapy of Cerebrovascular Dysfunction in Mild Traumatic Brain Injury

This chapter was entirely copied from the reference #1 of this section

2.1. Introduction

Reactive oxygen species (ROS) are an essential component of many regulatory processes in living organisms. Normally, they are continuously generated, transformed and consumed inside biological systems in which timing and location of these reactive species are firmly regulated[2]. Oxidative stress and vascular dysfunction is a prominent feature of traumatic brain injury (TBI),[3-5] in particular when accompanied by secondary

insults such as hemorrhagic hypotension.[6,7] Cerebrovascular dysfunction is evident even in mild TBI (mTBI) and if complicated by hypotension, causes both structural lesions and behavioral dysfunction.[8] In the case of an acute injury, there is both an acute elaboration of superoxide radicals[7] and an extended period of oxidative stress as the initial injury sets off a cascade that can last for days.[9] Consequently, antioxidant therapies have been investigated for treating TBI. Extensive research has explored using small molecule antioxidants, such as phenyl *N*-*tert*-butyl nitrone (PBN) and tirilazad mesylate, or stabilized enzymes, such as PEGylated superoxide dismutase (PEG-SOD), to combat oxidative stress.[10,11] Unfortunately, none of these potential therapies has shown efficacy in clinical trials,[11,13] and there are no Food and Drug Administration-approved antioxidant therapies for these conditions.[14]

The generation of oxidative radicals is increased after a TBI. Secondary injuries such as hypotension (low blood pressure), a major contributor to poor outcome in TBI, are additional sources of oxidative radical generation with several bursts of superoxide documented throughout the course of TBI and hypotension and reperfusion.[7] Moreover, our previous work has shown that PEG-SOD has only small and transient effects.[7] Therapies to address oxidative stress must, therefore, be rapidly effective and able to address the site of radical generation or its consequences at a clinically realistic time point. There is little evidence that conventional antioxidants can achieve these goals. Hence, there is a need to find new classes of biologically compatible antioxidants. Nanoparticles are an emerging group of such materials.[15] Nanoparticles have markedly different biodistribution and metabolic profiles than small molecules or enzymes, and they also may afford improved *in vivo* efficacy.

We previously showed that single-walled carbon nanotubes (SWCNTs) and ultrashort SWCNTs are antioxidants, as measured by the oxygen radical absorbance capacity (ORAC) assay.[15] We have recently developed another class of biologically compatible carbon-based nanovectors, poly(ethylene glycol)-functionalized hydrophilic carbon clusters (PEG-HCCs).[16,17] PEG-HCCs can be readily functionalized with antibodies for targeted drug delivery. These PEG-HCCs can be loaded with hydrophobic drugs, and when mixed with an antibody, a noncovalent formulation capable of targeted drug delivery in vitro is formed.[18,19] PEG-HCCs are approximately 50 nm in size at neutral pH based on dynamic light scattering (DLS) and have a zeta potential of -23.04 mV at pH 7.0, which is evidence for the negatively charge surface of the nanoparticle. This potential also indicates that the PEG-HCCs will flocculate with time. However, the PEG-HCCs can be easily re-suspended after vortexing the mixture for 5 min. Also importantly, ~ 94% of the PEG-HCC is constituted by PEG,[18] which is a non-ionic hydrophilic polymer approved for certain uses by the Food and Drug Administration (FDA) that is well tolerated clinically[20-23] with the additional benefit that polyethylene glycol can protect and restore the integrity of cell membranes.[24-26] Our preliminary toxicity and biodistribution studies indicate that these PEG-HCCs nanoparticles are not acutely toxic in normal mice, with no evidence of chemical or pathological damage to major organs and with a circulating half life of 2-3 hours.[18]

Here we report the *in-vitro* characteristics of PEG-HCC's designed specifically to address cerebrovascular dysfunction that accompanies TBI. We show that PEG-HCCs possess antioxidant activity that is potent enough to reduce oxidative stress *in vitro* following injury that its antioxidant mechanism does not involve metal chelation, and can

be targeted to a model of injured brain endothelial cells expressing p-selectin antigen. P-selectin expression is increased in brain endothelial cells following traumatic brain injury,[27] and possibly systemically depending on the trauma mechanism. These results suggest that targeted PEG-HCCs are potential therapeutics for oxidative stress-induced cerebrovacular dysfunction from mTBI.

2.2. Experimental Procedures

For all these experiments, PEG-HCCs were prepared as previously described and sterile filtered using a 0.20 μm pore size membrane.[18]

2.2.1. ORAC Assay

The following solutions were prepared daily: phosphate buffer at pH 7.4 (PBS, 75 mM), fluorescein sodium salt (0.1 μM), α,α'-azodiisobutyramidine dihydrochloride (AAPH, 0.15 M), racemic 6-hydroxy-2,5,7,8-tettramethylchromate-2-carboxilic acid (trolox, 400 μM). The experiment was carried out in a 96-well plate and each sample was analyzed by triplicate as shown below (Table 3.1). After the addition of the fluorescent probe or PBS and sample (1st step) to the assigned wells, the plate was incubated at 37 ºC for 15 min in a TECAN plate reader. Then, the ice-cold AAPH or PBS was added (2nd step) and the fluorescent intensity at 530 nm (485 nm excitation) was measured every minute for 2 h. Data were analyzed as follow: control 2 (background) was subtracted from the assay and control 1. The assay well results were divided by the control 1 and the

area under the curve (AUC) was determined by equation 1. trolox mass equivalents (TME) were determined by equation 2. [18,28-34]

$$AUC = 1 + \frac{f1}{f0} + \frac{f2}{f0} + \frac{f3}{f0} + \ \ldots + \frac{fi}{f0} \qquad \text{(Equation 2.1)}$$

$$TME = \frac{AUC_{Sample} - AUC_{Blank}}{AUC_{Trolox} - AUC_{Blank}} \ x \ \frac{Trolox_{mass\,(mg)}}{Sample_{mass\,(mg)}} \qquad \text{(Equation 2.2)}$$

Table 2.1. ORAC Assay design

	1st step		**2nd step**
Assay	120 µL of Fluorescein	20 µL of Sample	60 µL of AAPH
Control 1 (no AAPH)	120 µL of Fluorescein	20 µL of Sample	60 µL of PBS
Control 2 (no Fluorescein)	120 µL of PBS	20 µL of Sample	60 µL of AAPH

Trolox and phosphate buffer (blank) were run as samples. At least 3 standards of trolox were run for the calibration curve.

2.2.2. Chelation Assays

It has been found that iron forms deposits in patients with mTBI, this iron accumulation can be involved in the pathology of a TBI as one of the major secondary

events.[35-37] Furthermore, free iron causes oxidative stress when reacts with hydrogen peroxide to form hydroxyl radicals (Fenton reaction), and with lipids to produce alkoxy and peroxyl radicals (lipid peroxidation). Iron chelation therapy has been proposed in order to diminish the oxidative process.[36] Nonetheless, it is important to understand the effect that the chelator might have on the catalytic cycle of Fe^{+2}/Fe^{+3} process. In order to explore the behavior of the iron when combined with our nanoparticles, we ran the following iron chelator assays: benzoate hydroxylation and ascorbate oxidation. Ascorbic acid (cat # AC40147), benzoic acid (cat # AC22180), iron(II) sulfate heptahydrate (cat # AC42373), iron(III) chloride hexahydrate (cat # AC21709), and the disodium ethylenediamine tetraacetate (EDTA, cat # E4884) were obtained from Fisher Scientific. Deferoxamine mesylate salt (DFO, cat# D9533) was obtained from Sigma-Aldrich.

2.2.2.1. Benzoate Hydroxylation

This assay is based on the hydroxylation of benzoate when exposed to iron and H_2O_2, producing the fluorescent compounds 2,3,4-trihydroxybenzoate (308 nm excitation and 410 nm emission)[38-41] with the major products 2-hydroxybenzoic acid salt or salicylic acid salt at pH 7.4. In brief, the following solutions were freshly prepared before each run according to reported procedures:[42] benzoic acid (3 mM, recrystallized from hot water), $FeCl_3$ (1.80 mM), $FeSO_4$ (1.80 mM), methoxypolyethylene glycol amine polymer (PEG MW 5,000, 0.02 mg/mL) and PEG-HCCs (0.02 mg/mL). EDTA (0.60 mM) and DFO (0.60 mM) were used as the positive and negative control, respectively. The benzoic acid was incubated at room temperature for 1 h in the phosphate buffer (pH 7.4) with 5 mM of

H_2O_2 and the ferric or ferrous iron salt, in the presence of one of the controls or the PEG-HCCs. The reaction was started by the addition of any the iron salts and kept in dark. Salicylate was used to determine the quenching effect of the materials.[42]

2.2.2.2. Ascorbate Oxidation

This assay was performed in a similar way to that described previously.[43-47] Briefly, the following solutions were prepared prior to each experiment: ascorbic acid (0.1 mM), $FeCl_3$ (0.60 mM), potassium phosphate buffer (50 mM, pH 7.4, cleaned with Chelex resin), EDTA (0.02 mg/mL previously recrystallized three times from hot water), DFO (0.02 mg/mL), and PEG-HCCs (0.02 mg/mL). The ascorbate absorbance at 265 nm was measured after 1, 5 and 30 min using a TECAN plate reader.

2.2.3. Cell Culture

Murine brain endothelioma (bEnd.3, CRL 2299, ATCC, Manassas, VA) were cultured in DMEM-F12 (50:50) with 4 mM L-glutamine media, supplemented with 10% fetal bovine serum (both from HyClone) and 1% Pen Strep (+10,000 u/mL penicillin/+10,000 µg/mL streptomycin, from GIBCO). During the second week, between the 4th and 6th passage, cell experiments were performed.

2.2.3.1. P-selectin Targeting

bEnd.3 cells were grown on glass covers to 60-70% confluence in 6 well plates. P-selectin-targeted PEG-HCCs (ps/PEG-HCCs) were synthesized by adding 0.01 µg anti-p-selectin antibody (Santa Cruz Biotechnology Inc., Santa Cruz, CA) to 0.49 µg PEG-HCCs and incubating at RT for 1 h. The antibody possesses hydrophilic and hydrophobic

domains that allow the nanovector to sequester it. The bEnd.3 cells were treated with histamine (20 μM) to induce p-selectin expression or woth 1X PBS (histamine diluent) as a control.[48] After a 15 min incubation at 37° C, the cells were treated with vehicle (1X PBS), PEG-HCCs (0.49 μg), or ps/PEG-HCCs. Cells were incubated for 15 min and then washed twice and fixed with methanol. Cells were washed and stained with anti-PEG (Epitomics, Burlingame, CA) and anti-p-selectin antibodies (Santa Cruz Biotechnology Inc, Santa Cruz, CA). After washing, cells were probed with fluorescent secondary antibodies to the anti-PEG and anti-p-selectin antibodies (Invitrogen, Carlsbad, CA). Glass covers were mounted on slides and fluorescent images were captured on an epifluorescent microscope.

2.2.3.2. Intracellular Superoxide Cell Culture Model

bEnd.3 cells were cultured to 50-80% confluence in 6 well plates in 2 mL of culture media. The cells were treated with vehicle (1X PBS), PEG-HCCs, ps/PEG-HCCs, or p-selectin antibody alone (same concentration as found in ps/PEG-HCCs). After 15 min, the cells were treated with 10 μL of 2 mM Antimycin A or 10 μL ethanol (control). Antimycin A has been shown to induce intracellular superoxide radical production.[49] The cells were incubated at 37 °C for 40 min, at which point 2 μL of 10 mM dihydroethidine (DHE)[49] (in 50%/50% DMSO/1X PBS) was added to wells or 50%/50% DMSO/1X PBS (control). DHE reacts with ROS to form 2-hydroxyethidium, which possesses red fluorescence when excited near 480 nm; thus, the increase in red fluorescence is proportional to the ROS in the sample.[50] The cells were then placed on ice, trypsinized, and washed twice. Cells were subsequently counted and stained with SytoxRed (viability

stain). 10,000 cells were analyzed per treatment group using the TXRED channel (DHE) and SytoxRed to assess cell viability. A higher dose of Antimycin A was also studied to confirm that PEG-HCC's were able to protect against oxidative cell death (Appendix B, Figure B1).

2.3. Results and Discussion

2.3.1. ORAC Assay

The antioxidant capacity of the PEG-HCCs was compared by ORAC to known antioxidants vitamin C, caffeic acid, and catechin. ORAC measures antioxidant capacity by the ability of a substance to inhibit the loss of fluorescence caused by the oxidation of a fluorescent dye by peroxyl radicals formed during the thermal decomposition of the AAPH,[28-34] without the assistance of any metal.[32] The linear relationship between the net area and antioxidant concentration was evaluated by using a set of trolox and PEG-HCCs standards (Appendix B, Figure B2 - Figure B4). Table B.1 (Appendix B) summarizes the correlation coefficient, slope, and intercept of the trolox standard curves obtained in each run. The assay was consistent for all concentrations tested. For comparison and TME calculations, the concentrations of vitamin C, caffeic acid, catechin, trolox, and PEG-HCCs were kept constant at 1.6 µg/mL (Figure 2.1A and Table B2 of Appendix B). According to these results, PEG-HCCs showed higher antioxidant capacity than vitamin C, but lower than catechin and caffeic acid (Figure 2.1B). This range of antioxidant potential demonstrates that the PEG-HCCs likely possess enough antioxidant capacity to

be biologically relevant. Although the antioxidant mechanism is not fully known, given the nature of the carbon core, we hypothesize that this is due to the conjugated domains in the carbon core. When these domains receive two RO· species, two carbon–carbon pi-bonds will be lost but two new C–O sigma bonds and one new C–C pi bond will be formed without any radical species remaining (Figure 2.2).

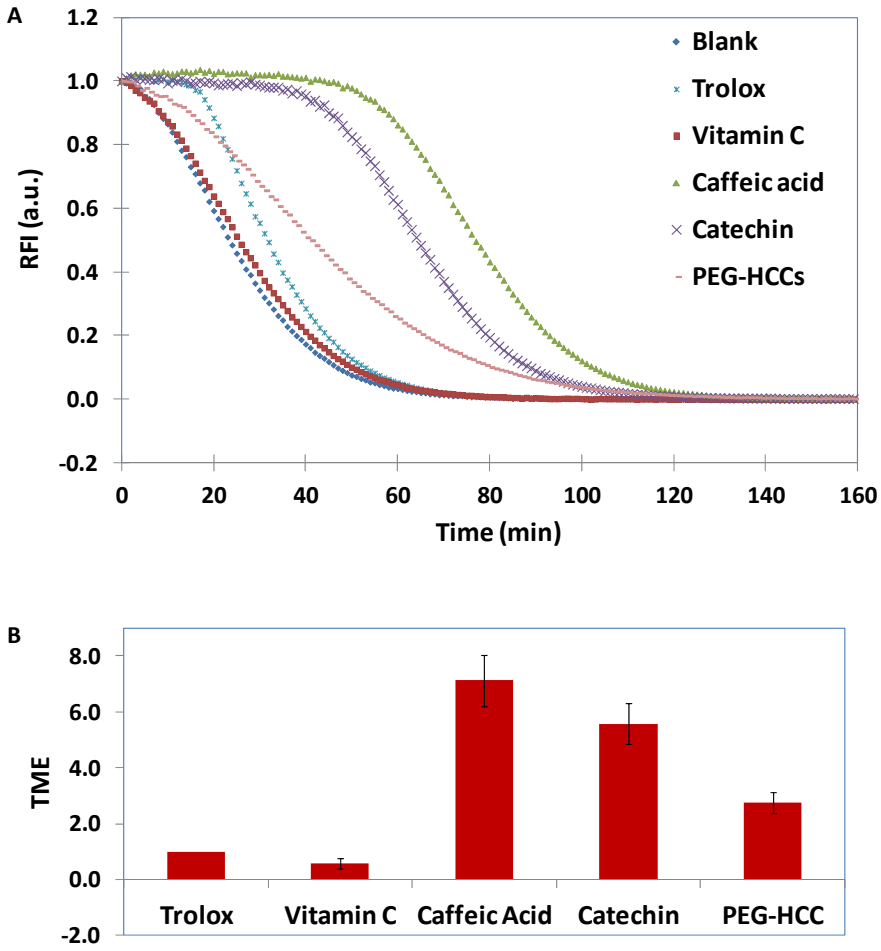

Figure 2.1. Typical fluorescence decay and calibration curves obtained. (A) Fluorescence decay curve obtained during the vitamin C, caffeic acid, catechin, and PEG-HCCs

evaluation. (B) Curve C represents the TME values corresponding to the different known antioxidants and carbon nanoparticles respectively. Trolox is the reference compound (TME_{trolox}=1).

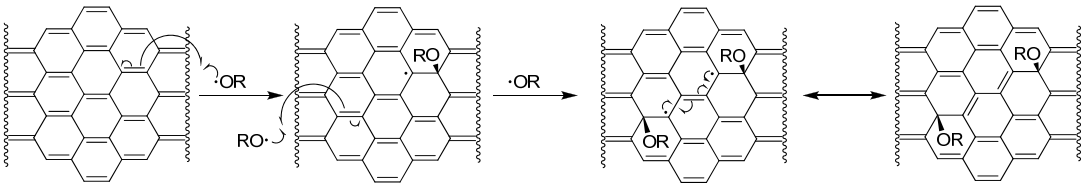

Figure 2.2. Suggested radical scavenging mechanism. Two additions of RO· result in the loss of two C–C pi-bonds and the formation of two new C–O sigma bonds and one new C–C pi bond without any radical species remaining.

2.3.2. Chelation as a Potential Mechanism

Iron accumulation in the pathology of TBI has been reported for mice[51] and humans[35] based on magnetic resonance imaging. It is known that Fe^{+2} and Fe^{+3} form lipid alkoxy radical and peroxyl radicals respectively, which induced the production of the neurotoxic aldehydes.[15] Therefore, it is important to determine if the nanoparticles stimulate the iron redox cycle (similar to EDTA) or inhibit it (similar to DFO). In order to assess this property, chelation assays were performed.

2.3.2.1. Benzoate Hydroxylation

The iron chelating assay was used to evaluate the antioxidant capacity of PEG-HCCs when is exposed to hydroxyl radicals produced by the reaction between iron and H_2O_2. In this assay, we monitored the oxidation of benzoate to salicylate by hydroxyl radicals produced by the Fenton reaction. To ensure that this measurement would be robust, sodium salicylate (SA) was mixed with PEG or PEG-HCCs every time that the experiment was run, in order to estimate how the fluorescence intensity was affected by the nanomaterial or the polymer, and then we proceeded to correct it (Figure 2.3A). In general, it was observed that PEG-HCCs quench about ~20% of the fluorescence and the PEG can enhance the fluorescence up to ~10%. In the actual assay, EDTA and DFO were included as positive and negative controls, respectively. PEG-HCCs decreased the hydroxylation process as well as DFO in comparison to the case in which no chelating agent was added (Figure 2.3B and 2.3C) for both iron systems. Interestingly, both PEG-HCCs and PEG reduced the hydroxylation of benzoic acid when the highest concentration of Fe^{+2} was used. We speculate that this could be due to the radical scavenger capacity of the carbon core (Figure 2.2), the degradation of the polymer chains as previously reported,[52-54] or both. Iron/PEG-HCCs systems do not induce the Fenton reaction.

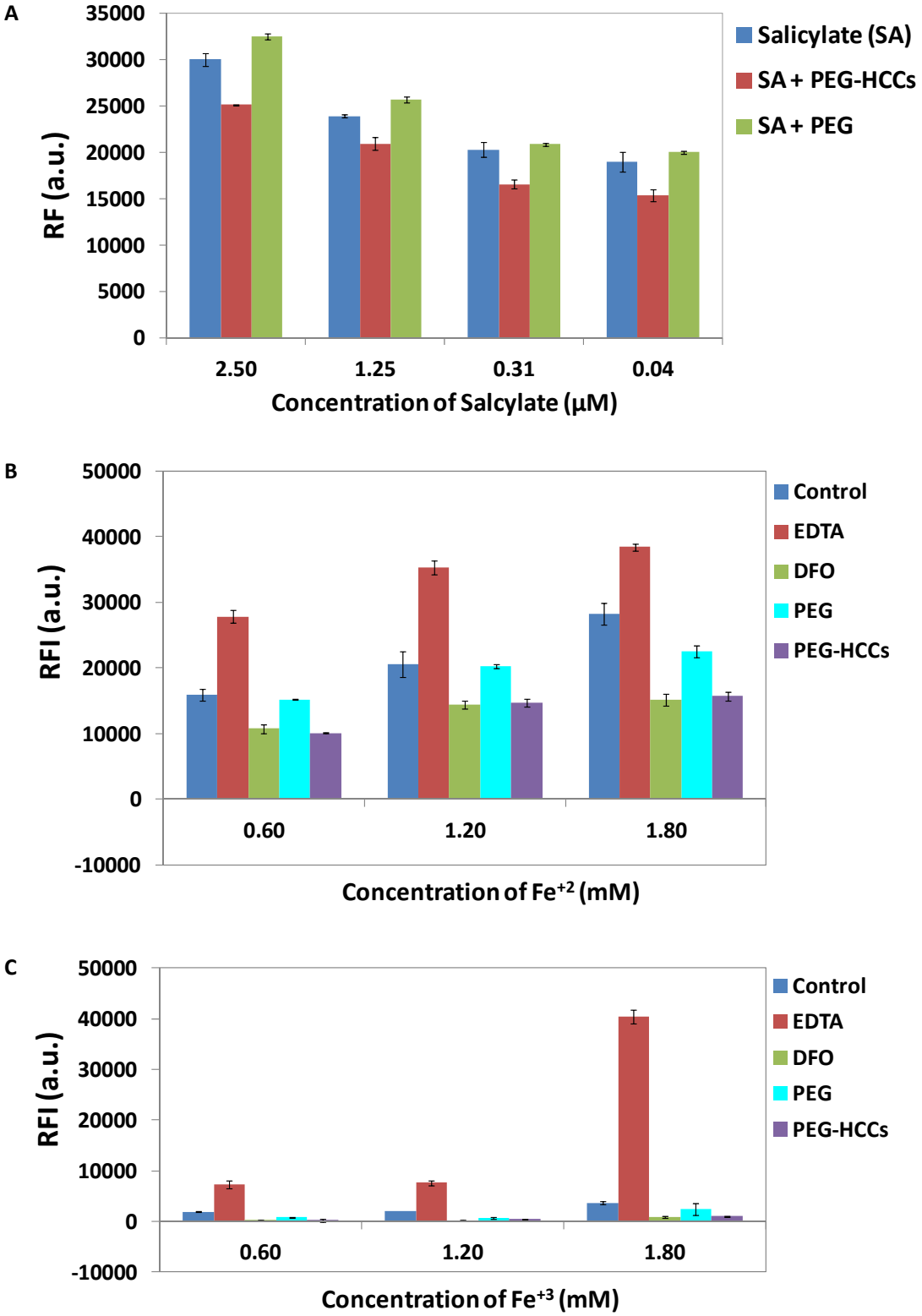
A
35000
30000
25000
20000
15000
10000
5000
0
RF (a.u.)
2.50
1.25
0.31
0.04
Concentration of Salcylate (µM)
Salicylate (SA)
SA + PEG-HCCs
SA + PEG
B
50000
40000
30000
20000
10000
0
-10000
RFI (a.u.)
0.60
1.20
1.80
Concentration of Fe+2 (mM)
Control
EDTA
DFO
PEG
PEG-HCCs
C
50000
40000
30000
20000
10000
0
-10000
RFI (a.u.)
0.60
1.20
1.80
Concentration of Fe+3 (mM)
Control
EDTA
DFO
PEG
PEG-HCCs

Figure 2.3. Benzoate hydroxylation assay. (A) Typical fluorescence quenching evaluation of the PEG-HCCs, PEG chains, and SA obtained in each experiment. PEG-HCCs can decrease the fluorescence intensity about ~20% while PEG can enhance it up to ~10% in average. These estimations were used for corrections purposes. (B) Benzoate hydroxylation induced by Fe^{+2} in the presence of EDTA, DFO, PEG-HCCs and PEG. PEG-HCCs and DFO inhibit the hydroxylation process at a similar level. In fact, PEG also prevents the hydroxylation at the highest concentration of the iron. (C) Benzoate hydroxylation induced by Fe^{+3}. Again, PEG-HCCs and DFO inhibit the hydroxylation process at a similar level. PEG-HCCs do not induce the Fenton reaction. The concentrations used were 0.60 mM for EDTA and DFO and 0.02 mg/mL for PEG-HCCs and 0.02 mg/mL for PEG.

2.3.2.2. Ascorbate Oxidation

Ascorbic acid is able to serve as a donor antioxidant in free radical-mediated oxidative processes. But it is also able to reduce redox-active metals such as copper and iron, thereby increasing the oxidant properties of those metals. In general, at low concentrations, ascorbic acid is prone to be a pro-oxidant and at high concentrations serves as an antioxidant.[45] In this assay, the oxidation of ascorbic acid by Fe^{3+} is monitored in the presence or absence of substances. EDTA again enhanced the oxidative activity of the Fe^{+3} while DFO inhibited it. We tested the PEG-HCCs in this system to determine if their antioxidant capacity could be due to interactions with trace iron content, and if there is such an interaction, the oxidation of the ascorbic acid should be

inhibited. We followed the oxidation of the ascorbic acid after 5 min and 30 min of metal addition (Figures 2.4A and 2.4B). And, we found that in this system the PEG-HCCs function as potent oxidants, regardless of the presence or absence of Fe^{3+}. PEG-HCCs and ascorbic acid show similar pro-oxidant and antioxidant behaviors; the difference is that for PEG-HCCs, no metal participation is necessary.

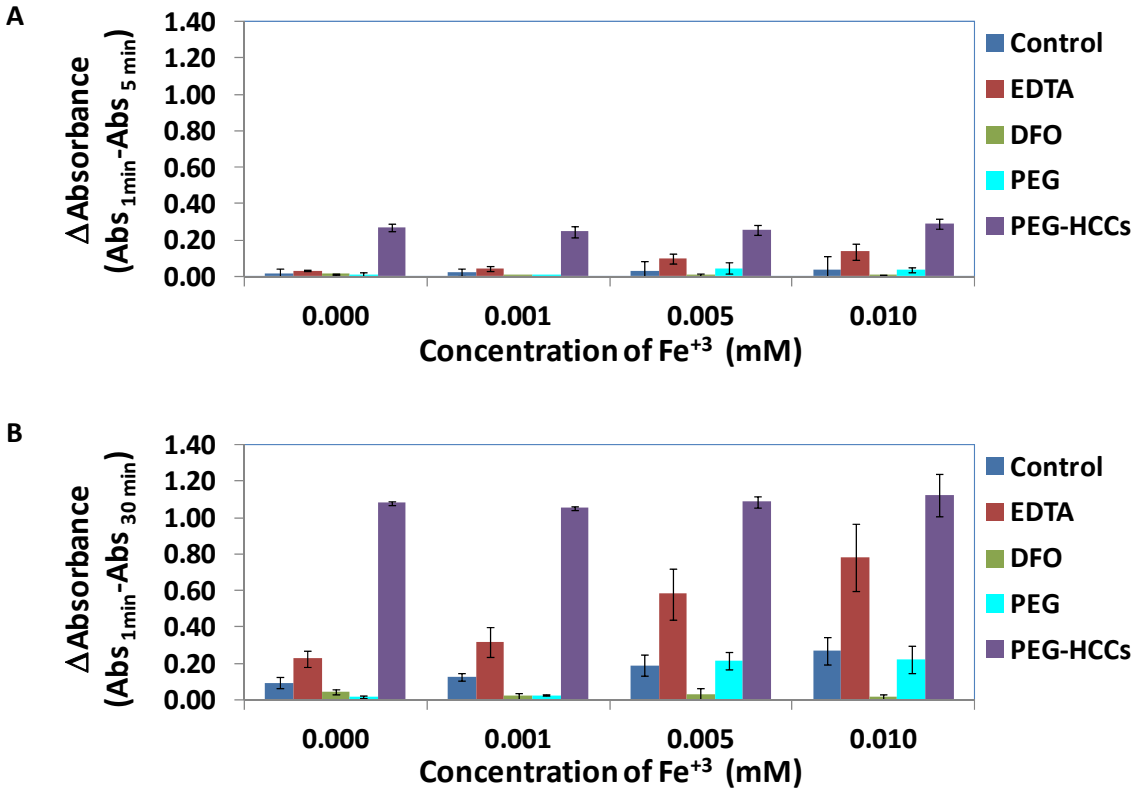

Figure 2.4. Oxidation of the ascorbic acid after (A) 5 min and (B) 30 min of metal addition. Trace of metal was likely present in the buffer as there were different absorbance values for EDTA and DFO compared to no chelator when no extra iron was

added. Overall, these results show that PEG-HCCs in the presence of a reductant such as ascorbate function as potent oxidant, regardless of the presence or absent of Fe^{+3}.

2.3.3. Targeted Binding of PEG-HCCs to Cultured Brain Endothelial Cell Line

Having demonstrated that the PEG-HCCs possessed antioxidant capacity in cell free systems, but that it could be dependent on the presence of reductants such as ascorbate, we evaluated if the PEG-HCCs could be targeted to cultured brain endothelial cells and if they could also alleviate oxidative stress in a biological system. A brain endothelial cell line was chosen because endothelial dysfunction is apparent even after mTBI,[55] and in the case of mTBI, there is minimal detectable brain injury and functional deficits unless hypotension is superimposed.[8] bEnd.3 cells were treated with histamine, which is known to rapidly induce the expression of p-selectin. PEG-HCCs were targeted to p-selectin. In endothelial cells, p-selectin, a cell adhesion molecule is involved in recruiting leukocytes to sites of inflammation and injury. P-selectin is rapidly expressed on endothelial cells following activation by histamine.[49] In this experiment, we treated cells with histamine or 1× PBS to induce p-selectin expression (Figure 2.5). After 15 min, the cells were treated with 1× PBS, PEG-HCCs, or ps/PEG-HCCs. The cells were incubated for another 15 min and after washing and fixing, they were stained with fluorescent antibodies for the presence of PEG to detect PEG-HCCs using an anti-PEG antibody (green), anti-p-selectin antibody(red) to detect p-selectin, and DAPI (nuclear stain; blue). In the cells that are not stimulated by histamine, there is little binding apparent with the p-selectin targeted PEG-HCCs. However, there was a dramatic

increase in binding with the targeted p-selectin antibody bound PEG-HCCs after stimulation by histamine (Figure 2.6, bottom panel). This experiment demonstrates greatly enhanced binding of the targeted PEG-HCCs to endothelial cells in a model that induces expression of a protein, p-selectin.

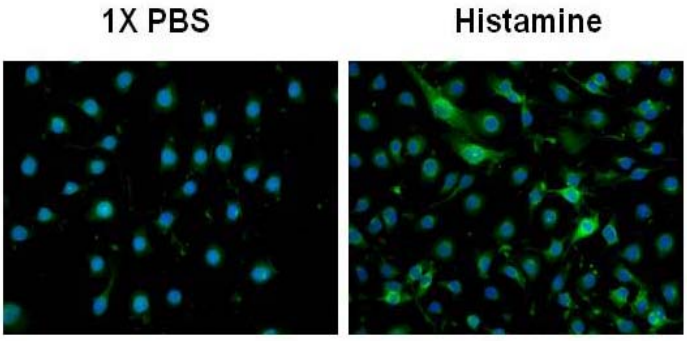

Figure 2.5. b.End3 cells express p-selectin when stressed by histamine. Cells were treated with histamine or the diluent 1× PBS, fixed, and stained for the presence of p-selectin (green) and DAPI (blue). There was considerably enhanced binding of p-selectin antibody following histamine treatment, confirming increased expression of p-selectin.

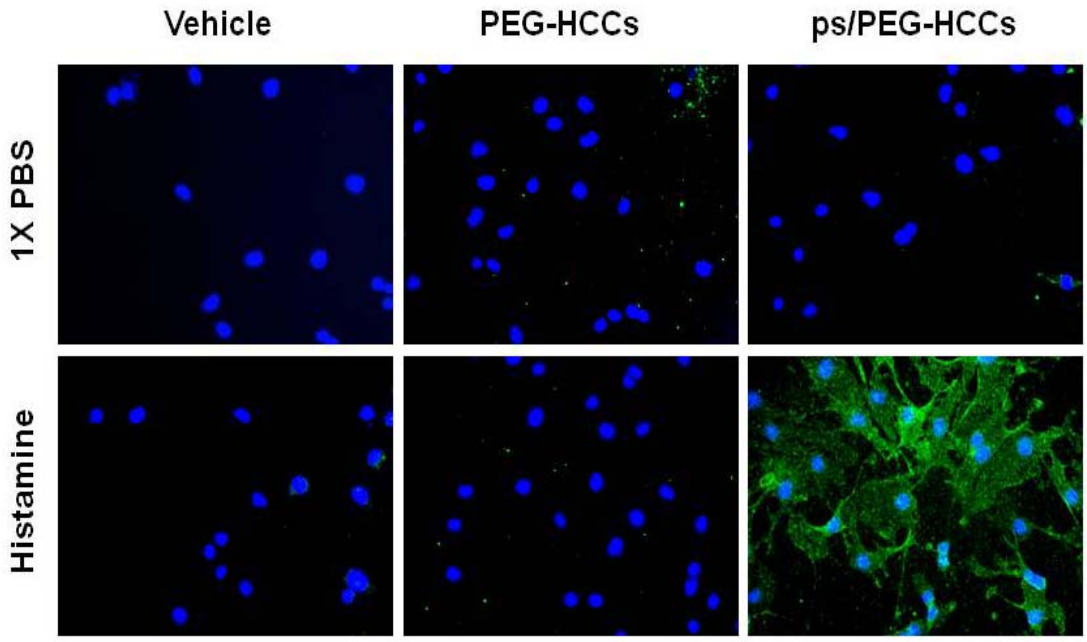

Figure 2.6. b.End3 cells oxidatively stressed by treatment with histamine or 1× PBS were exposed to vehicle, PEG-HCCs or the targeted variant ps/PEG-HCC and stained for the presence of PEG (green) and DAPI (blue). There is considerably enhanced binding of anti-PEG antibody following histamine treatment indicating enhanced binding of the ps/PEG-HCCs to stimulated b.End3 cells.

We then evaluated whether applying the targeted p-selectin antibody to the PEG-HCCs would reduce its antioxidant ability. We tested the protective capacity of the nanoparticles by stressing the cells with Antimycin A and determining the effectiveness of the native or antibody bound PEG-HCCs at reducing levels of oxidative radicals. The level of oxidative stress was measured by DHE fluorescence. An increase in fluorescence is proportional to oxidative stress and is roughly proportional to superoxide

levels, although not specific under all conditions.[47] In this study, we replicated the ability of the PEG-HCCs to reduce DHE fluorescence[56] even when applied after the Antimycin A, and in this study found that ps/PEG-HCCs reduced the level of DHE fluorescence to comparable levels as non-antibody bound PEG-HCCs, and to background (DHE) (Figure 2.7). By comparison, p-selectin antibody by itself had no significant effect on DHE fluorescence.

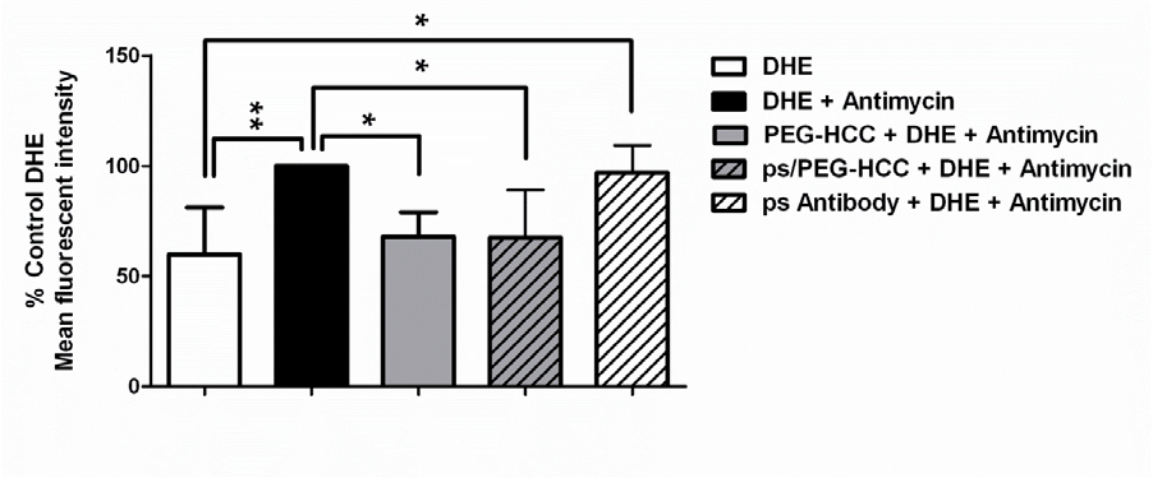

Figure 2.7. PEG-HCCs and targeted ps/PEG-HCCs effectively reduce intracellular oxidative stress. Antimycin A was used to induce intracellular superoxide production. DHE mean fluorescence intensity (indicative of oxidative stress) was measured in cells treated with Antimycin A to induce superoxide production (mean of 5 separate experiments). Results are given as % control (DHE + Antimycin A, black bar) to account for minor differences in DHE concentrations and laser fluctuations. Untargeted (solid grey) PEG-HCCs and targeted ps/PEG-HCCs (striped grey) were effective at reducing

DHE fluorescence after Antimycin A treatment, while treatment with a similar amount of pselectin antibody in the absence of PEG-HCCs (striped white) was not effective.

These results indicate that PEG-HCCs possess antioxidant capacity sufficient be biologically relevant and further, the mechanism does not involve chelation. They were effective in cultured brain endothelial cells *in vitro* when administered following administration of a mitochondrial toxin that induces oxidative stress. They could also be readily targeted to oxidatively stressed brain endothelial cells, and when functionalized for targeting, they retained the ability to alleviate oxidative stress in cultured brain endothelial cells. Overall, these results suggest that targeted PEG-HCCs are potential therapeutics for the cerebrovascular dysfunction from mTBI and the results open additional possibilities for targeting a variety of pathological processes.

Because of the deleterious effects of loss of cerebrovascular responsiveness, even in mild injuries, a therapy that mitigates oxidative injury to endothelial cells should hold promise for the improvement of outcome following mTBI. Furthermore, because there is a major burst of superoxide radical at the time of resuscitation following TBI and hemorrhagic hypotension,[7] treatment at the time of resuscitation may provide a clinically realistic time point that can address at least one pathological event in the care of the TBI patient. Our previous work also showed that the enzymatic antioxidant, PEG-SOD, had only transient and minimal effect in an *in vivo* model of experimental TBI complicated by hypotension and resuscitation,[7] consistent with lack of clinical benefit, and we have preliminary results that PEG-superoxide dismutase was effective in this Antimycin A

assay only when administered at high doses *prior* to the toxcin, whereas *post-treatment* with PEG-HCCs was quite effective. The effectiveness remained in the targeted ps/PEG-HCCs. This characteristic may be a major advantage in considering the use of this agent for treating TBI. Indeed, our preliminary results indicate that PEG-HCCs are able to restore cerebral blood flow following resuscitation in an experimental TBI model[56] when treated during resuscitation. A more fully defined time course, both *in vitro* and *in vivo* will be necessary to confirm the treatment time window and effect on outcome.

We are encouraged that targeting the PEG-HCC using a p-selectin antibody demonstrated a more rapid binding to stressed b.End3 cells. This characteristic may have advantages as a therapeutic agent with enhanced binding to molecules expressed at the site of injury and possibly reduce the total dose administered to the patient. There are many potential such targets, but p-selectin appears particularly promising as there is some added therapeutic benefit in experimental TBI of the antibody itself[57,58] perhaps providing added benefit in addition to the antioxidant ability of the PEG-HCCs. Further comparisons of these different therapeutic approaches will be pursued.

2.4. Conclusions

In summary, we have described a new class of antoxidant materials that were developed to specifically address the cerebrovascular dysfunction that follows TBI. We have shown that PEG-HCC's bound to a p-selectin antibody are rapidly targeted to stressed endothelial cells and are antioxidants capable of reducing oxidative stress-related

fluorescence even when administered after a mitochondrial toxin. It is possible that their effectiveness following injury may be due to the unique mechanism of annihilating radicals, rather than relying on downstream antioxidants that may be depleted in the toxic post-TBI environment. These cumulative characteristics support further testing in TBI models particularly those that involve cerebrovascular dysfunction such as mild TBI and hypotension/resuscitation where loss of cerebral autoregulation and poor reperfusion cause brain injury far beyond that of the TBI alone.[8]

2.5. Acknowledgements

Funding came from the Alliance for NanoHealth through a subcontract from the University of Texas Health Science Center, Houston (Department of Defense, W8XWH-09-2-0139); the Traumatic Brain Injury Consortium, funded by the United States Army (W81XWH-08-2-0141 and W81XWH-08-2-0143); and the Nanoscale Science and Engineering Initiative of the National Science Foundation under NSF Award EEC-0647452 for funding through the NSF Center for Biological and Environmental Nanotechnology.

2.6. References

1. Marcano, D. C.; Bitner, B. R.; Berlin, J. M.; Jarjour, J.; Lee, J. M.; Jacob, A.; Fabian, R. H.; Kent, T. A.; Tour, J. M. Design of poly(ethylene glycol)-

functionalized hydrophilic carbon clusters for targeted therapy of cerebrovascular dysfunction in mild traumatic brain injury. *J. Neurotrauma,* **2012,** accepted.

2. Dickinson, B. C.; Chang, C. J. Chemistry and biology of reactive oxygen species in signaling or stress responses. *Nat. Chem. Biol.*, **2011**, *7*, 504-511.
3. Kontos, H. A.; Wei, E. P. Superoxide production in experimental brain injury. *J. Neurosurg*., **1986**, *64,* 803–807.
4. Hall, E. D.; Andrus, P. K.; Yonkers, P. A. Brain hydroxyl radical generation in acute experimental head injury. *J. Neurochem*., **1993**, *60*, 588–594.
5. Wei, E. P.; Kontos, H. A.; Dietrich W. D.; Povlishock J. T.; Ellis, E. F. Inhibition by free radical scavengers and by cyclooxygenase inhibitors of pial arteriolar abnormalities from concussive brain injury in cats. *Circ. Res*., **1981**. *48*, 95–103.
6. DeWitt, D. S; Prough, D. S. Traumatic cerebral vascular injury: the effects of concussive brain injury on the cerebral vasculature. *J. Neurotrauma,* **2003**, *20,* 795-825.
7. Fabian, R. H.; DeWitt, D. S.; Kent, T. A. In vivo detection of superoxide anion production by the brain using a cytochrome c electrode. *J. Cereb. Blood Flow Meta.,* **1995**, *15*, 242-247.
8. Robertson, C. S.; Cherian, L.; Shah, M.; Garcia, R. G.; Navarro, J. C.; Grill, R. J.; Hand, C. C; Tain, T. S; Hannay, H. J. Neuroprotection with an erythropoietin mimetic peptide (pHBSP) in a model of mild traumatic brain injury complicated by hemorrhagic shock. *J. Neurotrauma*, **2011**, 29, 1156-1166.

9. Ansari, M. A.; Roberts, K. N.; Scheff, S. W. A time course of contusion-induced oxidative stress and synaptic proteins in cortex in a rat model of TBI. *J. Neurotrauma.*, **2008**, *25*, 513-526.

10. Rigg, J. L.; Elovic, E. P.; Greenwald, B. D. A review of the effectiveness of antioxidant therapy to reduce neuronal damage in acute traumatic brain injury. *J. Head Trauma Rehabil.,* **2005***, 20*, 389-391.

11. Marshall, L. F.; Maas, A. I.; Marshall, S. B.; Bricolo, A.; Fearnside, M.; Iannotti, F.; Klauber, M. R.; Lagarrique, J.; Lobato, R.; Persson, L.; Pickard, J. D.; Piek, J.; Servadei, F.; Wellis, G. N.; Morris, G. F.; Means, E. D.; Musch, B. A. Multicenter trial on the efficacy of using tirilazad mesylate in cases of head injury. *J. Neurosurg.,* **1998**, *89*, 519-525.

12. Muizelaar, J. P.; Marmarou, A.; Young, H. F.; Choi, S. C.; Wolf, A.; Schneider, R. L.; Kontos, H. A. Improving the outcome of severe head injury with the oxygen radical scavenger polyethylene glycol-conjugated superoxide dismutase: a phase II trial. *J. Neurosurg*., **1993**, *78*, 375-382.

13. Shuaib, A.; Lees, K. R.; Lyden, P.; Grotta, J.; Davalos, A.; Davis, S. M.; Diener, H.; Ashwood, T.; Wasiewski, W. W.; Emeribe, U. NXY-059 for the treatment of acute ischemic stroke. *N. Engl. J. Med.,* **2007**, *357*, 562-571.

14. Hall, E. D.; Vaishnav, R. A.; Mustafa, A. G. Antioxidant therapies for traumatic brain injury. *Neurotherapeutics,* **2010**, *7*, 51-61.

15. Lucente-Schultz, R. M.; Moore, V. C.; Leonard, A. D.; Price, B. K.; Kosynkin, D. V.; Lu, M.; Partha, R.; Conyers, J. L.; Tour, J. M. Antioxidant single-walled carbon nanotubes. *J. Am. Chem. Soc.,* **2009**, *131*, 3934 – 3941.

16. Chen, Z.; Kobashi, K.; Rauwald, U.; Booker, R.; Fan, H.; Hwang, W. F.; Tour, J. M. Soluble ultra-short single-walled carbon nanotubes. *J. Am. Chem.,* **2006***, 128*, 10568-10571.

17. Price, B. K.; Lomeda, J. R.; Tour, J. M. Aggressively oxidized ultra-short single-walled carbon nanotube having oxidized sidewalls. *Chem. Mater.,* **2009**, *21*, 3917-3923.

18. Berlin, J. M.; Pham, T. T.; Sano, D.; Milas, Z.; Marcano, D.; Leonard, A. D.; Kosynkin, D. V.; Price, B. K.; Lucente-Shultz, R.; Myers, J. N.; Tour, J. M. Effective drug delivery, *in vitro* and *in vivo*, by carbon-based nanovectors non-covalently loaded with paclitaxel. *ACS Nano,* **2010**, *4*, 4621-4636.

19. Berlin, J. M.; Pham, T. T.; Sano, D.; Mohamedali, K. A.; Marcano, D.; Myers, J. N.; Tour, J. M. Noncovalent functionalization of carbon nanovectors with antibody enables targeted drug delivery. *ACS Nano,* **2011**, *5*, 6643-6650.

20. Duncan, R. Polymer therapeutics as nanomedicines: new perspectives. *Curr. Opin. Biotechnol.,* **2011**, *22*, 492-501.

21. Knop, K.; Hoogenboom, R.; Fischer, D.; Schubert U. S. Poly(ethylene glycol) in drug delivery: pros and cons as well as potential alternatives. *Angew. Chem. Int. Ed*., **2010**, *49*, 6288-6308.

22. Alconcel, S. N. S.; Bass, A. S.; Maynard, H. D. FDA-approved poly(ethylene glycol)-protein conjugate drugs. *Polym. Chem*., **2011**, *2*, 1442-1448.

23. Jokerst, J. V.; Lobovkina, T.; Zare, R. N.; Gambhir, S. S. Nanoparticle PEGylation for imaging and therapy. *Nanomedicine*, **2011**, *6*, 715-728.

24. Koob, A. O.; Duerstock, B. S.; Babbs, C. F.; Sun, Y.; Borgens, R. B. Intravenous polyethylene glycol inhibits the loss of cerebral cells after brain injury. *J. Neurotrauma,* **2005***, 22*, 1092-1111.

25. Liu-Snyder, P.; Logan, M. P.; Shi, R.; Smith, D. T.; Borgens, R. B. Neuroprotection from secondary injury by polyethylene glycol requires its internalization. *J. Exp. Biol.,* **2007**, *210*, 1455-1462.

26. Malhotra, R.; Valuckaite, V.; Staron, M. L.; Theccanat, T.; D'Souza, K.; Alverdy, J. C.; Akhter, S. A. High-molecular-weight polyethylene glycol protects cardiac myocytes from hypoxia and reoxygenation-induced cell death and preserves ventricular function. *Am.. J. Physiol. Hearth Circ. Physiol.,* **2011,** *300*, H1733-H1742.

27. Israelsson C.; Bengtsson H.; Kylberg A.; Kullander K.; Lewén A.; Hillered L.; Ebendal T. Distinct cellular patterns of upregulated chemokine expression supporting a prominent inflammatory role in traumatic brain injury. *J. Neurotrauma,* **2008**, *25*, 959-974.

28. Glazer, A. N. Phycoerythrin fluorescence-based assay for reactive oxygen species. *Method. Enzymol.,* **1990**, *186*, 161−168.

29. Cao, G.; Alessio, H. M.; Cutler, R. G. Oxygen-radical absorbance capacity assay for antioxidants. *Free Radical Biol. Med.,* **1993**, *14*, 303-311.

30. Gillespie, K. M.; Chae, J. M.; Ainsworth, E. A. Rapid measurement of total antioxidant capacity in plants. *Nature Protocols*, **2007***, 2*, 867 – 870.

31. Zulueta, M. J.; Frívola, A. ORAC and TEAC assays comparison to measure the antioxidant capacity of food products. *Food Chemistry,* **2009**, 114, 310–316.

32. Prior, R. L.; Hoang, H.; Gu, L.; Wu, X.; Bacchioca, M.; Howard, L.; Hampsch-Woodill, M.; Huang, D.; Ou, B.; Jacob, R. Assays for hydrophilic and lipophilic antioxidant capacity (oxygen radical absorbance capacity (ORACFL)) of plasma and other biological and food samples. *J. Agri. Food Chem.,* **2003**, *51*, 3273–3279.

33. Lucas-Abellan, C.; Mercader-Ross, M. T.; Zafrilla, M. P.; Gabaldon, J. A.; Nunez-Delicado, E. Comparative study of different methods to measure antioxidant activity of resveratrol in the presence of cyclodextrins. *Food Chem. Toxicol.,* **2011**, *49*, 1255-1260.

34. Ou, B.; Hampsch-Woodill, M.; Ronald, P. L. Development and validation of an improved oxygen radical absorbance capacity assay using fluorescein as the fluorescent probe. *J. Agric. Food Chem.,* **2001**, *49*, 4619 – 4626.

35. Raz, E.; Jensen, J. H.; Ge, Y.; Babb, J. S.; Miles, L.; Reaume, J.; Grossman, R. I.; Inglese, M. Brain iron quantification in mild traumatic brain injury: a magnetic field correlation study. *Am. J. Neuroradiol.,* **2011**, *32*, 1851- 1856.

36. Potts, M. B.; Koh, S.; Whetstone, W. D.; Walker, B. A.; Yoneyama, T.; Claus, C. P.; Manvelyan, H. M.; Noble-Haeusslein, L. J. Traumatic injury to the immature brain: inflammation, oxidative injury, and iron-mediated damage as potential therapeutic targets. *NeuroRX*, **2006**, *3*, 143-151.

37. Freeman, L. R.; Keller, J. N. Oxidative stress and cerebral endothelial cells: Regulation of the blood-brain-barrier and antioxidant based interventions. *Biochim. Biophys. Acta*, **2012**, *1822*, 822-829.

38. Wei, Y.; Guo, M. Hydrogen peroxide triggered prochelator activation, subsequent metal chelation, and attenuation of the fenton reaction. *Angew. Chem. Int. Ed. Engl*., **2007**, *46*, 4722-4725.

39. Kocha, T.; Yamaguchi, M.; Ohtaki, H.; Fukuda, T.; Aoyagi, T. Hydrogen peroxide-mediated degradation of protein: different oxidation modes of copper and iron- dependent hydroxyl radicals on the degradation of albumin. *Biochim. Biophys. Acta,* **1997**, *1337*, 319-326.

40. Schopfer, P.; Plachy, C.; Frahry, G. Release of reactive oxygen intermediates (superoxide radicals, hydrogen peroxide, and hydroxyl radicals) and peroxidase in germinating radish seed controlled by light, gibberellin, and abscisic Acid. *Plant Physiol.,* **2001**, *125*, 1591-1602.

41. Baker, M. S.; Gebick, J. M. The effect of pH on the conversion of superoxide to hydroxyl free radicals. *Arch. Biochem. Biophys.,* **1984**, *234*, 258-264.

42. Nicholson, P.; Dean, R. T. The action of nine chelators on iron-dependent radical damage. *Free Rad. Res*., **1993**, *20*, 83-101.

43. Buettner, G. R. Ascorbate autoxidation in the presence of iron and copper chelates. *Free Rad. Res. Comms.,* **1985**, *1*, 349-353.

44. Buettner, G. R. In the absence of catalytic metals ascorbate does not autoxidize at pH 7: ascorbate as a test for catalytic metals. *J. Biochem. Biophys. Methods,* **1988**, *16,* 27-40.

45. Buettner, G. R.; Jurkiewicz, B. A. Catalytic metals, ascorbate and free radicals: combinations to avoid. *Radiat. Res.,* **1996**, *145*, 532-541.

46. Bernhardt, P. V.; Caldwell, L. M.; Chaston, T. B.; Chin, P.; Richardson, D. R. Cytotoxic iron chelators: characterization of the structure, solution chemistry and redox activity of ligands and iron complexes of the di-2-pyridyl ketone isonicotinoyl hydrazone (HPKIH) analogues. *J. Biol. Inorg. Chem.,* **2003**, *8*, 866-880.

47. Richardson, D. R.; Sharpe, P. C.; Lovejoy, D. B.; Senaratne, D.; Kalinowski, M. I.; Bernhardt, P. V. Dipyridyl thiosemicarbazone chelators with potent and selective antitumor activity form iron complexes with redox activity. *J. Med. Chem.,* **2006**, *49*, 6510-6521.

48. McEver, R. P.; Beckstead, J. H.; Moore, K. L.; Marshall-Carlson, L.; Bainton, D.F. GMP-140, a platelet alpha-granule membrane protein, is also synthesized by vascular endothelial cells and is localized in Weibel-Palade bodies. *J. Clin. Invest.,* **1989**, *84*, 92–99.

49. Han, Y. H.; Kim, S. H.; Kim S. Z.; Park, W. H. Antimycin A as a mitochondrial electron transport inhibitor prevents the growth of human lung cancer A549 cells. *Oncol. Rep.,* **2008**, *20*, 689-693.

50. Zhao, H.; Joseph, J.; Fales, H. M.; Sokoloski, E. A.; Levine, R. L.; Vasquez-Vivar, J.; Kalyanaraman, B. Detection and characterization of the product of hydroethidine and intracellular superoxide by HPLC and limitations of fluorescence. *Proc. Nat. Acad. Sci. USA,* **2005**, *102*, 5727-5732.

51. Povlishock, J. T. Traumatically induced axonal injury: pathogenesis and pathological implications. *Brain Pathol., **1992**, 2*, 1-12.

52. Kerem, Z.; Bao, W.; Hammel, K. E. Rapid polyether cleveage via extracellular one-electron oxidation by a brown-rot basidiomycete. *Proc. Nat. Acad. Sci. USA*, **1998**, *95*, 10373-10377.

53. Barz, M.; Luxenhofer, R.; Zentel, R.; Vincent, M. J. Overcoming the PEG-addiction: well-defined alternatives to PEG, from structure-property relationships to better defined therapeutics. *Polym. Chem.,* **2011**, *2*, 1900-1918.

54. Härtel, G.; Fdez-Navamuel, B.; Haseneder, R. Degradation of polyethylene glycol by Fenton reaction: a comparative study. *Water Sci. & Tech.,* **2007**, *55*, 83-87.

55. Golding E. M.; Robertson, C. S.; Fitch, J. C.; Goodman, J. C.; Bryan, R.M. Jr. Segmental vascular resistance after mild controlled cortical impact injury in the rat. *J. Cereb. Blood Flow Metab.,* **2003**, *23*, 210-218.

56. Kent, T. A.; Bitner, B. R.; Berlin, J. M.; Robertson, C. R.; Marcano, D. C.; Fabian, R. H.; Pautler, R. G.; Tour J. M. Antioxidant carbon-based nanotubes: in-vitro characterization and in vivo effects on cerebrovascular regulation following mild traumatic brain injury. *XXVth International Symposium on Cerebral Blood Flow, Metabolism and Function*. **2011**, Madrid, Spain.

57. Whalen, M. J.; Carlos, T. M.; Dixon, C. E.; Robichaud, P.; Clark, R. S.; Marion, D.W.; Kochanek, P. M. Reduced brain edema after traumatic brain injury in mice deficient in p-selectin and intracellular adhesion molecule-1. *J. Leukoc. Biol.,* **2000**, *67*, 160-168.

58. Grady, M. S.; Cody, R. F. Jr.; Maris, D. O.; McCall, T. D.; Seckin, H.; Sharar, H.; Winn, H. R. P-selectin blockade following fluid-percussion injury: behavioral and immunochemical sequelae. *J. Neurotrauma,* **1999**, *16*, 13-25.

2.7. Experimental Contributions

I prepared the PEG-HCCs, performed and analyzed the ORAC, ascorbate oxidation, and benzoate hydroxylation assays. Jane Jarjour, Juhey Lee, and Aakash Jacob ran the replicates for the ascorbic and benzoate hydroxylation assays. Dr. Bitner and Dr. Fabian ran the cells experiments. Dr. Berlin helped with the data analysis.

Chapter 3

Antioxidant Carbon Particles Improve Cerebrovascular Dysfunction Following Traumatic Brain Injury

This chapter was entirely copied from the reference #1 of this section

3.1. Introduction

The neurovascular unit, composed of neuronal and non-neuronal cells such as vascular cells, comprise an integrated network responsible for important physiological functions in the brain including regulation of blood flow.[2] The brain has a high metabolic demand that is met by maintenance of cerebral blood flow (CBF) even under conditions of altered systemic blood pressure, a process termed cerebral autoregulation.[3] It is achieved by the ability of the brain vasculature to dilate in the face of low blood pressure

and constrict during increased blood pressure in order to maintain its perfusion within physiological range. Loss of autoregulaion can expose the brain to hypoperfusion during low blood pressure (hypotension) and to excess blood flow and potentially bleeding during high blood pressure (hypertension). Dysfunction of the neurovascular unit is recognized as a major determinant of patient outcome after brain injury, and it has been hypothesized that therapies that do not address that dysfunction are unlikely to promote recovery.[2] In the case of traumatic brain injury (TBI), damage to the neurovascular unit is manifested under conditions of abnormally low blood pressure, known as hypotension, by loss of cerebral autoregulation and poor restoration of blood flow even after treatment with fluids to increase blood pressure (resuscitation).[4] Loss of autoregulation and poor reperfusion contribute to the clinical finding that TBI with a secondary insult of hypotension predicts poor outcome.[5] This poor outcome is seen even when the brain injury is classified as mild TBI, more commonly known as a concussion. Elevated levels of reactive oxygen species (ROS) such as superoxide (SO)[6,7] are found in the vasculature and have been shown to mediate loss of autoregulatory tone. Along with spikes of ROS following trauma, continued damaging spikes in the level of ROS are observed upon subsequent blood reinfusion during resuscitation;[8] hence, in an effort to stabilize the patient, furtherance of oxidative damage ensues.[9,10] However, blood reinfusion also provides an opportunity to intervene at a clinically realistic time point.

A variety of functionalized carbon materials such as single-walled carbon nanotubes, multi-walled carbon nanotubes, graphene, fullerenes, and/or their derivatives have been studied for the treatment of many diseases, including cancer,[11-13] arthritis,[14-16] inflammation,[17] and neurodegenerative[18-20] diseases. In this report we demonstrate that

poly(ethylene glycol)-functionalized hydrophilic carbon clusters (PEG-HCCs), which are nontoxic carbon particles, rapidly restore cerebral blood flow (CBF) in a TBI/hypotension/resuscitation rat model when administered during resuscitation. Remarkably, along with restoration of CBF, there is a concomitant normalization of both SO and the vasodilator, nitric oxide (NO), levels.

There are currently no antioxidants, including PEG-superoxide dismutase (PEG-SOD) and tirilizad, which have improved patient outcome following TBI.[21] One reason for the lack of effectiveness could be due to the mechanism by which antioxidants trap radicals. Many of these agents modify the radical and depend on the presence of additional detoxifying molecules, such as catalase or glutathione to regenerate the antioxidant.[21] Unfortunately, in the toxic post-injury environment, these downstream molecules are depleted and cannot sufficiently detoxify the damaging radicals. Other agents, such as Vitamin E, are insufficiently regenerated in the face of rising levels of oxidative radicals.[22] While it is probably not possible to administer therapy in time to avert the initial instantaneous spike in ROS following TBI, it should be possible to include an antioxidant at the time of resuscitation and reperfusion to avert the subsequent waves of damaging ROS and their damaging cascades. Therefore, a useful clinical agent would need to act rapidly *in vivo* following the release of the ROS, have high capacity for radical annihilation where there is no need for complementary detoxifying molecules, and it should be effective at a clinically realistic time point such as during the resuscitation.

Particle-based systems are an emerging class of antioxidants with potential advantages over currently available antioxidants[23-32] due to the possibility that they can fully quench radicals without the need for assistance from other detoxifying molecules, as

in the case of superoxide dismutase, for example.[32] HCCs are chemically cut carbon materials, 30- to 40-nm-long and 2- to 3-nm wide, possessing both graphitic and oxidized domains, the latter being the addend locations for PEGylation *via* amide linkages.[34] PEG-HCCs are *in vitro* antioxidants,[35] and they can also be non-covalently loaded with hydrophobic drugs for *in vivo* delivery.[36] PEG-HCCs have the hydrodynamic volume of a moderately sized protein; hence, they are diminutive. Dynamic light scattering (DLS) measurements indicate that they are 50 nm in size at neutral pH.[34] Preliminary studies that used histological analysis of major organs along with hematology measurements demonstrated that the PEG-HCCs have no acute toxicity, and a biodistribution study indicated that they were primarily cleared through the kidneys with a blood half-life of 2 to 3 h.[34] Finally, PEG-HCCs are room-temperature stable for months, biocompatible with cultured brain endothelial cells (bEnd.3), and they can be targeted with monoclonal antibodies, such as P-selectin, to specific cellular locations on tissue of interest.[35,36]

It is conjectured that PEG-HCCs' graphitic structural domains cause them to be antioxidants by radical annihilation (Figure 3.1) rather than by radical transfer to a less reactive radical form as is required for most other antioxidants. Thus, PEG-HCCs can detoxify many radicals at each of their graphitic domains, as demonstrated by our previous finding that PEG-HCCs are potent antioxidants after generation of SO, one of the damaging ROS overproduced during TBI.[35] It is thus possible that *in vivo* the PEG-HCCs can annihilate toxic ROS during periods of trauma when other antioxidants are overwhelmed due to a lack of supporting detoxifying molecules. Hence, PEG-HCCs alone may function as effective antioxidants and have sufficient capacity for radical annihilation to be used therapeutically during periods of intense ROS generation. These

multifaceted properties suggest that the PEG-HCCs could be exciting constructs for clinical evaluation.

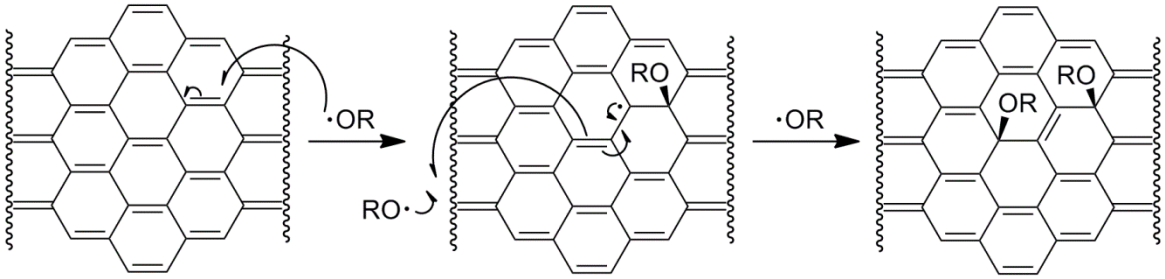

Figure 3.1. The suggested radical annihilation mechanism at a graphitic domain of the carbon particle. Two additions of RO· result in the loss of two C–C pi-bonds and the formation of two new C–O sigma bonds and one new C–C pi bond, without any radical species remaining. Only one regioisomer is shown, though many others can form by resonance of the conjugated radical.

3.2. Experimental Procedures

3.2.1. Preparation and Characterization of the PEG-HCCs

PEG-HCCs were prepared as previously described.[34] These particles are soluble in water and PBS. Optical spectrum (Figure C1, Appendix C), thermogravimetric analysis (TGA, Figure C1-B), and X-ray photoelectron spectroscopy (XPS, Figure C1-C, Appendix C) measurements were consistent with the previously reported[33]

characterization of these materials. According to the TGA, the PEG-HCCs used in the current studies were 84% PEG by weight.

3.2.2. DAF-2DA Staining in bEnd.3 Cells

bEnd.3 cells (ATCC) were grown in Dulbecco's modified Eagle's medium (4 mM L-glutamine adjusted to contain 1.5 g/L sodium bicarbonate and 4.5 g/L glucose, 90%; fetal bovine serum, 10% (Atlanta Biological) in an incubator set to 37 °C with 5% CO_2. Aliquots of 60,000 cells in 0.5 mL were added directly onto sterile 25 mm round cover glasses inside 6 well plates. The cells were allowed to attach for 15 min after which an additional 1.5 mL of media was added and then the cells were placed in an incubator and allowed to grow for 48 h. PEG-HCCs were added to each well to obtain the following concentrations: 0 mg/L, 0.1 mg/L, 1 mg/L, 10 mg/L, 20 mg/L and 30 mg/L (triplicate). The cells were incubated for 1 h with the specific PEG-HCC concentrations after which DAF-2DA at a final concentration of 5 mM was added to each well and incubated for an additional 5 min. The cells were then washed 3× with PBS and fixed with 4% paraformaldehyde for 15 min. The cells were washed 3× with PBS and then the cover glasses were attached to glass slides and coverslipped. A Nikon eclipse 80i microscope set to FITC was used to capture ten 40X fields per slide. Five cells from each 40X field were analyzed using NIS Elements software. An auto detect region of interest (ROI) function was used to select the cells and calculate their mean intensity and area. The intensity/area/exposure was calculated. An ANOVA was performed using the means followed by post tests using the Bonferroni method.

3.2.3. Internalization of the PEG-HCCs

Confocal microscopy showed that the PEG-HCCs were taken up by the endothelial cells (Figure C2 – Figure C4, Appendix C). Staining against the PEG for the mock (Figure C2-B, Appendix C) and PEG (Figure C2-E, Appendix C) treated cells showed similar low intensity signals, indicating that uptake was dependent on the presence of carbon particles but not the PEG. The experiment was set as follow: bEnd.3 cells (~50,000/well, passage less than 30 times) were grown on coverslips placed in 6-well plates with 5 mL of complete media (high glucose Dulbecco's modified Eagle's medium (Gibco) formulated to contain 4 mM L-glutamine, 3.7 g/L sodium bicarbonate, 4.5 g/L D-glucose, 1 mM sodium pyruvate, 90%; fetal bovine serum, 10%; 1x pen-strep). Cells were later treated with 5 mL of complete medium in a 1:1 mixture with water (Mock treatment), a solution of PEG in water, or a solution of PEG-HCCs in water. The final concentration of the PEG and PEG-HCCs in the treatment solution was 4 mg/L. Cells were incubated at 37 °C with 5% CO_2 for 5.5 h. The cells were then washed with ice cold PBS, then a solution of glycine (50 mM)/NaCl (100 mM), followed again by ice cold PBS in order to remove the carbon particles that are weakly attached to the membrane. Cells were fixed with 4% paraformaldehyde, then cell membranes were stained with Wheat Germ Agglutinin 594 before being permeabilized with PBT (PBS containing 0.1% Triton X-100), blocked with 5% BSA in PBT, and immunostained with a primary antibody against PEG (Epitomics, PEG Rabbit Monoclonal Antibody, RabMAb® #: 2061-1) and an Alexa-633 conjugated secondary antibody, with DAPI used as a nuclear counterstain. Each set of images was taken with the same settings on a Zeiss LSM 510 META confocal microscope, and are shown at the same brightness/contrast levels.

3.2.4. Animal Experiments

A TBI/hypotension/resuscitation rat model was chosen to simulate a typical case in the field: 50 min after controlled cortical impact TBI and loss of blood, lactacted Ringers solution was administered in an ambulance "prehospital" phase, then after further delay of 30 min, definitive "hospital" care consisted of therapy administration, oxygenation and blood infusion. The model is described as follows: In Phase 1, Long Evans rats (250 to 300 g) underwent sham injury or mild cortical compression injury TBI (3 m/s, 2.5 mm deformation, Table C1) to one hemisphere of the brain. Sham animals underwent identical surgical preparation as the TBI group except they did not receive the cortical impact used to produce mild TBI. Both sham and mild TBI animals had hemorrhagic hypotension produced by controlled blood withdrawal to reach a mean arterial blood pressure (MAP) of 40 mm Hg in a decelerating protocol to mimic trauma blood loss. In order to simulate field resuscitation and ambulance transport (Phase 2), the rats received intravenous (i.v.) lactated Ringer's solution for initial resuscitation. Then hospital care (Phase 3) was simulated by administering a single dose of PEG-HCCs (2 mg/kg) or a diluent vehicle, phosphate buffered saline (PBS), *via* a 5 min i.v. tail vein administration. This was followed by oxygenation and blood reinfusion. Beginning with Phase 4, there was extensive physiological monitoring included MAP, arterial blood gases, intracranial pressure and non-invasive spatial brain perfusion using laser Doppler flowmetry (LDF, Periscan).[37]

3.3. Results and Discussion

First, by confocal microscopy studies, we confirmed that the PEG-HCCs are rapidly internalized by murine brain endothelial (b.End3) cells (Figure C2 – Figure C4, Appendix C). Brain endothelial cells were chosen because, as discussed, the vasculature is a major and potentially treatable injury in the TBI and secondary injury paradigm that results in loss of autoregulation.[4,6] A series of *in vitro* studies showed that when oxidative stress was induced in b.End.3 cells[38] by treatment with the mitochondrial toxin, antimycin A,[23,26,35,39] the intracellular oxidative stress could be reduced in a dose-dependent manner by treatment with PEG-HCCs. Antimycin A blocks electron flow through complex III of the mitochondrial electron transport chain that results in the formation of SO.[39] The amount of oxidative radical expression was measured as a proportion of dihydroethidium (DHE) fluorescence.[40] PEG-HCC treatment was effective even 10 min after toxin exposure, while neither PEG-SOD nor the small molecule antioxidant, phenyl-α-*tert*-butyl nitrone (PBN)[8,41,42] was effective in the post-toxin-treated cells. The latter two traditional antioxidants were only effective pre-toxin exposure, and then only at a 10 to 30× higher dose (Figure 3.2A). Furthermore, at higher doses of antimycin A where significant cell death could be induced, post-treatment with PEG-HCCs was able to restore cell viability to more than 65% of baseline. Conversely, no protective effect from post-treatment with either PEG-SOD or PBN could be observed (Figure 3.2B). These studies underscore the efficacy of the PEG-HCCs to annihilate ROS that would otherwise have resulted in cell death; the poor performance of conventional antioxidants is also noted.

Furthermore, it was found that PEG-HCCs are selective antioxidants as additional *in vitro* experiments in bEnd.3 cells indicated that the PEG-HCCs do not quench NO

sensitive fluorescence of diaminofluorescein diacetate (DAF-2DA)[42] associated with spontaneous NO release from these cells (Figure C5 and Figure C6, Appendix C). This may be significant for eventual clinical efficacy since physiological levels of NO are essential for many processes, including blood vessel dilation and autoregulation.[43] An effective antioxidant treatment for TBI must annihilate toxic species such as SO without impairing the normal levels and functions of NO.

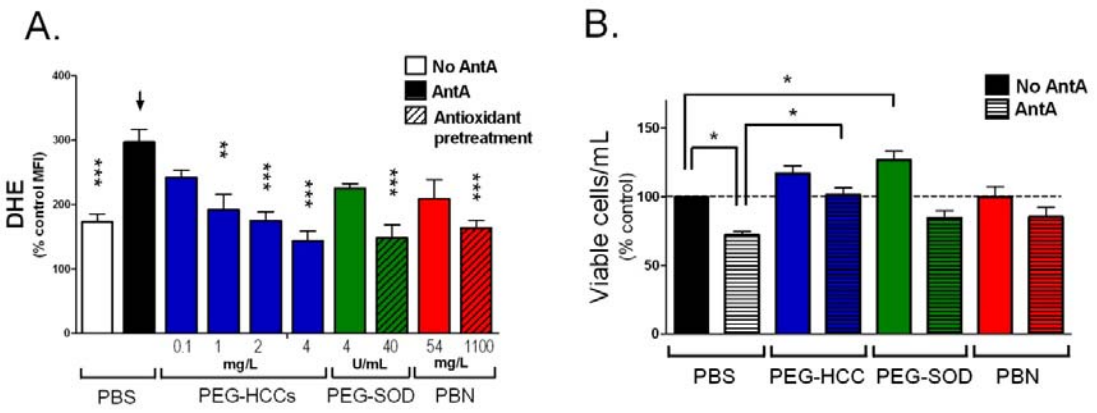

Figure 3.2. PEG-HCCs protect brain endothelial cells from oxidative stress when administered after an insult. (A) Intracellular ROS levels for b.End3 cells as determined by DHE staining and flow cytometry. The mean fluorescent intensity (MFI) of 10,000 cells/group was normalized to the group not treated with antimycin A (AntA in graphs) or DHE. Phosphate buffered saline (PBS, black bar) or antioxidant treatments (blue, green, and red solid bars) were given after antimycin A. Some antioxidants were administered prior to antimycin A (striped bars). Additional controls are shown in Figure C6 (Appendix C). * p-value < 0.05; ** p-value < 0.01; *** p-value < 0.001 compared to bar with arrow. Results are a mean of five separate experiments. (B) Cell survival relative to

control for b.End3 cells given different treatments. The cells were either cultured in the presence of PEG-HCCs, PEG-SOD or PBN alone (solid bars) or the cells were first treated with a dose of antimycin A titrated to kill 30% of the cells followed by treatment with PEG-HCCs, PEG-SOD or PBN (striped bars). Results are a mean of seven separate experiments. Error bars are s.e.m. ANOVA with Bonferroni post test was used to calculate statistics. * p-value <0.05.

PEG-HCCs were next evaluated *in vivo.* The TBI model used here is intended to mimic the common clinical situation in which TBI is accompanied by a systemic injury resulting in hypotension (low blood pressure). There is minimal evidence of either behavioral or histological injury with either TBI or hypotension alone, but with the superimposition of hemorrhagic hypotension and subsequent resuscitation, there is marked expansion of lesion size and behavioral impairment (Figure C7, Appendix C).[37] Reperfusion CBF was reduced in proportion to the increase in injury, supporting the hypothesis that this is primarily a vasculature injury. The loss of autoregulation and poor reperfusion originating in the brain endothelium contribute to injury even in the setting of mild TBI. This highlights that while the blood-brain barrier becomes compromised following mild TBI[44] potentially allowing access of agents such as PEG-HCCs to the brain itself, the major treatable injury in the TBI and secondary injury paradigm is to the brain vasculature manifested by loss of CBF and poor reperfusion.

Using this TBI/hypotension/resuscitation rat model, treatment was chosen to simulate a typical case in the field: 50 min after controlled cortical impact TBI and loss of blood, lactacted Ringers solution was administered in an ambulance “prehospital” phase,

then after further delay of 30 min, definitive "hospital" care consisted of therapy administration, oxygenation and blood infusion. The model is outlined in the Injury Model Table 1 and described as follows: In Phase 1, Long Evans rats (250 to 300 g) underwent sham injury or mild cortical compression injury TBI (3 m/s, 2.5 mm deformation, Table C1, Appendix C) to one hemisphere of the brain. Sham animals underwent identical surgical preparation as the TBI group except they did not receive the cortical impact used to produce mild TBI. Both sham and mild TBI animals had hemorrhagic hypotension produced by controlled blood withdrawal to reach a mean arterial blood pressure (MAP) of 40 mm Hg in a decelerating protocol to mimic trauma blood loss. In order to simulate field resuscitation and ambulance transport (Phase 2), the rats received intravenous (i.v.) lactated Ringer's solution for initial resuscitation. Then hospital care (Phase 3) was simulated by administering a single dose of PEG-HCCs (2 mg/kg) or a diluent vehicle, phosphate buffered saline (PBS), *via* a 5 min i.v. tail vein administration. This was followed by oxygenation and blood reinfusion. Beginning with Phase 4, there was extensive physiological monitoring included MAP, arterial blood gases, intracranial pressure and non-invasive spatial brain perfusion using laser Doppler flowmetry (LDF, Periscan).[37]

Table 3.1. Injury Model

Phase 1	**Phase 2**	**Phase 3**	**Phase 4**
Injury and	**Prehospital**	**Definitive**	**Test**
hemorrhage	**ambulance**	**hospital**	**outcome**

(50 min)	(30 min)	(30 min)	(6 h)
• Ventilate (air) • Mild TBI • Withdraw blood to MAP 40 mm Hg	• Ventilate (air) • Initial resuscitation saline MAP ≥ 50 mm Hg	• Give drug • Ventilate with 100% oxygen • Reinfuse blood • Saline to MAP ≥ 60 mm Hg	• 0-6 h Monitor cerebral hemodynamics • 6 h Determine SO and NO levels

Remarkably, PEG-HCCs restored cerebral perfusion and normalized the oxidative radical profile. Rats received a single dose of PEG-HCCs (2 mg/kg) or PBS at the beginning of the blood resuscitation (Phase 3). CBF was measured for 6 h from the brain surface with LDF (Phases 3 and 4). Just before the 6 h mark, rats were injected with dyes for SO (DHE) and NO (DAF-2DA) detection, and perfusion fixed.[42] Systemic injection of these dyes and a short circulation time was able to identify vascular expression of these radicals since the dyes are concentrated in the vasculature with less chance of diffusion into the brain parenchyma.[42] LDF-relative CBF (rCBF) is shown in the series of Figures 3.3A-C. Figure 3.3A illustrates changes in rCBF in the region of the traumatic injury. Hypotension following TBI significantly reduced rCBF. In the vehicle-treated TBI group, rCBF was only partially restored by reinfusion of shed blood while rCBF returned rapidly to baseline levels following administration of the PEG-HCCs and blood. The duration of the PEG-HCC effect was from 2 to 3 h, at which time both groups showed a decline in rCBF; this duration of treatment effect is consistent with the 2 to 3 h blood half-life of PEG-HCCs[34] and also consistent with the prolonged anesthesia time.

Figure 3.3B shows a qualitatively similar effect in the peri-traumatic region (region around the injury), with rCBF returning to baseline in the PEG-HCC-treated group, while remaining depressed in the vehicle-treated group. No effect on rCBF of either group in the contralateral cortex (Figure 3.3C) indicates that the outcomes seen in the lesion and peri-lesional regions were not artifactual and were specific for injured areas. Additional experiments in a model to simulate linear flow show that there was no effect of PEG-HCCs on the LDF signal used to measure CBF, nor did the PEG-HCCs influence systemic blood pressure or physiological variables (Figure C8, Table C2, Appendix C). These results demonstrated that in a model of TBI/hypotension/resuscitation, the PEG-HCCs rapidly restore the cerebral perfusion and that the PEG-HCCs were directly improving CBF in the injured area.

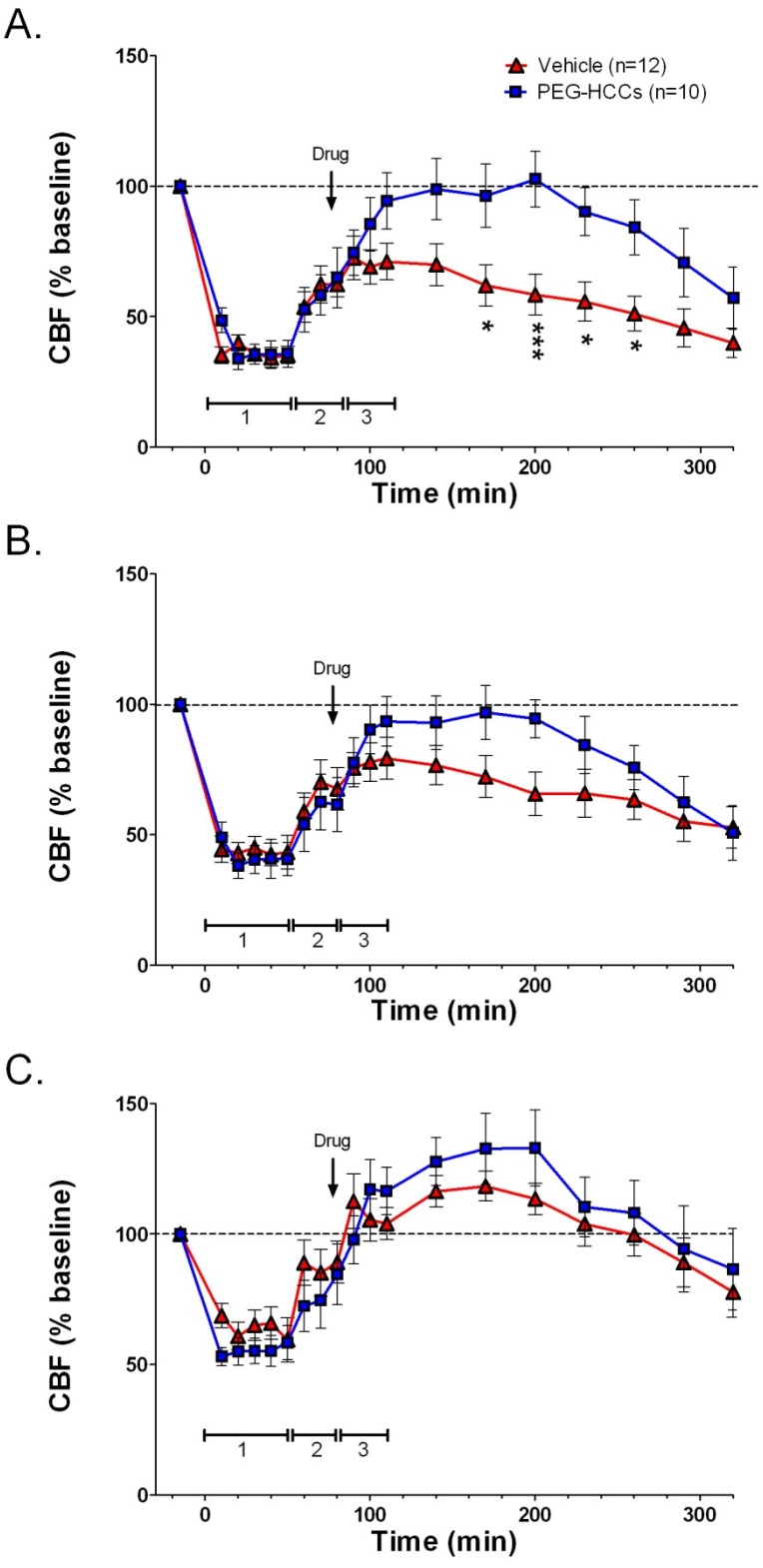
A.
Vehicle (n=12)
PEG-HCCs (n=10)
Drug
CBF (% baseline)
Time (min)
1
2
3
*
***
*
*
B.
Drug
CBF (% baseline)
Time (min)
1
2
3
C.
Drug
CBF (% baseline)
Time (min)
1
2
3

D.

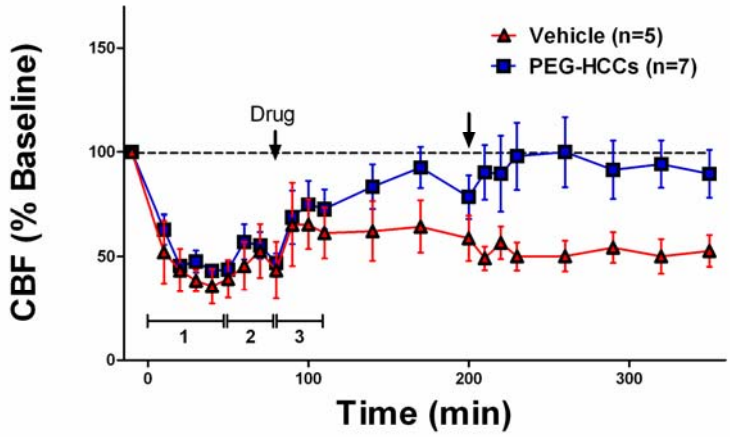
Vehicle (n=5)
PEG-HCCs (n=7)
Drug
CBF (% Baseline)
Time (min)
150
100
50
0
0
100
200
300
1
2
3

E.

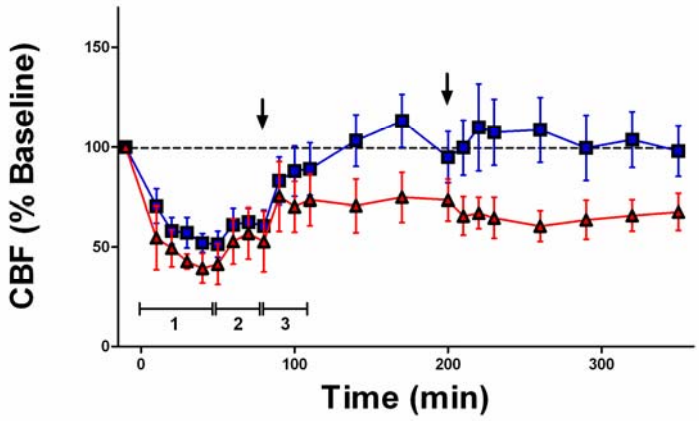
CBF (% Baseline)
Time (min)
150
100
50
0
0
100
200
300
1
2
3

F.

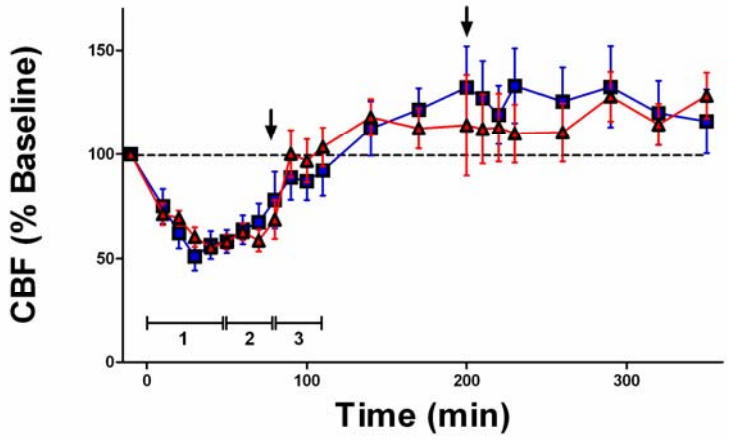

Figure 3.3. PEG-HCCs treatment rapidly improves CBF in the injured cortex in rats with TBI plus hypotension after a single dose and two sequential doses. Laser Doppler was used to measure CBF given as a percent of the baseline (pre-injury) CBF. Relative CBF below 100 (dashed line) indicate low CBF. Relative CBF after a single drug dose (arrow) administered during the "hospital phase" in the (A) injured cortex (B) peri-lesional cortex, and (C) contralateral cortex; the effect of sequential dosing in a second set of rats treated with drug during the "hospital phase" and again 2 h later (arrows) are shown in (D) injured cortex (E) peri-lesional cortex, and (F) contralateral cortex. Drugs (PEG-HCC or PBS vehicle) were given where indicated. Time 0 min indicates when the TBI was performed. Phase 1 = TBI+hypotension; Phase 2 = saline during "ambulatory phase"; Phase 3 = vehicle or PEG-HCC treatment and blood reinfusion during "hospital phase". Error bars are S.E.M. Repeated measures ANOVA with Bonferroni post test was used to calculate statistics. * p-value <0.05 and *** p-value <0.01 for vehicle (red) compared to PEG-HCCs (blue). Note that 100% of CBF is considered "normal". Approximately 50% and 150% are considered low and high cerebral blood flow, respectively.

We next determined whether treatment was able to modify the hypothesized targets, SO while restoring NO. The injection of PEG-HCC antioxidants significantly reduced SO levels in the vasculature (Figures 3.4A-C), underscoring that this is primarily a vasculature injury. Concomitantly, treatment with PEG-HCCs completely restores vascular NO levels (Figures 3.4D-E). This duality of modes in the resuscitative phase of treatment, specifically decreasing SO and normalizing NO, is highly unusual in such injury models.

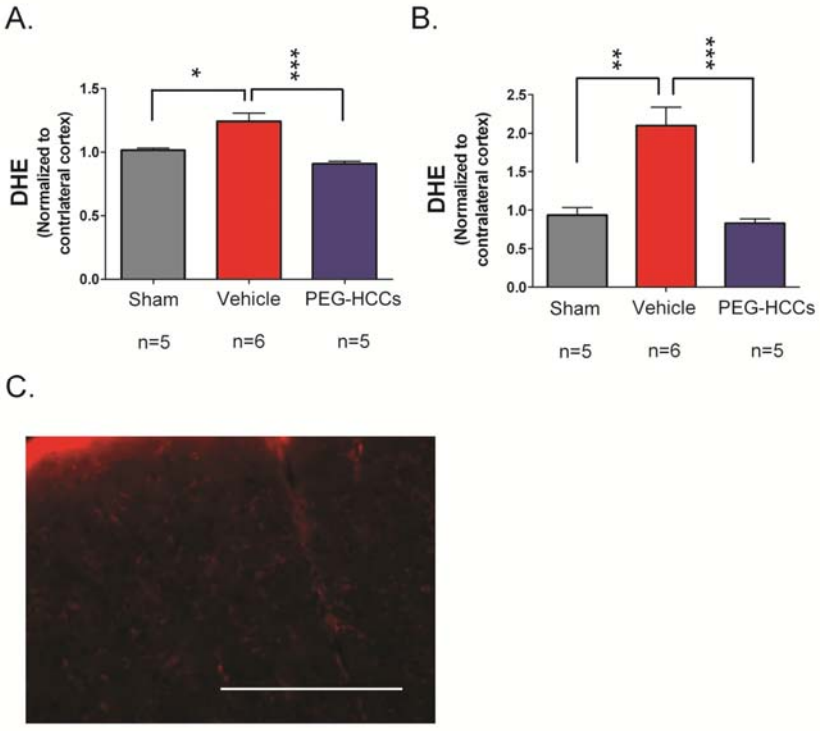

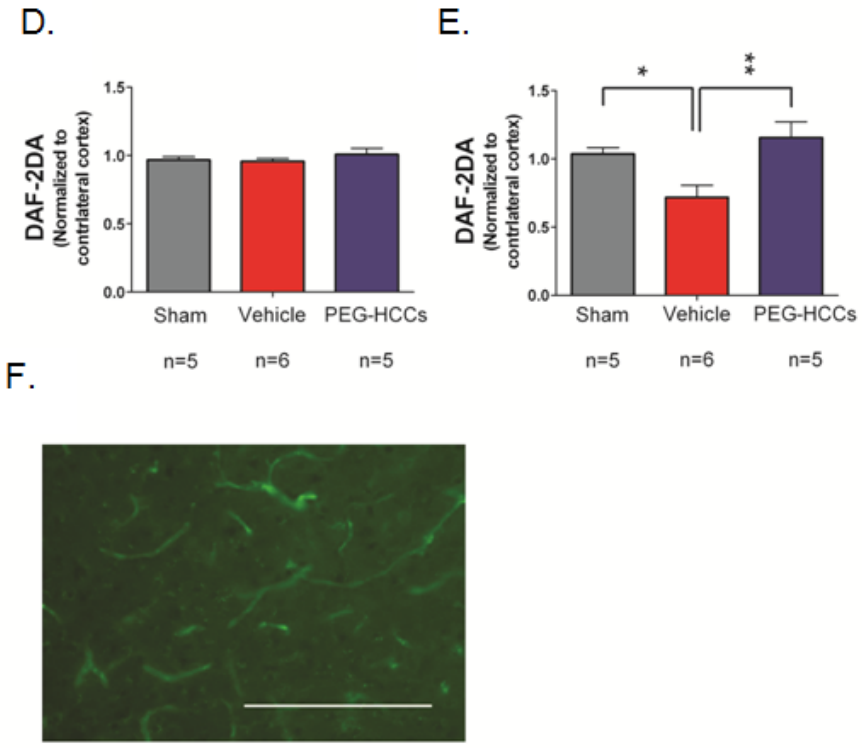

Figure 3.4. Fluorescence after systemic injection of radical-sensitive dyes measured in the brain and vasculature following TBI. DHE levels (proportional to SO and oxidative radicals) in the (A) brain parenchyma (cortex) and (B) blood vessels of sham (no TBI) surgery rats or rats with TBI + hypotension with vehicle or PEG-HCC treatment. The ipsilateral cortex (brain hemisphere with TBI) was normalized to the contralateral cortex. PEG-HCC treatment was able to reduce DHE staining (blue column) compared to vehicle treatment (red column), with a larger magnitude of effect seen in the blood vessels than the brain parenchyma, suggesting that the cerebrovascular is likely the site of major dysfunction in the TBI model. (C) Microscopy of DHE staining (red) in the injured cortex; scale bar = 200 μm showing the prominent fluorescence in vascular structures (long thin structures). DAF-2DA levels (indicative of NO levels) are shown in (D) for the

brain parenchyma (cortex) and (E) blood vessels of sham surgery rats or rats with TBI + hypotension with vehicle or PEG-HCCs treatment. (F) Microscopy of DAF-2DA staining (green) in the injured cortex. NO-related fluorescence was reduced following TBI and restored to levels comparable to the sham-treated animals. NO is important for vasodilation and increased CBF, therefore, increased DAF-2DA staining with PEG-HCC treatment correlates well with the improved CBF from Figure 3.3. Both DHE and DAF-2DA fluorescence was normalized in each animal to the contralateral cortex to account for minor differences in dye administration and circulation times. For all data in this Figure, error bars are S.E.M. D'Agostino-Pearson normality test was used on data and no groups had a p-value <0.05. ANOVA with Bonferroni post test was used to calculate statistics. * p-value < 0.05; ** p-value < 0.01; *** p-value < 0.001. N=5-6 animals/group with 10 brain sections analyzed per animal. Scale bar = 200 μm.

3.4 Conclusions

Non-toxic PEG-HCCs are inherently active particle-based drugs that have efficacy at the critical neurovascular unit, restoring CBF after a mild TBI. Since reduction in CBF following even mild TBI is a major cause of poor outcome, the results shown for restoring CBF while normalizing SO and NO levels primarily in the cerebral vasculature are suggestive of a treatment that could vastly improve the recovery and long-term neurological prognosis for traumatized patients, and it has implications for

other acute disorders such as stroke in which reperfusion-based ROS release is associated with extension and propagation of injury.[8]

3.5. Acknowledgments

Funding was provided by the Mission Connect Mild Traumatic Brain Injury Consortium, funded by the Department of Defense: W81XWH-08-2-0141, W81XWH-08-2-0143 and W81XWH-08-2-0132. We also thank the support of the Alliance for NanoHealth through a subcontract from the University of Texas Health Science Center, Houston (Department of Defense: W8XWH-07-2-0101); Nanoscale Science and Engineering Initiative of the National Science Foundation under NSF Award EEC-0647452 for funding through the NSF Center for Biological and Environmental Nanotechnology; the Graduate Fellows in K-12 education at Baylor College of Medicine, funded by the National Science Foundation (Track 2, 0440525); the BCM DERC Pilot and Feasibility Award (P30DK079638-02); NIH R01 HL095586; the BCM Cytometry and Cell Sorting Core with funding from the NIH (NCRR grant S10RR024574, NIAID AI036211 and NCI P30CA125123); and an NIH Training Grant from the National Heart, Lung, and Blood Institute (T32 HL007676).

3.6. References

1. Bitner, B. R.; Marcano, D. C.; Berlin, J. M.; Fabian, R. H.; Cherian, L.; Culver, J. C.; Dickinson, M. E.; Robertson, C. S.; Pautler, R. G.; Kent, T. A.; Tour, J. M.

Antioxidant carbon particles improve cerebrovascular dysfunction following traumatic brain injury. *ACS Nano*, **2012**, accepted.

2. Lo, E. H. Experimental models, neurovascular mechanisms and translational issues in stroke research. *Br. J. Pharmacol.,* **2008**, *88*, S396-S405.
3. Paulson, O. B.; Strandgaard, S.; Edvinsson, L. Cerebral autoregulation. *Cerebrovasc. Brain. Metab. Rev*., **1990,** *2*, 161-192.
4. DeWitt, D. S.; Prough, D. S. Traumatic cerebral vascular injury: the effects of concussive brain injury on the cerebral vasculature. *J. Neurotrauma,* **2003**, *20*, 795-825.
5. Butcher, I.; Maas, A. I.; Lu, J.; Marmarou, A.; Murray, G.D.; Mushkudiani, N.A.; McHugh, G. S.; Steyerberg, E. W. Prognostic value of admission blood pressure in traumatic brain injury: results from the IMPACT study. *J. Neurotrauma,* **2007**, *24*, 294-302.
6. Kontos, H. A.; Wei, E. P. Superoxide production in experimental brain injury. *J. Neurosurg.,* **1986**, *64*, 803-807.
7. Kehrer, J. P. Free radicals as mediators of tissue injury and disease. *Crit. Rev. Toxicol.,* **1993**, *23*, 21-48.
8. Fabian, R. H.; DeWitt, D. S.; Kent, T. A. *In vivo* detection of superoxide anion production by the brain using a cytochrome c electrode. *J. Cereb. Blood Flow Metab.,* **1995**, *15*, 242-247.
9. Halliwell, B.; Gutteridge, J. M. C.; eds. *Free Radicals in Biology and Medicine*. Oxford University Press: Oxford, New York, 1999; pp xxxi-936.

10. Ansari, M. A.; Roberts, K. N.; Scheff, S. W. A time course of contusion-induced oxidative stress and synaptic proteins in cortex in a rat model of TBI. *J. Neurotrauma,* **2008**, *25*, 513-526.

11. Murakami, T.; Sawada, H.; Tamura, G.; Yudasaka, M.; Iijima, S.; Tasuchida, K. Water-dispersed single-wall carbon nanohorns as drug carriers for local cancer chemotherapy. *Nanomedicine,* **2008**, *3*, 453–463.

12. Hampel, S.; Kunze, D.; Haase, D.; Krämer, K.; Rauschenback, M.; Ritschel, M.; Leonhardt, A.; Thomas, J.; Oswald, S.; Hoffmann, V.; *et al*. Carbon nanotubes filled with a chemotherapeutic agent: a nanocarrier mediates inhibition of tumor cell growth. *Nanomedicine,* **2008**, 3, 175–182.

13. Liu, Z.; Robinson, J. T.; Sun, X.; Dai, H. PEGylated nanographene oxide for delivery of water-insoluble cancer drugs. *J. Am. Chem. Soc.,* **2008**, *130*, 10876–10877.

14. Yudoh, K.; Karasawa,R.; Masuko, K.; Kato, T. Water-soluble fullerene (C60) inhibits the development of arthritis in the rat model of arthritis. *Int. J. Nanomedicine,* **2009**, *4*, 217–225.

15. Nakamura, M.; Tahara, T.; Ikehara, Y.; Murakami, T.; Tsuchida, K.; Iijima, S.; Waga, I.; Yudasaka, M. Single-walled carbon nanohorns as drug carriers: adsorption of prednisolone and anti-inflammatory effects on arthritis. *Nanotechnology,* **2011**, *22*, 465102

16. Girase, B.; Shah, J.; Misra, R. D. Cellular mechanics of modulated osteoblasts functions in graphene oxide reinforced elastomers. *Adv. Eng. Mater.,* **2012**, *14*, B101–B111.

17. Huang, S.; Ho, C.; Lin, C.; Fang, H.; Peng, Y. Development and biological evaluation of C_{60} fulleropyrrolidine-thalidomide dyad as a new anti-inflammation agent. *Bioorg. Med. Chem.,* **2008**, *16*, 8619-8626.

18. Makarova, E.G.; Gordon, R.Y.; Podolski, I.Y. Fullerene C_{60} prevents neurotoxicity induced by intrahippocampal microinjection of amyloid-*β* peptide. *J. Nanosci. Nanotechnol.,* **2012**, *12*, 119-126.

19. Zhang, Y.; Bai, Y.; Yan, B. Functionalized carbon nanotubes for potential medicinal applications. *Drug Discov. Today*, **2010**, *15*, 428-435.

20. Lv, M.; Zhang, Y.; Liang, L.; Wei, M.; Hu,W.; Li, X.; Huang, Q. Effect of graphene oxide on undifferentiated and retinoic acid-differentiated SH-SY5Y cells line. *Nanoscale,* **2012**, *4*, 3861.

21. Muizelaar, J. P.; Marmarou, A.; Young, H. F.; Choi, S. C.; Wolf, A.; Schneider, R. L.; Kontos, H. A. Improving the outcome of severe head injury with the oxygen radical scavenger polyethylene glycol-conjugated superoxide dismutase: a phase II trial. *J. Neurosurg.,* **1993**, *78*, 375-382.

22. Wang, X.; Quinn, P. J. Vitamin E and its function in membranes. *Prog. Lipid Res.,* **1999**, *38*, 309–336.

23. Lucente-Schultz, R. M.; Moore, V. C.; Leonard, A. D.; Price, B. K.; Kosynkin, D. V.; Lu, M; Partha, R.; Conyers, J. L.; Tour, J. M. Antioxidant single-walled carbon nanotubes. *J. Am. Chem. Soc*., **2009**, *131*, 3934-3941.

24. Ali, S. S.; Hardt, J. I.; Dugan, L. L. SOD Activity of carboxyfullerenes predicts their neuroprotective efficacy: a structure-activity study. *Nanomedicine-UK,* **2008**, *4*, 283-294.

25. Ali, S. S.; Hardt, J. I.; Quick, K. L.; Kim-Han, J. S.; Erlanger, B. F.; Huang, T. T.; Epstein, C. J.; Dugan, L. L. A Biologically effective fullerene (C60) derivative with superoxide dismutase mimetic properties. *Free Radic. Biol. Med.,* **2004**, *37*, 1191-1202.

26. Dugan, L. L.; Lovett, E. G.; Quick, K.L.; Lotharius, J.; Lin, T. T.; O'Malley, K. L. Fullerene-based antioxidants and neurodegenerative disorders. *Parkinsonism Relat. Disord*., **2001**, *7*, 243-246.

27. Dugan, L. L.; Turetsky, D. M.; Du, C.; Lobner, D.; Wheeler, M.; Almli, C. R.; Shen, C. K.; Luh, T. Y.; Choi, D. W.; Lin, T. S. Carboxyfullerenes as neuroprotective agents. *Proc. Nat. Acad. Sci.,* **1997**, *94*, 9434-9439.

28. Quick, K. L.; Ali, S. S.; Arch, R.; Xiong, C.; Wozniak, D.; Dugan, L. L. A carboxyfullerene SOD mimetic improves cognition and extends the lifespan of mice. *Neurobiol. Aging,* **2008**, *29*, 117-128.

29. Das, M.; Patil, S.; Bhargava, N.; Kang, J. F.; Riedel, L. M.; Seal, S.; Hickman, J. J. Auto-catalytic ceria nanoparticles offer neuroprotection to adult rat spinal cord neurons. *Biomaterials,* **2007**, *28*, 1918-1925.

30. Hirst, S. M.; Karakoti, A. S.; Tyler, R. D.; Sriranganathan, N.; Seal, S.; Reilly, C. M. Anti-inflammatory properties of cerium oxide nanoparticles. *Small,* **2009**, *5*, 2848-2856.

31. Schubert, D.; Dargusch, R.; Raitano, J.; Chan, S. W. Cerium and yttrium oxide nanoparticles are neuroprotective. *Biochem. Biophys. Res. Commun*., **2006**, *342*, 86-91.

32. Martín, R.; Menchón, C.; Apostolova, N.; Victor, V. M.; Alvaro, M.; Herance, J. R.; García, H. Nano-Jewels in Biology. Gold and platinum on diamond nanoparticles as antioxidant systems against cellular oxidative stress. *ACS Nano,* **2010**, *4*, 6957-6965.

33. McCord, J. M.; Fridovich, I. Superoxide dismutase. An enzymic function for erythrocuprein (Hemocuprein). *J. Biol. Chem.,* **1969**, *244*, 6049-6055.

34. Berlin, J. M.; Leonard, A. D.; Pham, T. T.; Sano, D.; Marcano, D. C.; Yan, S.; Fiorentino, S.; Milas, Z. L.; Kosynkin, D. V.; Price, B. K.; *et al*. Effective drug delivery, *in Vitro* and *in Vivo*, by carbon-based nanovectors noncovalently loaded with unmodified paclitaxel. *ACS Nano,* **2010**, *4*, 4621-4636.

35. Marcano, D. C.; Bitner, B. R.; Berlin, J. M.; Jarjoura, J.; Lee, J. M.; Jacob, A.; Fabian, R. H.; Kent, T. A.; Tour, J. M. Design of poly(ethylene glycol)-functionalized hydrophilic carbon clusters for targeted therapy of cerebrovascular dysfunction in mild traumatic brain injury. *J. Neurotrauma,* in press.

36. Sano, D.; Berlin, J. M.; Pham, T. T.; Marcano, D. C.; Valdecanas, D. R.; Zhou, G.; Milas, L.; Myers, J. N.; Tour, J. M. Noncovalent assembly of targeted carbon nanovectors enables synergistic drug and radiation cancer therapy *in vivo*. *ACS Nano,* **2012**, *6*, 2497-2505.

37. Toda, N.; Ayajiki, K.; Okamura, T. Cerebral blood flow regulation by nitric oxide: recent advances. *Pharmacol. Rev*., **2009**, *61*, 62-97.

38. Montesano, R.; Pepper, M. S.; Möhle-Steinlein, U.; Risau, W.; Wagner, E. F.; Orci, L. Increased proteolytic activity is responsible for the aberrant morphogenetic

behavior of endothelial cells expressing the middle T oncogene. *Cell.* **1990**, *62*, 435-445.

39. Han, D.; Williams, E.; Cadenas, E. Mitochondrial respiratory chain-dependent generation of superoxide anion and its release into the intermembrane space. *Biochem. J.,* **2001**, *353*, 411-416.
40. Aykin-Burns, N.; Ahmad, I. M.; Zhu, Y.; Oberley, L. W.; Spitz, D. R. Increased levels of superoxide and H_2O_2 mediate the differential susceptibility of cancer cells versus normal cells to glucose deprivation. *Biochem. J.,* **2009**, *418*, 29-37.
41. Marklund, N.; Lewander, T.; Clausen, F.; Hillered, L. Effects of the nitrone radical scavengers PBN and S-PBN on *in vivo* trapping of reactive oxygen species after traumatic brain injury in rats. *J. Cereb. Blood Flow Metab.,* **2001**, *21*, 1259-1267.
42. Fabian, R. H.; Perez-Polo, J. R.; Kent, T. A. Perivascular nitric oxide and superoxide in neonatal cerebral hypoxia-ischemia. *Am. J. Physiol. Neart. Circ. Physiol*., **2008**, *295*, H1809-H1814.
43. Navarro, J. C.; Pillai, S.; Cherian, L.; Garcia, R.; Grill, R. J.; Robertson, C. S. Histopathological and behavioral effects of immediate and delayed hemorrhagic shock after mild traumatic brain injury in rats. *J. Neurotrauma,* **2012**, *29*, 322-334.
44. Hicks, R. R.; Smith, D. H.; Lowenstein, D. H.; Saint Marie, R.; McIntosh, T. K. Mild experimental brain injury in the rat induces cognitive deficits associated with regional neuronal loss in the hippocampus. *J. Neurotrauma,* **1993**, *10*, 405-414.

3.7. Experimental Contributions

I prepared, purified, and characterized the PEG-HCCs. Also, I worked with James Culver on the internalization of the nanoparticles experiments. Dr. Bitner and Leela Cherian performed *in vitro* and animals experiments.

Chapter 4

Antibody-Targeted Nanovectors for the Treatment of Brain Cancers

This chapter was entirely copied from the reference #1 of this section

4.1. Introduction

Glioblastoma multiforme (GBM) is the most common and aggressive malignant primary brain tumor in humans. GBM prognosis is poor, with a 14 month median survival time despite interventions.[2] Nanovectors, nanoparticles capable of transporting and delivering drugs and bioactive molecules, are an emerging class of drug delivery platforms.[3] Some nanovectors, such as hydrophilic carbon clusters (HCCs)[4-6] and single-walled carbon nanotubes,[7] can be engineered to possess both hydrophobic and hydrophilic domains, combining high aqueous solubility with the ability to adsorb

hydrophobic compounds. Therefore nanovectors are an exciting avenue for drug delivery of such compounds without the need for covalent drug or covalent antibody attachment[7,8] and could be used to target glioma.[8-12]

HCCs are heavily oxidized carbon nanoparticles that are 30 to 40 nm long and approximately 1 nm wide, and although water soluble, they must be further functionalized with poly(ethylene glycol) (PEG-5000 MW) to maintain their solubility in phosphate buffered saline (PBS), thereby rendering the PEG-HCCs nanovector system. Their synthesis and characterization has been described previously.[4,5] PEG-HCCs have three properties that allow them to be used as nanovectors: extremely low biological toxicity with clearance mainly through the kidneys,[4] hydrophobic domains of the PEG-HCCs that can be non-covalently loaded with drugs,[4,6] and an ability to strongly bind to IgG-type antibodies while the antibodies maintain the majority of their activity.[5,6] Thus, drug-loaded PEG-HCCs combined with an IgG will bind to a chosen cell surface antigen and deliver a hydrophobic, lipophilic drug into cells that express the selected epitope. We use the nomenclature: $Epitope_{AB}$/Drug/PEG-HCCs to describe a particular hydrophilic carbon cluster antibody enhancement system (HADES) composed of an antibody, a drug, and the PEG-HCCs delivery platform. In this nomenclature, non-covalent sequestration is indicated with a slash, "/", and covalent bonding with a dash, "-". In each case, the drug and the antibody are added, sequentially, to the PEG-HCCs by simple mixing, hence a facile "mix-and-treat" toolbox is afforded.[5]

We have sequestered three potent hydrophobic chemotherapeutic agents onto the PEG-HCCs, chosen on the basis of theoretical synergistic effect. These include (a) SN-

38, a topoisomerase I inhibitor, which arrests the cell cycle in the S and G2 phases,[13] (b) Vinblastine (Vin), which causes microtubule detachment from spindle poles, arresting the cell cycle in the M phase at the mitotic spindle checkpoint,[14] and (c) Docetaxel (Doc), which binds tubulin, preventing microtubule depolymerization and arresting the cell cycle in both the G2 and M phases, resulting in mitotic catastrophe.[15] Of note, SN-38 is dramatically more potent than the pro-drug form, Irinotecan®, but SN-38 cannot be directly administered to patients due to its extremely low aqueous solubility.[16] The use of the HADES system allows for the direct delivery of this active drug, and perhaps other pharmaceutics, whose solubility requires the use of moieties that increase solubility, but limits drug efficacy.

To treat GBM, we selected immunoglobulin G antibodies (IgGs) to cell surface epitopes that are overexpressed in glioma cells relative to other cell types. $GFAP_{AB}$ is an IgG-type antibody to the glial fibrillary acidic protein (GFAP), a protein present in reactive astrocytes and also highly expressed in the majority of GBM cells.[17] The interleukin-13 receptor (Il-13R) is a cytokine receptor, binding interleukin-13, and has been found to be upregulated in a large range of cancers, including GBM.[18] Normal, unreactive, astrocytes express low levels of GFAP[19,20] and even lower levels of IL-13R.[21] The epidermal growth factor receptor (EGFR) is the cell-surface receptor for members of the EGF family of extracellular proteins. This receptor is overexpressed, in either full length or truncated form, in many cancers including GBMs.[22] Surface epitope mapping was performed on primary glioma cell cultures and the binding of specific IgGs to GFAP:IL-13R:EGFR had ratios of 1.0:1.3:1.6, respectively (Appendix D, Figure D1A-C).

We examined the effectiveness of the antibody-targeted, IgG/drug/PEG-HCCs in primary human glioma cultures and control cultures of normal human astrocytes (NHA) and human cortical neurons (HCN). As GBM generates blood–brain barrier defects, this antibody-guided drug delivery system might ultimately be used intravenously to actively target glioma cells.[23]

4.2. Experimental Procedures

4.2.1. HCCs Functionalization, Drug Loading and Antibody Binding

The HCCs, PEG-HCCs and Drug/PEG-HCCs were prepared as reported by Berlin *et al*.[5] Drugs were dissolved in a minimal amount of methanol (for Vin and Doc) or THF (for SN-38) and added dropwise into a stirring aqueous solution of PEG-HCCs. After overnight sonication, the organic solvent was removed by rotary evaporating one-third of the original volume of solution, adding one-third volume of water, and carrying out the same protocol evaporation/addition of water two more times according to published protocols.[4] Vin (LogP 4.8) was incorporated into PEG-HCCs with a mass ratio of 5:1; Doc (LogP 2.92) was incorporated into PEG-HCCs with a mass ratio of 1.7:1 and SN-38 (LogP 1.87) was incorporated into PEG-HCCs with a mass ratio of 0.33:1. Three mouse monoclonal antibodies, IgGs with affinities to cancer cell surface epitopes GFAP (2A5), Il-13R (YY-23Z) and EGFR (528), were obtained from Santa Cruz Biotechnology (Santa Cruz, CA, USA). Prior to use, drug-loaded PEG-HCCs were vortexed for 15 min and then were co-incubated with IgG for 15 min before being diluted and added to cell media.

We used a mass ratio of PEG-HCCs:IgG of 4.1:1 throughout. Although heterogeneous, the average molecular mass of PEG-HCCs is ~920,000, which gives rise to a molar PEG-HCCs:IgG ratio of 1:1.5. Assuming the binding distribution to be Poissonian, ~80% PEG-HCCs have one or more IgGs bound. Visualization of mouse IgG was performed by incubating Alexa Fluor 594 goat anti-mouse IgG (Molecular Probes), overnight. The levels of Alexa Fluor-IgG were calibrated using a 5 μm thick, gelatin tissue phantom, entrapping 150 μg mL^{-1}/1 μM goat-IgG[21].

4.2.2. Cell Cultures

Primary human glioblastoma or astrocytoma cells were prepared from tumors within 10 min of their excision. The tumors were broken up using a pipette and then grown in DMEM, 20% FBS, GlutaMax-I, sodium pyruvate and Pen/Strep, for 2 weeks. After this time, and in all presented data, the same media was used, except that sodium pyruvate was omitted. NHA were obtained from Lonza (Walkersville, MD, USA) and HCN from the American Type Culture Collection (ATCC Manassas, VA USA), and grown subject to their recommendations. NHA were grown in Astrocyte Cell Basal Medium supplemented with 3% FBS, Glutamine, Insulin, fhEGF, GA-1000 and Ascorbic acid. HCN using ATCC-formulated Dulbecco's Modified Eagle's Medium (Cat#30-2002) and supplemented with 10% FBS. GBM and NHA were grown to confluency in the appropriate media on Costar 96-well growth plates (Corning, NYC, NY, USA) and HCN were grown on 16-well Lab-Tek slide chambers (Nalge Nunc, Rochester, NY, USA). Cells were grown for 24 h in the presence/absence of all effectors, in a total volume of 250 μL.

4.2.3. Assays

The ability of PEG-HCCs to take up hydrophobic solutes compromises a large number of high throughput proliferation assays. We find that many common reporter chromophore/fluorophores partition into PEG-HCCs and then undergo altered absorbance/fluorescence properties.[4,5] PEG-HCCs also interfere with peptide-bond chelated copper reduction of Folin-Ciocalteu reagent (phosphomolybdate/ phosphotungstate), making the Lowery protein assay unsuitable.

4.2.4. Protein Measurement

Cell proliferation studies with PEG-HCCs included four HCN controls: 100 μM CCCP (100% cell death), saline vehicle, PEG-HCCs and IgG/PEG-HCCs using monoclonal antibodies toward GFAP, IL-13R or EGFR; three HADES treatments where PEG-HCCs loaded with the drugs Vin, Doc, or SN-38 were added to HCN with or without antibodies; and a final triple pairing with or without antibodies. After 24 h the cells were washed with PBS, solubilized using 0.1% SDS and then the protein present in the well was measured using the Thermo Scientifics Micro Bicinchoninic acid (BCA) Assay Kit (Waltham, MA, USA) and the data displayed in Figure D2 (Appendix D).

4.2.5. Cell Viability Measurements

The measurements and quantification of DNA 3'OH and blunt ended breaks by use of the *dd*TUNEL and blunt ended ligation were performed as described in our recent publications.[25,35] The biotinylated *dd*UTP and biotinylated blunt ended oligonucleotide probe was visualized using Texas Red labeled avidin. Cells were incubated with 500 nM

Mitotracker Red (Cat#M22425), 1 μM Hoechst 33258 (Cat#H1398) and 100 nM Dead Green (Cat#I10291), with reagents obtained from Molecular Probes (Eugene, OR, USA). The activity of Caspase-3 in fixed, 0.1% Triton permeabilized cells was measured using the Molecular Probes R110-EnzChek Assay Kit (Cat#E13184), incubating cells for 1 h at 37 °C. Signals from Dead Green/R110 and from Mitotracker were calibrated against known concentrations of liquid FITC-gelatin and Texas Red-gelatin and then against FITC/Texas Red gelatin tissue phantoms 5 μm in thickness.[25,29]

4.2.6. Viability Cut-Off

Cells were counted at 4× magnification using a Nikon Eclipse TE2000-E fluorescent microscope equipped with a CoolSnap ES digital camera system (Roper Scientific) containing an CCD-1300-Y/HS 1392 × 1040 imaging array cooled by a Peltier device. Images were recorded using Nikon NIS-Elements software as JEP2000 files. Cells were deemed to be non-viable if they had Dead Green/Hoechst signals >5 times the level found in control cells and >4.2 times the level of *dd*TUNEL labeled DNA 3'OH ends in control cells.

4.3. Results and Discussion

In Figure 4.1A we demonstrate the ability of the HADES formulation $GFAP_{AB}$/SN-38/PEG-HCCs, with each component concentration at 3.9 nM, 2 μM, and 2.6 nM, respectively, to induce cell death in primary GBM cell cultures. Due to the fact that nanomaterials can often interfere with biological assays,[24] three different

methodologies were used to measure cell viability. Total, viable, and dead gliomal cell numbers in confluent primary GBM cell cultures were measured using *dd*TUNEL (a quantitative assay for 3'OH DNA ends),[25] Dead Green,[26] and Hoechst stains.[25] Cells were treated with $GFAP_{AB}$/SN-38/PEG-HCCs or saline for 24 h. SN-38 induced cell death could be monitored by all three viability methodologies, but there was slight under reporting of total cell numbers using both *dd*TUNEL and Dead Green, with respect to Hoechst, due to the presence of overlapping cells.[27] It is clear that the three methodologies are robust even in the presence of nM concentrations of PEG-HCCs. Figure 4.1A further shows that in the saline control viable cell numbers increased from the ≈30,000 inoculum to 52,000 cells mL^{-1} in 24 h, whereas incubation with $GFAP_{AB}$/SN-38/PEG-HCCs, there was a fall in cell numbers to only 22,000 cells mL^{-1}. Moreover, there was a three-fold increase in the number of dead cells following treatment with HADES.

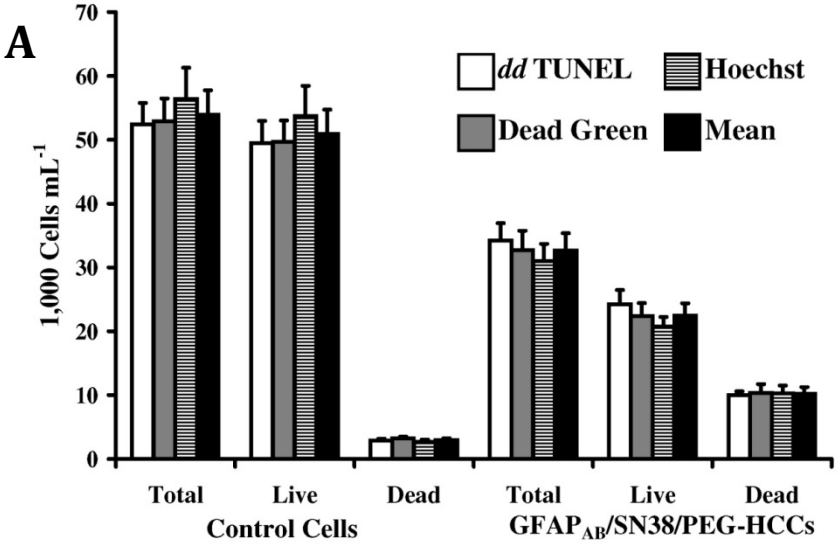
A
70
60
50
40
30
20
10
0
1,000 Cells mL-1
dd TUNEL
Hoechst
Dead Green
Mean
Total
Live
Dead
Total
Live
Dead
Control Cells
GFAPAB/SN38/PEG-HCCs

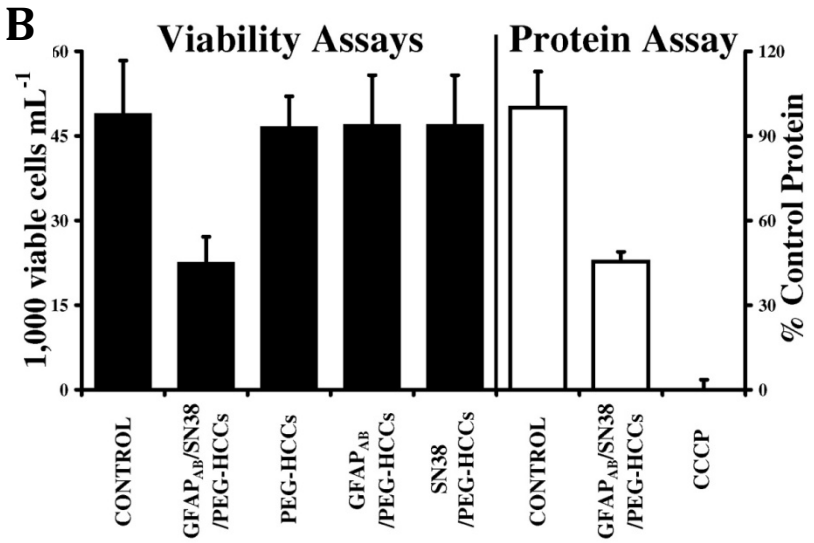
B
Viability Assays
Protein Assay
60
45
30
15
0
1,000 viable cells mL-1
120
90
60
30
0
% Control Protein
CONTROL
GFAPAB/SN38 /PEG-HCCs
PEG-HCCs
GFAPAB /PEG-HCCs
SN38 /PEG-HCCs
CONTROL
GFAPAB/SN38 /PEG-HCCs
CCCP

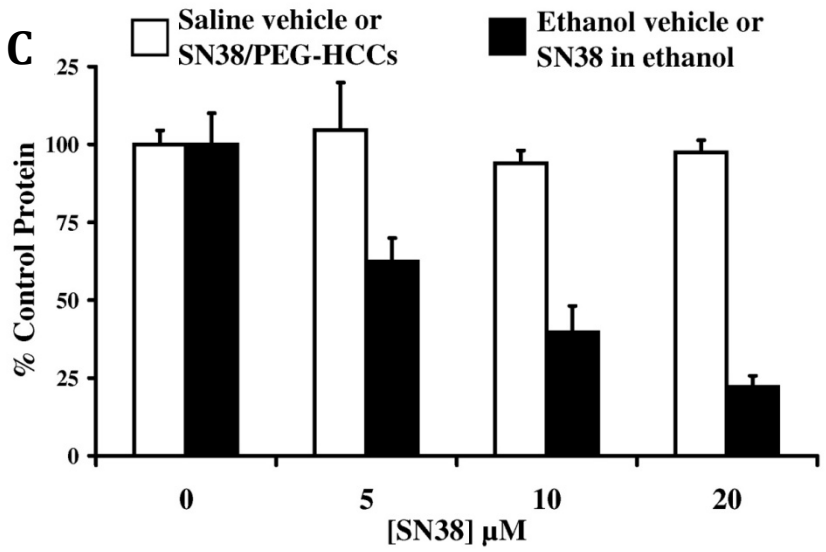

Figure 4.1. Four measures of viability all show that HADES therapy kills GBM primary cultures. (A) The three cell viability measures; *dd*TUNEL (white bars), Dead Green (gray bars) and Hoechst staining (striped bars) all give similar live/dead numbers (averages are the black bars) in GBM cultures in the absence (controls, left) and presence (HADES, right) as $GFAP_{AB}$/SN-38/PEG-HCCs with each component at the following concentrations: 3.9 nM, 2.6 nM, and 2 µM, respectively. Viable cell numbers fall to only 44% of the control in HADES treated cells and the dead cell fraction rises from 5.5% to 31%. (B) The average levels of living GBM cells (left), from *dd*TUNEL, Dead Green and Hoechst staining, show that the individual HADES components, PEG-HCCs, $GFAP_{AB}$/PEG-HCCs, and SN-38/PEG-HCCs are non-toxic, whereas HADES treatment, in the form of $GFAP_{AB}$/SN-38/PEG-HCCs, causes significant cell death. Additionally, changes in cell protein mass, using the BCA method (right panel), correlate with viable

cell numbers determined using viability stains in fixed cells, using the lethal uncoupling agent CCCP to establish the minimum cellular protein levels. (C) Comparison of SN-38 toxicity when presented to GBM in solution or as HADES. SN-38 is insoluble in water, so it had to be delivered in ethanol and was compared to an ethanol control. Thus, changes in protein mass after 24 h treatment with SN-38/PEG-HCCs (white bars) and SN-38 (black bars) were compared to saline or ethanol only controls, respectively. SN-38/PEG-HCCs are not toxic up to 20 μM SN-38, whereas aqueous SN-38 has an LD_{50} of ~ 8 μM. In all figures $n = 8$ wells and the error bars are equal to the SD.

Figure 4.1B (left panel) shows that the individual components of HADES treatment, PEG-HCCs (2.6 nM), $GFAP_{AB}$ (3.9 nM) and SN-38 (2 μM), are not toxic towards cell when added individually. Only when the three components: targeting antibody, chemotherapeutic and nanovector are all combined is there an increase in cell death. Addition of the three individual HADES components to glioblastoma cells results in no statistically significant difference in cell viability. Remarkably, we find that PEG-HCCs alone are not toxic towards glioma, astrocytes or neurons at concentrations more than three orders of magnitude greater than those used in all the experiments related to Figure 4.1 (Appendix D, Figure D3). This corresponds with previous reports showing that PEG-HCCs are not toxic to mammalian cell cultures or in mice.[4-6]

Cell counting assays are time consuming; in order to validate a high data throughput assay, we compared the changes in cell numbers obtained from viability studies with the use of the bicinchoninic acid (BCA) assay of protein levels (Figure

4.1B). The maximum and minimum cellular protein levels were establish using a saline negative control (100%) and carbonyl cyanide chlorophenyl hydrazone (CCCP) positive control (0%). Incubation of GBM for 24 h with CCCP (100 μM) induces cell death by mitochondrial uncoupling and allows the background matrix protein levels to be determined. Cellular protein levels following HADES treatment fell to 46% of the saline control level, mirroring the 44% levels of living cells determined using viability methodologies.

The impact of sequestering SN-38 on the hydrophobic core of the PEG-HCCs was evaluated by comparing the changes in cellular protein of GBM following 24 h incubation with SN-38/PEG-HCCs or SN-38 alone (Figure 4.1C). As mentioned previously, SN-38 is extremely insoluble in water;[16] for this reason, in experiments using bulk phase drug we added either 5 μL of ethanol or ethanol containing SN-38 to each 250 μL well volume. The two controls, ethanol and saline, had no significant change in cellular protein relative to one another. We found that aqueous SN-38 has an LD_{50} of approximately 8 μM toward primary GBM, within the 5-10 μM range reported by others using immortalized human glioblastoma cell cultures.[28] Interestingly, no toxicity is observed when SN-38 is presented to the cells in the form of SN-38/PEG-HCCs, even at concentrations as high as 20 μM. This indicates that the SN-38/PEG-HCCs, without antibody targeting, cannot deliver the drug to the GBM cells at any significant rate.

In Figure 4.2 we show that HADES treatment is toxic towards a variety of human glial cell carcinomas and that the system is flexible with respect to the loaded chemotherapeutic. In Figure 4.2A we show the titration of three different primary GBM

cultures, and one primary anaplastic astrocytoma (solid line), with $GFAP_{AB}$/SN-38/PEG-HCCs. The three GBM cultures, which have a doubling time of 28 to 34 h, have a common dose response with a LD_{50} of 1.5 to 2 μM SN-38, delivered in the form of HADES. In the slower growing anaplastic astrocytoma, which has a doubling time of 48 to 52 h, the LD_{50} is elevated to ~3.75 μM SN-38. In Figure 4.2B we show the dose response of GBM towards three different chemotherapeutics, SN-38, Vin, and Doc which were loaded into PEG-HCCs and guided to the cell membrane using $EGFR_{AB}$. The highest concentration of $GFAP_{AB}$ used on the confluent cells was 10 nM. In control experiments, we incubated for 1 h with $GFAP_{AB}$/SN-38/PEG-HCCs, with each component concentration at 10 nM, 5 μM, and 6.5 nM, respectively. Then, fixed cells were stained using a labeled goat anti-mouse secondary antibody. Results indicated 86% saturation of the total surface GFAP epitopes, indicating that only 14% of the surface epitope is not bound to $GFAP_{AB}$/SN-38/PEG-HCCs (Appendix D, Figure D1D). Using this nanovector delivery system, the LD_{50} for both SN-38 and Vin is ~1.5 μM while for Doc it is ~3 μM.

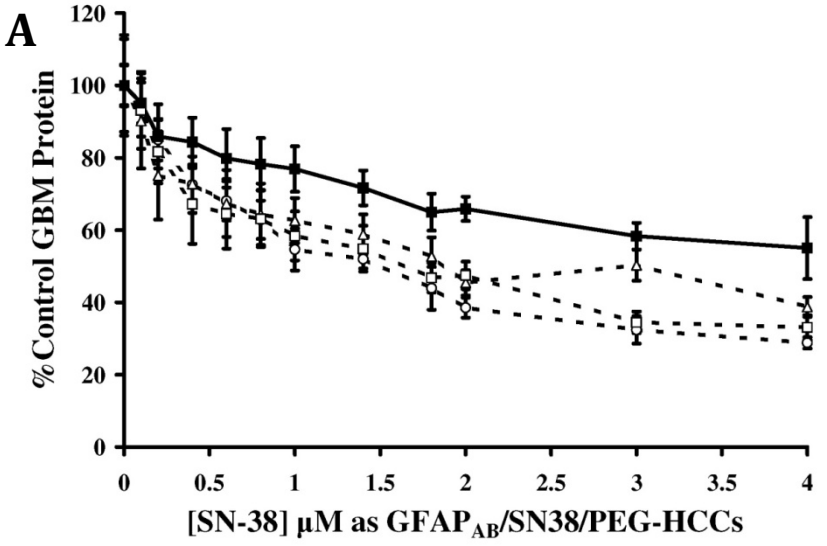
A
% Control GBM Protein
120
100
80
60
40
20
0
0
0.5
1
1.5
2
2.5
3
3.5
4
[SN-38] µM as GFAP$_{AB}$/SN38/PEG-HCCs

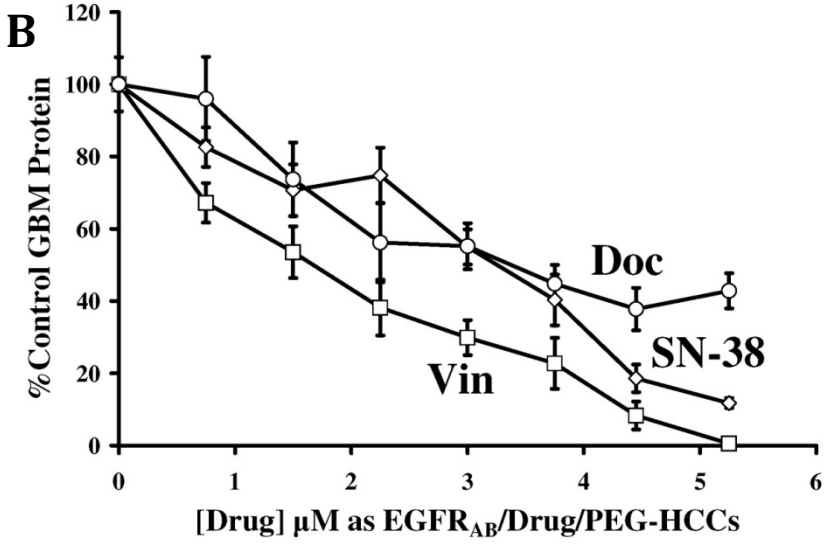
B
% Control GBM Protein
120
100
80
60
40
20
0
0
1
2
3
4
5
6
Doc
SN-38
Vin
[Drug] µM as EGFR$_{AB}$/Drug/PEG-HCCs

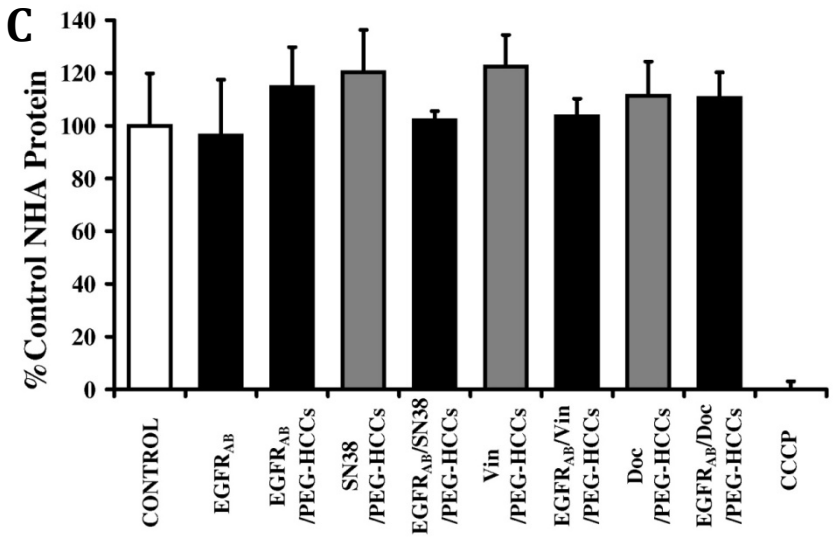

Figure 4.2. HADES therapy is highly versatile, having broad antibody/drug specificity and it is lethal toward a range of GBM. (A) The dose response curve of three different GBMs (dashed lines) and one anaplastic astrocytoma (solid line) toward anti-$GFAP_{AB}$/SN-38/PEG-HCCs, measured at 24 h. (B) HADES treatment using three hydrophobic drugs: Vin (□), Doc (○) and SN-38 (◊) were presented to GBM for 24 h within PEG-HCCs, targeted to the tumor antigen, EGFR, by an IgG. (C) Astrocytes are insensitive to HADES and the individual HADES components, as shown by protein measurement following 24 h incubation. Control (white bar on left), incubation of NHA with $EGFR_{AB}$ and $EGFR_{AB}$/PEG-HCCs (next two black bars) and then with $EGFR_{AB}$ in the absence (gray bars) and presence (black bars) of PEG-HCCs ± drug (5μM) causes no change in protein mass.

In Figure 4.2C we show the effects of 5μM Drug/PEG-HCCs ± $EGFR_{AB}$ treatment on normal human astrocyte total protein levels, a treatment that caused >85% cell death in glioma. Neither PEG-HCCs nor $EGFR_{AB}$/PEG-HCCs cause cell death. Extraordinarily, astrocytic mass was unaffected by the three $EGFR_{AB}$/drug/PEG-HCCs combinations, each of which was overwhelmingly lethal to GBMs.

Clinically, the use of combined therapy in cancer treatment is an attempt to evade the heterogeneous response that a cancer cell population has toward different chemotherapeutics and the ability of cancer cells to rapidly acquire drug resistance. As SN-38, Vin, and Doc all have different pharmacologic targets, we postulated that the three drugs might be able to potentiate each other's anti-cancer properties. We incubated GBM, and also control NHA and HCN, with low levels of the three drugs in HADES form: consisting of three individual HADES formulations and an additional triple combination therapy where the three HADES individuals were combined (Figure 4.3). The low drug levels chosen, 0.5 μM, allowed enough damaged and dying cells to remain at the end of a 24 h incubation to be characterized using specific probes of DNA damage, mitochondria dysfunction, loss of plasma membrane potential and of the initiation of apoptotic, proteolytic, cascades.

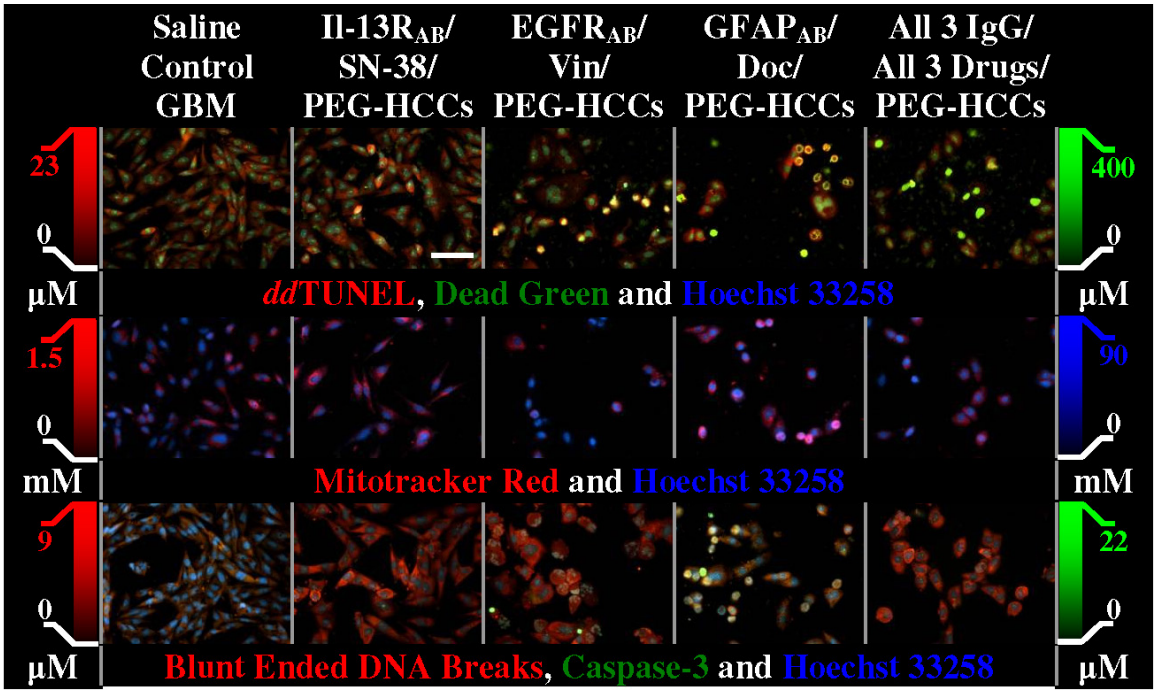

Figure 4.3. Effects of Vin, Doc and SN-38 HADES individual or triple therapy on GBM measured using six different death markers; all drugs at a final concentration of 0.5 µM. The upper row shows 3'OH DNA ends, Dead Green and Hoechst DNA staining, the middle row shows mitochondrial membrane potential and the bottom row shows blunt ended, lethal, DNA breaks[25,29] and Caspase-3 activity. All of the figures are at 20× magnification and the side bars show the calibration scale for each fluorophore.[25,29]

The upper panel of Figure 4.3 shows the effects of the individual drugs and triple therapy on the viability of glioma primary cultured GBM cells, demonstrated by *dd*TUNEL (red)[25] and Dead Green and Hoechst (blue). It is evident that both Vin and Doc have devastating impacts on GBM. Microscopic examination shows evidence of mitotic catastrophe and of the presence of gear-wheel-shaped nuclei, typical of the

microtubule disrupting actions of Vin[30] and Doc.[15,31] The center panel of Figure 4.3 shows the loss of mitochondrial membrane potential with all four HADES regimes. Vin has been shown to alter the distribution of mitochondria throughout cells and to cause mitochondrial 'clumping'[32] and this type of mitochondrial flocculation is clearly evident in GBM. We also observe changes in mitochondrial morphology and cytosolic distribution in GBM treated with $EGFR_{AB}$/Doc/PEG-HCCs that are very similar to those observed in prostate cancer cells treated with Taxels.[31]

The lowest panels of Figure 4.3 show the levels of blunt ended DNA breaks[25,29] and Caspase-3 activity. All three individual HADES therapies cause increases in these lethal DNA breaks and in apoptotic, Caspase-3 activity.[31] $EGFR_{AB}$/Doc/PEG-HCCs in particular increases Caspase-3 activation, especially in the condensed cells, in which gear-wheel shaped nucleus predominate. In Figure D4A-C (Appendix D), we show the death labeling of two more primary GBMs and that of an anaplastic astrocytomoa, under conditions identical to that of Figure 4.3. In addition in Figure D4D-E (Appendix D), we show the effects of the same therapies on cultures of NHA and HCN. In stark contrast to the effects of HADES on the GBM, the effects on astrocytes and neurons are far more modest. Compared to control, for the four treatment groups, there is a doubling in the levels of *dd*TUNEL positive DNA 3'OH ends in NHA but no great increase in cell death. In Figure D4E (Appendix D), it is noteworthy that we observe no changes in nuclear structure of the treated neurons, even though neurons are very vulnerable towards microtubule disruption drugs like Doc[31] and Vin (Figure D4F, Appendix D).[34]

Figure 4.4 shows the extent of cell viability and death, for GBM, NHA and HCN, using Hoechst staining. Figure 4.4A shows the levels of live and dead GBM cells following individual HADES treatments and the triple therapy. The two microtubule targeting chemotherapeutics are much more effective than the Topoisomerase-I inhibitor, SN-38. Treatment with Il-13R_{AB}/SN-38/PEG-HCCs, $GFAP_{AB}$/Vin/PEG-HCCs or $EGFR_{AB}$/Doc/PEG-HCCs all produced a statistically significant, $p < 0.01$, drop in living cell numbers and an increase in dead cell percentages. There is a statistically significant, $p < 0.01$, synergistic effect caused by triple therapy, with respect to the individuals, on the level of cell death.

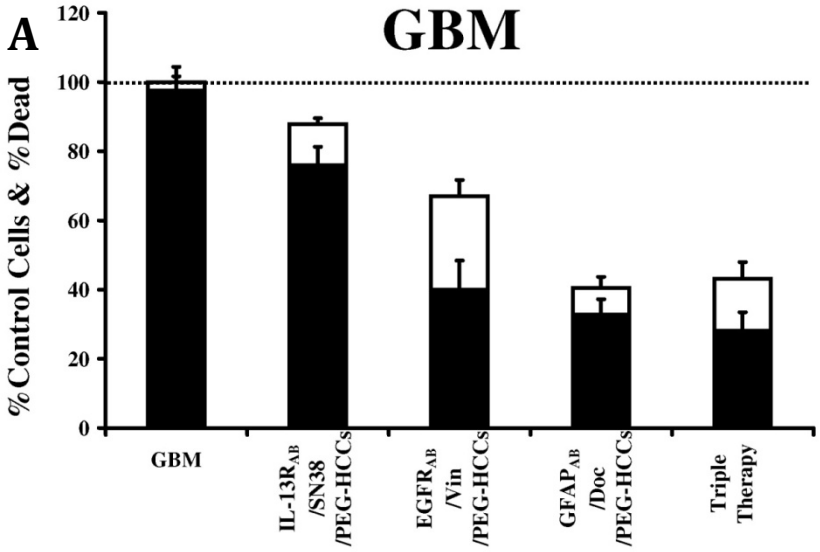
A
GBM
% Control Cells & % Dead
120
100
80
60
40
20
0
GBM
IL-13R$_{AB}$ /SN38 /PEG-HCCs
EGFR$_{AB}$ /Vin /PEG-HCCs
GFAP$_{AB}$ /Doc /PEG-HCCs
Triple Therapy

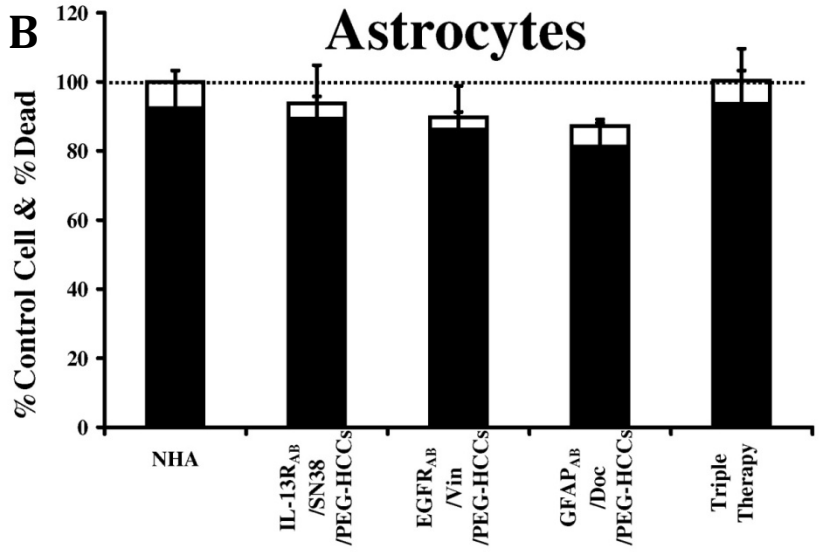
B
Astrocytes
% Control Cell & % Dead
120
100
80
60
40
20
0
NHA
IL-13R$_{AB}$ /SN38 /PEG-HCCs
EGFR$_{AB}$ /Vin /PEG-HCCs
GFAP$_{AB}$ /Doc /PEG-HCCs
Triple Therapy

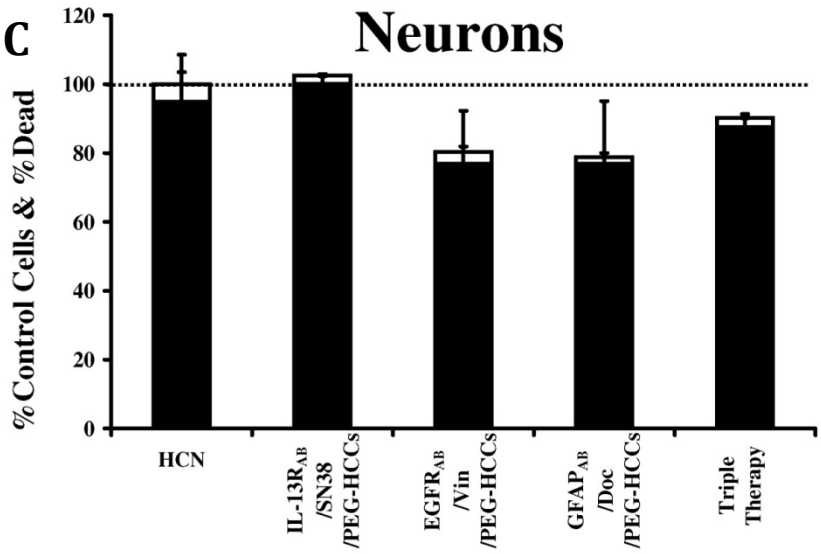

Figure 4.4. HADES triple therapy is not overly toxic towards astrocytes and neurons, but is highly toxic toward GBM. The living and dead cell numbers resulting from HADES treatment using 0.5 μM drug (Vin, Doc and SN-38) targeted with monoclonal antibodies to GBM surface antigens (Il-13R, EGFR and GFAP), (A) as IgG/drug/PEG-HCCs in cultures of GBM, (B) astrocytes and (C) neurons. Black bars are % control living cells, white bars are % dead cells. (GBM: n = 8 wells; NHA: n = 8 wells; HCN: n = 4 wells; error bars SD in all cases).

With respect to NHA and HCN, HADES treatment did not result in statistically significant changes in cell viability. However, in the case of HCN, only four wells were used for each treatment. Therefore, the number is too low to make accurate statistical

assertions. We therefore measured the changes in HCN protein levels in controls and following HADES treatment [as we had done with NHA (Figure 4.2C)], and we present this data in Figure D4 (Appendix D). The BCA assay shows that individual HADES therapies do not kill neurons, to any statistically significant degree, when using protein as a measure of cellular mass. However, combining the three drug-loaded PEG-HCCs, in the absence or presence of antibodies, does cause a statistically significant, $p<0.05$, 5% drop in cell protein levels. In spite of this increase in the killing of neurons, use of a multipronged therapy often has utility in treatment due to its potential ability to avoid the development of drug resistance.

4.4 Conclusions

In summary, we are able to target drug-loaded PEG-HCCs to the surface epitopes of cells, using specific antibodies. EGFR,[35] IL-13R[36] and GFAP[37] are not present in human cortical neurons, but are found in high levels in GBM.[35-37] Single or triple therapy is capable of killing gliomas with extreme lethality, while at the same time causing little or no ill-effects towards either astrocytes or neurons. The simplicity of the preparation where the PEG-HCCs, drug, and antibody are simply mixed together, coupled with the lethality of these combinations toward extremely aggressive cancers, provides encouragement for the continued testing of HADES.

4.5. Acknowledgments

The work at the Methodist Hospital Research Institute was funded by The Henry J. N. Taub Fund for Neurological Research, The Pauline Sterne Wolff Memorial Foundation, Golfers Against Cancer and the Methodist Hospital Foundation. S. Lopez provided valuable technical support throughout the study; D. Livingston and D. James provided proof reading and comments. The support at Rice University was provided by the Mission Connect Mild Traumatic Brain Injury Consortium funded by the Department of Defense (W81XWH-08-2-0143); the Alliance for NanoHealth through a subcontract from the University of Texas Health Science Center, Houston with funding from the Department of Defense (W8XWH-07-2-0101) and the Nanoscale Science and Engineering Initiative of the National Science Foundation under Award EEC-0647452 through the NSF Center for Biological and Environmental Nanotechnology.

4.6. References

1. Sharpe, M. A.; Marcano, D. C.; Berlin, J. M.; Widmayer, M. A.; Baskin, D. S.; Tour, J. M. Antibody-targeted nanovectors for the treatment of brain cancers. *ACS Nano*, **2012**, *6*, 3114-3120.
2. Preusser, M.; de Ribaupierre, S.; Wöhrer, A.; Erridge, S. C.; Hegi, M.; Weller, M.; Stupp, R. Current concepts and management of glioblastoma. *Ann. Neurology,* **2011**, *70*, 9-21.
3. Chakraborty, M.; Jain, S.; Rani, V. Nanotechnology: emerging tool for diagnostics and therapeutics. *Appl. Biochem. Biotechn.,* **2011**, *165*, 1178-1187.

4. Berlin, J. M.; Leonard, A. D.; Pham, T. T.; Sano, D.; Marcano, D. C.; Yan, S.; Fiorentino, S.; Milas, Z. L.; Kosynkin, D. V.; Price, B. K. *et al*. Effective drug delivery, *in vitro* and *in vivo*, by carbon-based nanovectors noncovalently loaded with unmodified paclitaxel. *ACS Nano,* **2010**, *4*, 4621- 4636.

5. Berlin, J. M.; Pham, T. T.; Sano, D. S.; Mohamedali, K. A.; Marcano, D. C.; Myers, J. N.; Tour, J. M. Noncovalent functionalization of carbon nanovectors with an antibody enables targeted drug delivery. *ACS Nano,* **2011**, *8*, 6643-6650.

6. Sano, D.; Berlin, J. M.; Pham, T. T.; Marcano, D. C.; Valdecanas, D. R.; Zhou, G.; Milas, L.; Myers, J. N. Tour, J. M. Non-covalent assembly of targeted carbon nanovectors enables synergistic drug and radiation cancer therapy *in vivo*. *ACS Nano*, **2012**, *6*, 2497-2505.

7. Liu, Z.; Fan, A. C.; Rakhra, K.; Sherlock, S.; Goodwin, A.; Chen, X.; Yang, Q.; Felsher, D. W.; Dai, H. Supramolecular stacking of doxorubicin on carbon nanotubes for *in vivo* cancer therapy. *Angew. Chem. Int. Ed. Engl.,* **2009**, *48*, 7668-7672.

8. Hong, G.; Tabakman, S. M.; Welsher, K.; Chen, Z.; Robinson, J. T.; Wang, H.; Zhang, B.; Dai, H. Near-infrared-fluorescence-enhanced molecular imaging of live cells on gold substrates. *Angew. Chem.,* **2011**, *123*, 4740-4744.

9. O'Driscoll, C. M.; Griffin, B. T. Biopharmaceutical challenges associated with drugs with low aqueous solubility: the potential impact of lipid-based formulations. *Adv. Drug Del. Rev.,* **2008**, *60*, 617-624.

10. Ohba, S.; Hirose, Y.; Yoshida, K.; Yazaki, T.; Kawase, T. Inhibition of 90-KD heat shock protein potentiates the cytotoxicity of chemotherapeutic agents in human glioma cells. *J. Neurosurg.,* **2010**, *112*, 33-42.

11. Biggs, T.; Foreman, J.; Sundstrom, L.; Regenass, U.; Lehembre, F. Antitumor compound testing in glioblastoma organotypic brain cultures. *J. Biomolec. Screening,* **2011**, *16*, 805-817.

12. Wang, W.; Ghandi, A.; Liebes, L.; Louie, S. G.;, Hofman, F. M.;, Schönthal, A. H.; Chen, T. C. Effective conversion of irinotecan to SN-38 after intratumoral drug delivery to an intracranial murine glioma model *in vivo*. Laboratory investigation. *J. Neurosurg.,* **2011**, *114*, 689-694.

13. Maurya, D., Ayuzawa, R., Doi, C., Troyer, D. & Tamura, M. Topoisomerase I inhibitor SN-38 effectively attenuates growth of human non-small cell lung cancer cell lines *in vitro* and *in vivo*. *J. Environ. Pathol. Toxicol. Oncol.,* **2011**, *30*, 1-10.

14. Hoshino, T.; Wilson, C. B.; Muraoka, I. The Stathmokinetic (mitostatic) effect of vincristine and vinblastine on human gliomas. *Acta Neuropathologica,* **1979**, *47*, 21-25.

15. Fabbri, F.; Amadori, D.; Carloni, S.; Brigliadori, G.; Tesei, A.; Ulivi, P.; Rosetti, M.; Vannini, I.; Arienti, C.; Zoli, W. Mitotic catastrophe and apoptosis induced by docetaxel in hormone-refractory prostate cancer cells. *J. Cell. Physiology,* **2008**, *217*, 494-501.

16. Zhang, J.A.; Xuan, T.; Parmar, M.; Ma, L.; Ugwu, S.; Ali, S.; Ahmad, I. Development and characterization of a novel liposome-based formulation of SN-38. *Internat. J. Pharmaceutics*, **2004**, *270*, 93–107.

17. Chekhonin, V.; Baklaushev, V.; Yusubalieva, G.; Gurina, O. Targeted transport of ^{125}I-labeled antibody to GFAP and AMVB1 in an experimental rat model of C6 glioma. *J. Neuroimmune Pharm.,* **2009**, *4*, 28-34.

18. Husain, S. R.; Joshi, B. H.; Puri, R. K. Interleukin-13 receptor as a unique target for anti-glioblastoma therapy. *Int. J. Cancer,* **2011**, *92*, 168-175.

19. Eng, L. F.; Ghirnikar, R. S. GFAP and astrogliosis. *Brain Pathology,* **1994**, *4*, 229-237.

20. Schittenhelm, J.; Mittelbronn, M.; Nguyen, T.-D.; Meyermann, R.; Beschorner, R. WT1 expression distinguishes astrocytic tumor cells from normal and reactive astrocytes. *Brain Pathology,* **2008**, *18*, 344-353.

21. Wu, H.; Mahmood, A.; Lu, D.; Jiang, H.; Xiong, Y.; Zhou, D.; Chopp, M. Attenuation of astrogliosis and modulation of endothelial growth factor receptor in lipid rafts by simvastatin after traumatic brain injury. *J. Neurosurg.,* **2010**, *113*, 591-597.

22. Hatanpaa, K. J.; Burma, S.; Zhao, D.; Habib, A. A. Epidermal growth factor receptor in glioma: signal transduction, neuropathology, imaging, and radioresistance. *Neoplasia,* **2010**, *12*, 675-684.

23. Chekhonin, V. P.; Baklaushev, V. P.; Yusubalieva, G. M.; Belorusova, A. E.; Gulyaev, M. V.; Tsitrin, E. B.; Grinenko, N. F.; Gurina, O. I.; Pirogov, Y. A. Targeted delivery of liposomal nanocontainers to the peritumoral zone of glioma by means of monoclonal antibodies against GFAP and the extracellular loop of Cx43. *Nanomedicine: Nanotech. Biol. Med.,* **2011**, Epub ahead of print, http://www.ncbi.nlm.nih.gov/pubmed/21703991.

24. Worle-Knirsch, J. M.; Pulskamp, K.; Krug, H. F. Oops they did it again! Carbon nanotubes hoax scientists in viability assays. *Nano Lett.,* **2006,** *6*, 1261-1268.

25. Baskin, D. S.; Widmayer, M. A.; Sharpe, M. A. Quantification of DNase type I ends, DNase type II ends, and modified bases using fluorescently labeled ddUTP, terminal deoxynucleotidyl transferase, and formamidopyrimidine-DNA Glycosylase. *Biotechniques,* **2010**, 49, 505-512.

26. Frank, S.; Steffens, S.; Fischer U.; Tlolko A.; Rainov N. G.; Kramm, C. M. Differential cytotoxicity and bystander effect of the rabbit cytochrome P450 4B1 enzyme gene by two different prodrugs: implications for pharmacogene therapy. *Cancer Gene Ther*., **2002**, *9*, 178-88.

27. Morelock, M. M.; Hunter, E. A.; Moran, T. J.; Heynen, S.; Laris, C.; Thieleking, M.; Akong, M.; Mikic, I.; Callaway, S.; DeLeon, R. P.; *et al*. Statistics of assay validation in high throughput cell imaging of nuclear factor kappaβ nuclear translocation. *Assay Drug Dev. Tech.,* **2005**, *3*, 483-499.

28. Nakatsu, S.; Kondo, S.; Kondo, Y.; Yin, D.; Peterson, J. W.; Kaakaji, R.; Morimura, T.; Kikuchi, H.; Takeuchi, J.; Barnett, G. H. Induction of Apoptosis in Multi-Drug Resistant (MDR) Human Glioblastoma Cells by SN-38, a Metabolite of the Camptothecin Derivative CPT-11. *Cancer Chemo. Pharmacol.* **1997**, *39,* 417-423.

29. Baskin, D. S.; Widmayer, M. A.; Sharpe, M. A. Quantification and calibration of images in fluorescence microscopy. *Anal. Biochem.,* **2010**, *404*, 118-126.

30. Upreti, M.; Lyle, C. S.; Skaug, B.; Du, L.; Chambers, T. C. Vinblastine-induced apoptosis is mediated by discrete alterations in subcellular location, oligomeric

structure, and activation status of specific Bcl-2 family members. *J. Biol. Chem.,* **2006**, *281*, 15941-15950.

31. Huang, Y. T.; Huang, D. M.; Guh, J. H.; Chen, I. L.; Tzeng, C. C.; Teng, C. M. CIL-102 interacts with microtubule polymerization and causes mitotic arrest following apoptosis in the human prostate cancer PC-3 cell line. *J. Biol. Chem.,* **2005**, *280*, 2771-2779.
32. Wang, G. J.; Jackson, J. G.; Thayer, S. A. Altered distribution of mitochondria impairs calcium homeostasis in rat hippocampal neurons in culture. *J. Neurochem.,* **2003**, *87*, 85-94.
33. Hickson, J.; Ackler, S.; Klaubert, D.; Bouska, J.; Ellis, P.; Foster, K.; Oleksijew, A.; Rodriguez, L.; Schlessinger, S.; Wang, B.; *et al*. Noninvasive molecular imaging of apoptosis *in vivo* using a modified firefly luciferase substrate, Z-DEVD-aminoluciferin. *Cell. Death. Differ.,* **2010**, *17*, 1003-1010.
34. Boland,B.; Kumar, A.; Lee,S.; Platt, F.M.; Wegiel, J.; Yu, W. H.; Nixon, R.A. Autophagy induction and autophagosome clearance in neurons: relationship to autophagic pathology in alzheimer's disease. *J. Neurosci*., **2008**, *28*, 6926-6937.
35. Wagner, B.; Natarajan, A.; Grünaug, S.; Kroismayr, R.; Wagner, E. F.; Sibilia, M. Neuronal survival depends on EGFR signaling in cortical but not midbrain astrocytes. *Eur. Mol. Bio. Org. J.,* **2006**, *25*, 752-762.
36. Fillmore, H. L.; Shultz, M. D.; Henderson, S. C.; Cooper, P.; Broaddus, W. C.; Chen, Z. J.; Shu, C. Y.; Zhang, J. F.; Ge, J. C.; Dorn, H. C.; *et al*. Conjugation of functionalized gadolinium metallofullerenes with IL-13 peptides for targeting and imaging glial tumors. *Nanomed.,* **2011**, *6*, 449-458.

37. Tateki Kubo, T.; Yamashita, T.; Yamaguchi, A.; Sumimoto, H.; Hosokawa, K,; Tohyama, M. A Novel FERM domain including guanine nucleotide exchange factor is involved in rac signaling and regulates neurite remodeling. *J. Neurosci.,* **2002**, *22*, 8504-8513.

4.7. Experimental Contributions

I synthesized and purified the PEG-HCCs. Also, I prepared several Drug/PEG-HCCs formulations in which the drug concentration and/or the nanoparticles concentration was varied in order to determine the most stable proportion of both components. Martyn Sharpe ran the cells studies.

Chapter 5

Improved Synthesis of Graphene Oxide

This chapter was entirely copied from the reference #1 of this section

5.1. Introduction

Graphene has enjoyed significant recent attention.[2] Graphene is a single atomic layer of sp^2 carbon atoms. Few- and single-layer transferable graphene nanosheets were first obtained by mechanical exfoliation ("Scotch-tape" method) of bulk graphite[3] and by epitaxial chemical vapor deposition.[4] Although those routes might be preferred for precise device assembly, they can be less effective for large-scale manufacturing. Chemical means are a practical approach to bulk-scale graphene materials.[5] The primary obstacle to achieving individual or few-layer graphene is overcoming the enormous interlayer van der Waals forces. To date, chemical efforts at graphite exfoliation have

been focused primarily on intercalation, chemical derivatization, thermal expansion, oxidation-reduction, the use of surfactants, or some combination thereof.[6-14]

The most common approach to graphite exfoliation is the use of strong oxidizing agents to yield graphene oxide (GO), a non-conductive hydrophilic carbon material.[15-18]Although the exact structure of GO is difficult to determine, it is clear that for GO the previously contiguous aromatic lattice of graphene is interrupted by epoxides, alcohols, ketone carbonyls and carboxylic groups.[19-21] The disruption of the lattice is reflected in an increase in interlayer spacing from 0.335 nm for graphite to more than 0.625 nm for GO.[22] Brodie first demonstrated the synthesis of GO in 1859 by adding a portion of potassium chlorate to a slurry of graphite in fuming nitric acid.[23] In 1898 Staudenmaier improved on this protocol by using concentrated sulfuric acid as well as fuming nitric acid and adding the chlorate in multiple aliquots over the course of the reaction. This small change in the procedure made the production of highly oxidized GO in a single reaction vessel significantly more practical.[24] In 1958, Hummers reported the method most commonly used today: the graphite is oxidized by treatment with $KMnO_4$ and $NaNO_3$ in concentrated H_2SO_4.[16] It should be noted that all three of these procedures involve the generation of the toxic gas(es) NO_2, N_2O_4, and/or ClO_2; the latter also being explosive.

The most common source of graphite used for chemical reactions, including its oxidation, is flake graphite, which is a naturally occurring mineral that is purified to remove heteroatomic contamination.[25] GO prepared from flake graphite can be readily dispersed in water and has been used on a large scale for preparing large graphitic films, as a binder for carbon products and as a component of the cathode of lithium batteries.[26-

[29] Moreover, the hydrophilicity of GO allows it to be uniformly deposited onto substrates in the form of thin films, which is necessary for applications in electronics.[30] It is also often essential that the GO can be transformed back into a conductive graphitic material, and indeed, either in thin films or in bulk, partial restoration of the graphitic structure can be accomplished by chemical reduction[13,30-32] to chemically converted graphene (CCG). However, the graphitic structure (with its desired properties) is not fully restored using these conditions, and significant defects are introduced.[33]

Recently, we reported the scaleable preparation of graphene oxide nanoribbons (GONRs) from multi-walled carbon nanotubes by treatment with $KMnO_4$ and concentrated H_2SO_4[31] and the discovery that the addition of phosphoric acid (H_3PO_4) to this reaction produced GONRs with more intact graphitic basal planes.[34] Reduction of these second-generation GONRs produced ribbons that were comparable in conductivity to those prepared by reduction of the first generation GONRs. We hypothesized that this oxidation procedure ($KMnO_4$ and a 9:1 mixture of concentrated H_2SO_4:H_3PO_4, called the "improved method" for clarity of discussion in this paper) could be used to prepare improved GO (IGO) with fewer defects in the basal plane as compared to GO prepared by the Hummers' method. The IGO synthesis was evaluated in comparison to Hummers' method or Hummers' method with additional $KMnO_4$. For clarity, we have named the GO produced by these methods: IGO, HGO and HGO+, respectively. The improved method provides a greater amount of hydrophilic oxidized graphite material relative to the other two procedures. Moreover, even though IGO is as oxidized as HGO+ and both are more oxidized than HGO, IGO has a more regular structure with a greater amount of basal plane framework retained. This is reflected in the fact that when all three GOs are

reduced with hydrazine hydrate, the CCG produced from IGO (CCIG) showed an equivalent level of conductivity with respect to the material produced from the other two methods (CCHG, CCHG+). The advantages of the improved method, with its simpler protocol, higher yield, no toxic gas evolution during preparation and equivalent conductivity upon reduction, make it an attractive material for preparation on a large-scale. It may also show improved performance in materials applications, such as in membranes, TEM grids or temperature-sensitive device fabrication.

5.2. Experimental Procedures

Graphite flakes (Sigma-Aldrich, cat # 332461, ~150 μm flakes) were oxidized using three different procedures: improved method, Hummers' method and Hummers' method with additional $KMnO_4$.

For the improved method a 9:1 mixture of conc H_2SO_4:H_3PO_4 (360:40 mL) was added to a mixture of graphite flakes (3.0 g, 1 wt equiv) and $KMnO_4$ (18.0 g, 6 wt equiv), producing a slight exotherm to 35-40 °C. The reaction was then heated to 50 °C and stirred for 12 h. The reaction was cooled to rt and poured onto ice (~400 mL) with 30% H_2O_2 (3 mL). For work up, the mixture was sifted through a metal U.S Standard testing sieve (W.S Tyler, 300 μm) and then filtered through polyester fiber (Carpenter Co.) The filtrate was centrifuged (4000 rpm for 4 h) and the supernatant was decanted away. The remaining solid material was then washed in succession with 200 mL of water, 200 mL of 30% HCl, and 200 mL of ethanol (2×); for each wash the mixture was sifted through the U.S Standard testing sieve, and then filtered through polyester fiber with the filtrate being centrifuged (4000 rpm for 4 h) and the supernatant decanted away. The material

remaining after this extended, multiple-wash process was coagulated with 200 mL of ether, and the resulting suspension was filtered over a PTFE membrane with a 0.45 μm pore size. The solid obtained on the filter was vacuum dried overnight at room temperature, obtaining 5.8 g of product.

For Hummers' method, concentrated H_2SO_4 (69 mL) was added to a mixture of graphite flakes (3.0 g, 1 wt equiv) and $NaNO_3$ (1.5 g, 0.5 wt equiv), and the mixture was cooled to 0 °C. $KMnO_4$ (9.0 g, 3 wt equiv) was added slowly in portions to keep the reaction temperature below 20 °C. The reaction was warmed to 35 °C and stirred for 30 min, at which time water (138 mL) was added slowly, producing a large exotherm to 98 °C. External heating was introduced to maintain the reaction temperature at 98 °C for 15 min, then the heat was removed and the reaction was cooled using a water bath for 10 min. Additional water (420 mL) and 30% H_2O_2 (3 mL) were added, producing another exotherm. After air cooling, the mixture was purified as described for the IGO above (sifting, filtration, multiple washings, centrifugations and decanting, vacuum drying) to give 1.2 g of solid.

The third method makes use of the Hummers' reagents with additional $KMnO_4$. We call this method Hummers' method+ and its product HGO+. Concentrated H_2SO_4 (69 mL) was added to a mixture of graphite flakes (3.0 g, 1 wt equiv) and $NaNO_3$ (1.5 g, 0.5 wt equiv), and the mixture was cooled using an ice bath to 0 °C. $KMnO_4$ (9.0 g, 3 wt equiv) was added slowly in portions to keep the reaction temperature below 20 °C. The reaction was warmed to 35 °C and stirred for 7 h. Additional $KMnO_4$ (9.0 g, 3 wt equiv) was added in one portion, and the reaction was stirred for 12 h at 35 °C. The reaction mixture was cooled to room temperature and poured onto ice (~400 mL) with 30% H_2O_2

(3 mL). The mixture was then purified following the previous protocol of sifting, filtering, centrifugation, decanting with multiple washes followed by a final vacuum drying to give 4.2 g of solid product.

5.3. Results and Discussion

The increased efficiency of the IGO method as compared to the HGO and HGO+ methods was apparent after the first purification step for each method. The hydrophilic carbon material produced during the reaction passed through the sieve while the under-oxidized hydrophobic carbon material was retained on the sieve due to its particle size and low water solubility. Significantly less under-oxidized material was generated in the production of IGO (0.7 g) compared to HGO (6.7 g) or HGO+ (3.9 g). Note that these weights correspond to the under-oxidized graphene and any water that was retained after drying overnight in vacuum; the HGO and HGO+ had a wet appearance (Figure 5.1).

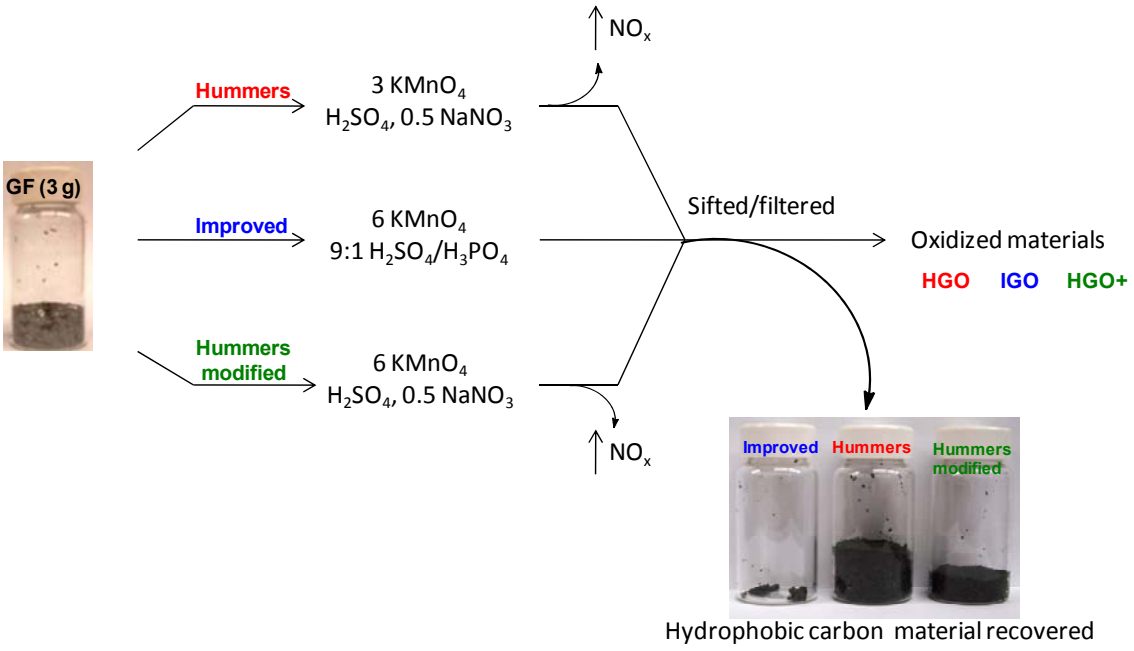

Figure 5.1. Representation of the procedures followed starting with graphite flakes (GF). Under-oxidized hydrophobic carbon material recovered during the purification of IGO, HGO, and HGO+. The increased efficiency of the IGO method is indicated by the very small amount of under-oxidized material produced.

Following purification, the hydrophilic materials obtained (IGO, HGO, HGO+) were characterized. Raman and infrared spectroscopy indicated that all three materials were similar. Raman spectra show D peaks ~ 1590 cm^{-1} and G peaks ~ 1350 cm^{-1}, confirming the lattice distortions (Figure 5.2A). Also, FTIR-ATR spectra (Figure 5.2B) were recorded and the following functional groups were identified in all samples: O-H stretching vibrations (3420 cm^{-1}), C=O stretching vibration (1720-1740 cm^{-1}), C=C from unoxidized sp^2-CC bonds (1590-1620 cm^{-1}) and C-O vibrations (1250 cm^{-1}).

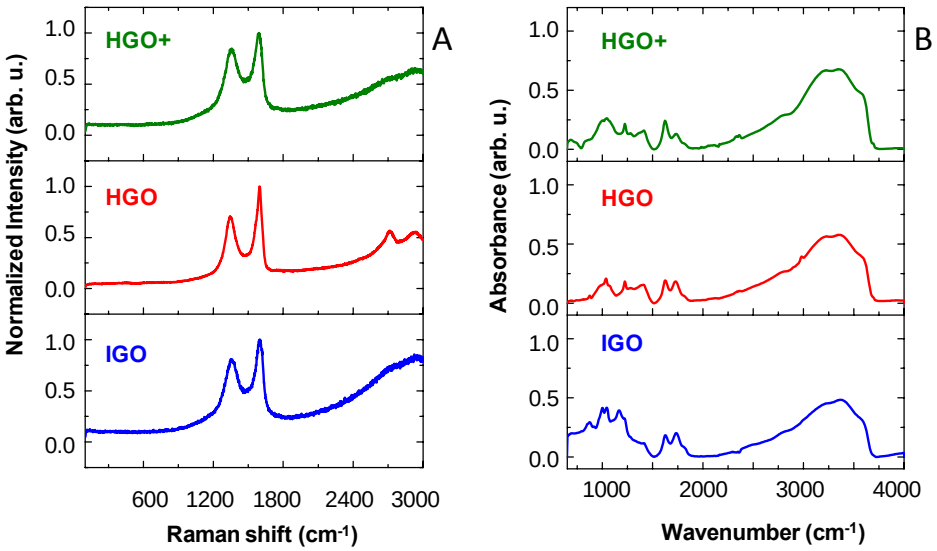

Figure 5.2. (A) Raman spectra recorded using 514 nm laser excitation and (B) FTIR-ATR spectra of HGO+, HGO, and IGO.

Atomic force microscopy (AFM) images (Figure 5.3) also indicated that the three materials were similar, as the thickness of the IGO, HGO+, and HGO layers were all ~ 1.1 nm.

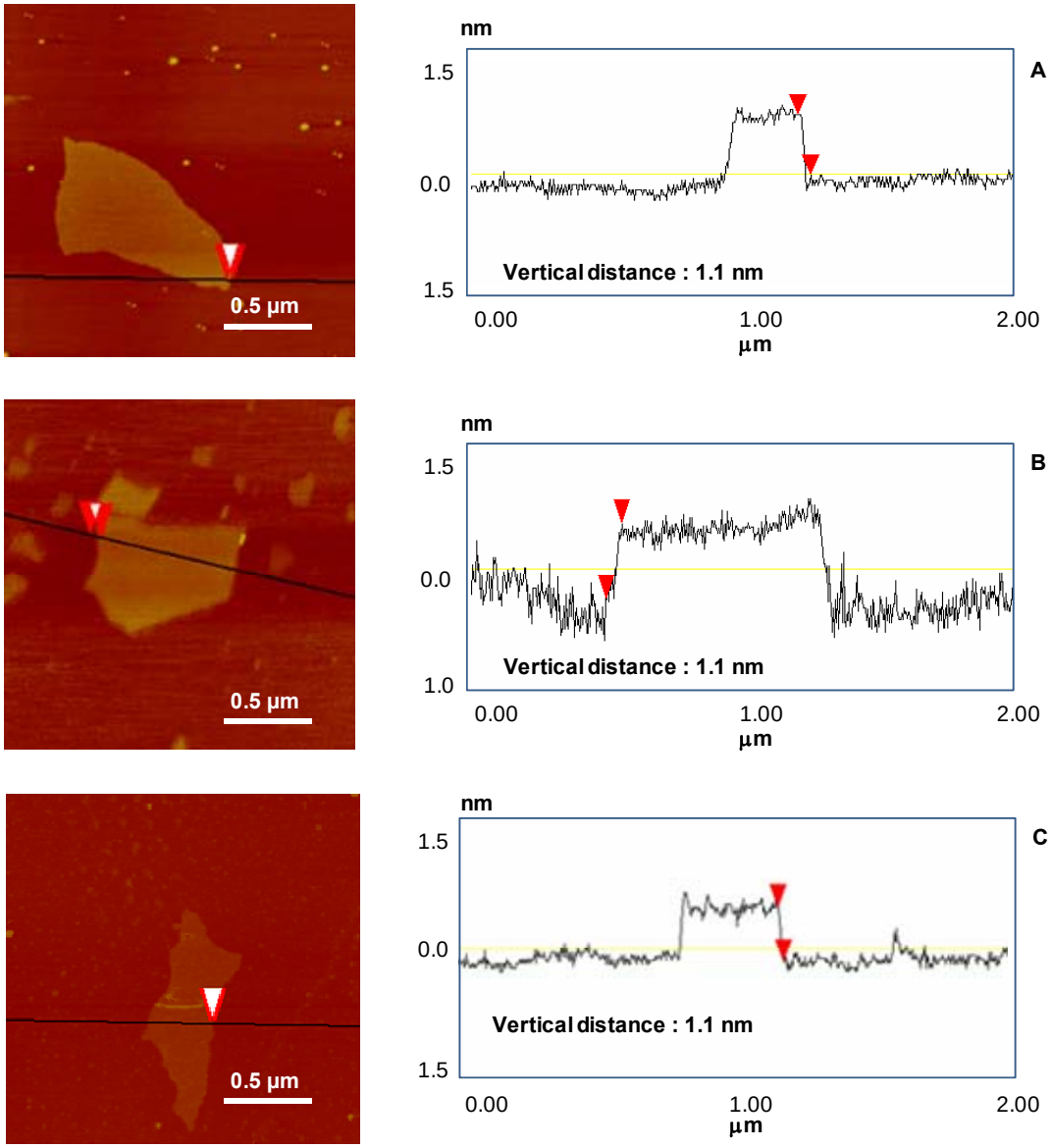

Figure 5.3. Tapping mode AFM topographic images and height profiles of a single layer of (A) HGO+, (B) HGO, and (C) IGO.

A variety of techniques indicated that the order of overall oxidation is HGO < HGO+ < IGO. Thermogravimetric analysis (TGA) of the materials (Figure 5.4) showed major weight losses between 150-300 ºC, which corresponds to CO, CO_2, and steam

release[11] from the most labile functional groups. Between 400-950 ºC, a slower mass loss was observed and can be attributed to the removal of more stable oxygen functionalities.[35] By TGA, HGO+ had the smallest weight loss while HGO and IGO had similar weight losses.

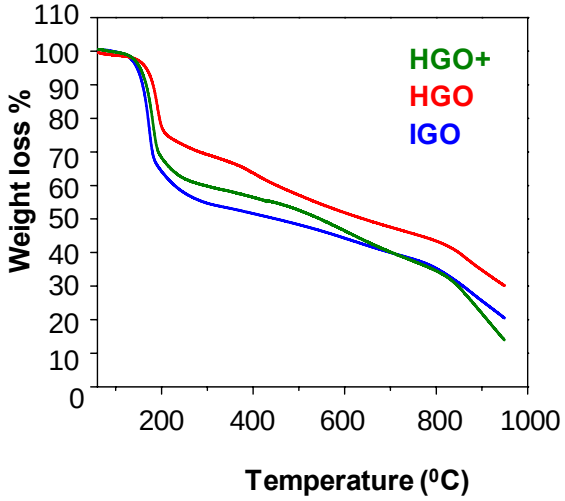

Figure 5.4. TGA plots of HGO+, HGO, and IGO.

Solid state ^{13}C NMR (Figure 5.5) suggests that the order of overall oxidation is HGO < HGO+ < IGO. The signals can be assigned as described previously:[11,36,37] ketone carbonyls near 190 ppm; ester and lactol carbonyls near 164 ppm, graphitic sp^2 carbons near 131 ppm, lactols O-C(sp^3)-O near 101 ppm, and alcohols at about 70 ppm with an upfield intense signal from epoxides near 61 ppm. The simplest measure of oxidation is the ratio between the alcohol/epoxide signal and graphitic sp^2 carbon signal. This ratio is greatest for IGO and least for HGO. It is also noteworthy that IGO appears to have more epoxide functionalities than either of the other GOs.

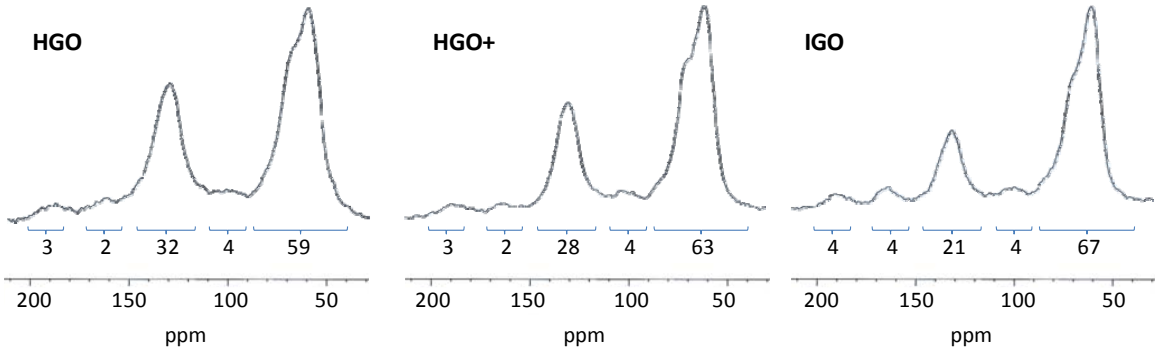

Figure 5.5. 50.3 MHz ^{13}C NMR spectra obtained of HGO, HGO+ and IGO [12 kHz magic angle spinning (MAS), a 90° ^{13}C pulse, 41-ms FID, and 20-s relaxation delay]. Integration areas are shown under each peak.

The X-ray diffraction (XRD) spectra (Figure 5.6) support the same order of overall oxidation. For XRD, the interlayer spacing of the materials is proportional to the degree of oxidation. The spacings are 9.5 Å, 9.0 Å, and 8.0 Å for IGO, HGO+ and HGO, respectively. Also, the HGO spectrum had a peak at 3.7 Å, indicating traces of starting material (graphite flakes) were present in the sample.

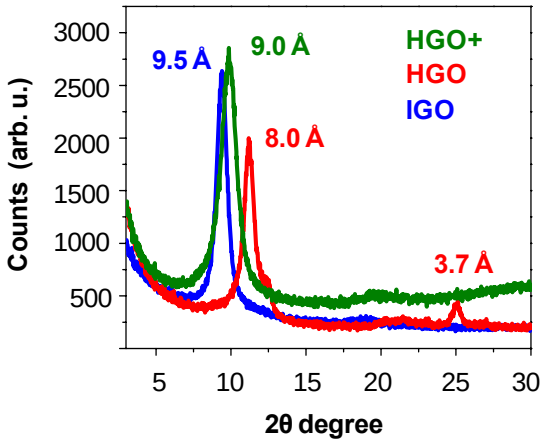

Figure 5.6. XRD spectra of HGO, HGO+ and IGO (1.54059 Å Cu/K-alpha 1 as wavelength).

The X-ray photoelectron spectroscopy (XPS) spectra of the samples both support the conclusion that IGO is the most oxidized material and suggest that the IGO has a more organized structure than the other two materials. To determine the relative levels of oxidation, the C/O ratio was not used; it is unreliable because it is so difficult to fully dehydrate a GO sample.[38] Instead, the C1s spectra were compared by deconvoluting (Multipack software, version 7.0) each spectrum into four peaks that correspond to the following functional groups: carbon sp^2 (C=C, 284.8 eV), epoxy/hydroxyls (C-O, 286.2 eV), carbonyl (C=O, 287.8 eV) and carboxylates (O-C=O, 289.0 eV).[10] All percentages of the oxidized materials were combined such that IGO had 69% oxidized carbon and 31% graphitic carbon; HGO+ had 63% and 37%; HGO contained 61% and 39% of the oxidized carbon and graphitic carbon, respectively. The C1s XPS spectra were then normalized with respect to the C=C peak (Figure 5.7). The degree of oxidation for each sample is similar to the amount indicated by ^{13}C NMR. IGO is the most oxidized material, HGO+ is slightly (~10%) less oxidized and HGO is the least oxidized. Moreover, the apparent peak at ~286 eV, corresponding to the oxidized carbons for IGO, is sharper than the same peak for HGO+. This suggests that for similar levels of overall oxidation, the IGO has a more regular structure than that of HGO+.[39]

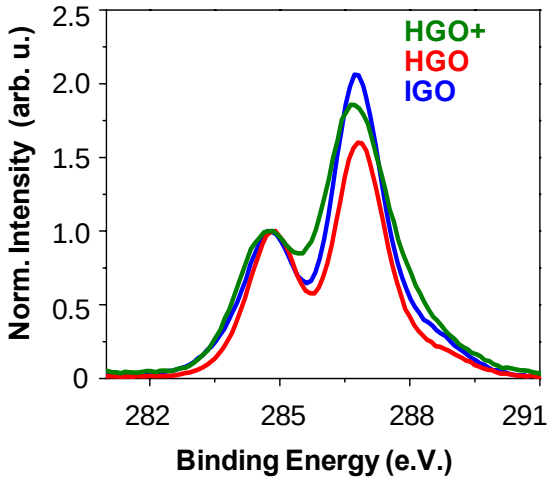

Figure 5.7. The C1s XPS spectra of HGO+, HGO, and IGO normalized with respect to the C=C peak.

Transmission electron microscopy (TEM) images of the three samples support the assertion that IGO has a more regular structure than either HGO+ or HGO (Figure 5.8). All three procedures produce large flakes of GO that are a few layers thick; however, the diffraction patterns indicate differences in crystallinity. HGO is modestly crystalline, but when the more highly oxidized HGO+ is analyzed, an amorphous structure is indicated by the diffuse diffraction pattern.[30,40] In comparison, the IGO is highly oxidized but has the sharpest diffraction pattern of all three samples, again suggesting that IGO has a more regular carbon framework than HGO or HGO+.

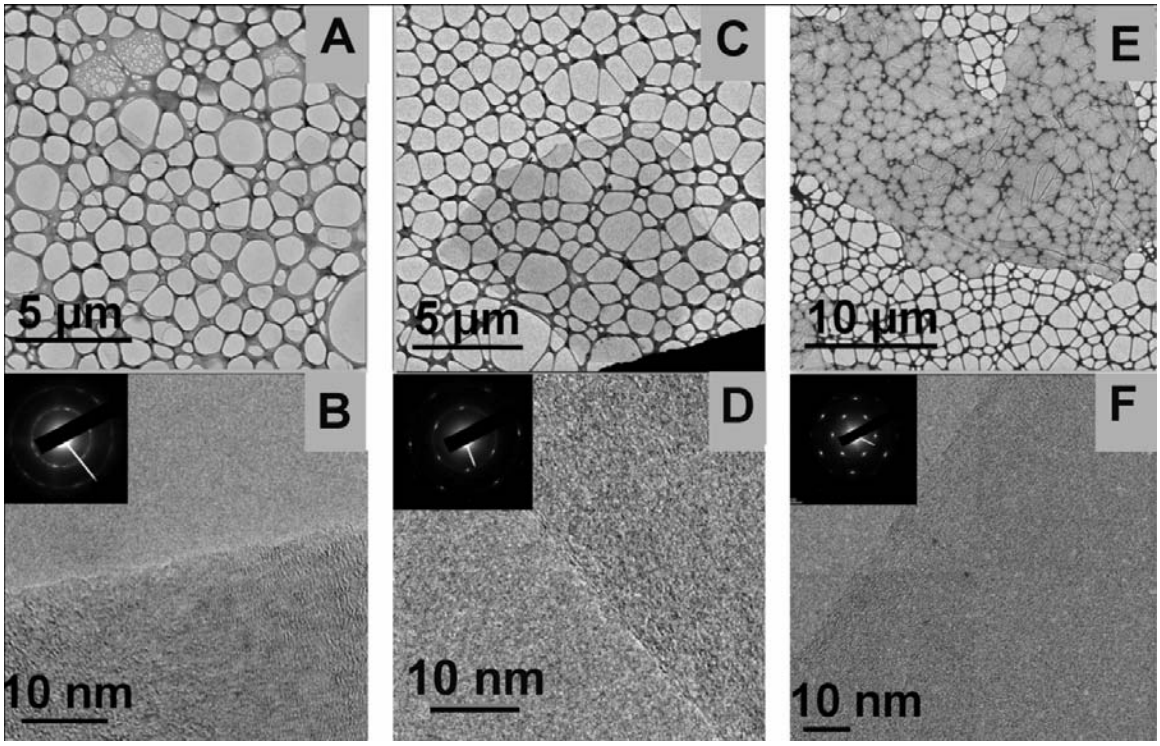

Figure 5.8. TEM images of (A) HGO+, (C) HGO, (E) IGO and their diffraction patterns (B), (D), and (F) respectively. Insets are the selected area electron diffraction (SAED) patterns corresponded to the graphene films in the TEM images. TEM grids with lacey carbon support films (Ted Pella, Inc.) were used to prepare the samples.

The UV/Vis spectra of the three materials suggest that the more ordered structure of IGO is due to greater retention of carbon rings in the basal planes. The three spectra were recorded for an equal concentration of each material (Figure 5.9). The degree of remaining conjugation can be determined by the λ_{max} of each UV/Vis spectrum. The more $\pi \rightarrow \pi^*$ transitions (conjugation), the less energy needs to be used for the electronic transition, which results in a higher λ_{max}. IGO, HGO+ and HGO all have a very similar λ_{max}, which is in the 227-231 nm range as previously reported for GO.[13,41] Also, for all

three materials, a similar shoulder around ~300 nm is observed and can be attributed to n-π* transitions of the carbonyl groups. This suggests that the materials are grossly similar in structure, as the Raman, IR and AFM data indicated. However, IGO has a larger extinction coefficient than those of HGO+ or HGO, suggesting that for an equal amount of each sample, the IGO has more aromatic rings or isolated aromatic domains retained. The λ_{max} data indicates that these aromatic rings are not in extended conjugation, but the overall absorption indicates that IGO has more aromatic rings retained.

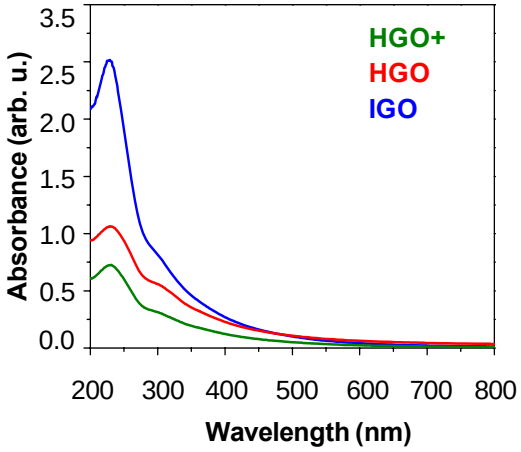

Figure 5.9. UV/vis spectra recorded in aqueous solutions at 0.05 mg/mL of HGO+, HGO, and IGO.

Bulk samples of the oxidized materials were reduced using hydrazine hydrate and then annealed at 300 °C and at 900 °C in Ar/H_2. In general, for the hydrazine reduction, 100 mg of the IGO, HGO or HGO+ material was dispersed in 100 mL of DI water, stirred for 30 min and then 1.00 mL of hydrazine hydrate was added. The mixtures were heated at 95 ºC using a water bath for 45 min; a black solid precipitated from the

reaction mixture. Products were isolated by filtration (PTFE 20 μm pore size) and washed with DI water (50 mL 3×) and methanol (20 mL 3×), producing 54 mg, 57 mg, and 76 mg of the reduced chemically converted IGO (CCIG), chemically converted HGO+ (CCHG+) and chemically converted HGO (CCHG), respectively. After reduction, no signal from oxidized carbons could be detected. Only a broad aromatic/alkene NMR signal could be detected for CCHG, CCHG+, and CCIG. This signal was shifted upfield relative to that in the precursor HGO, HGO+, and IGO; the peak maximum after reduction was at about 118 ppm, very similar to that noted previously[36] on other samples of reduced GO. Reduction also had an effect similar to that previously noted[36] on the drive pressure required to spin the rotor and on the tuning and matching of the ^{13}C and ^{1}H channels of the probe. After reduction and annealing in Ar/H_2 at 900 °C, no NMR signal could be detected for any of the samples, consistent with their becoming even more graphite-like.[36]

XPS analysis of the black solids showed similar levels of reduction for all three materials when they were hydrazine reduced and when they were annealed (Figure 5.10; in Figures 5.10B and 5.10C the annealed materials are designated by the prefix “ann” to differentiate them from the materials that were only hydrazine reduced). Atomic compositions for CCHG+ were C(1s) 89%, N(1s) 3%, and O(1s) 8%; for CCHG: C(1s) 88%, N(1s) 3%, and O(1s) 9%; and for CCIG C(1s) 86%, N(1s) 5%, O(1s) 9%, and P(2p) <0.1% (the amount is lower than the detection level of the instrument).

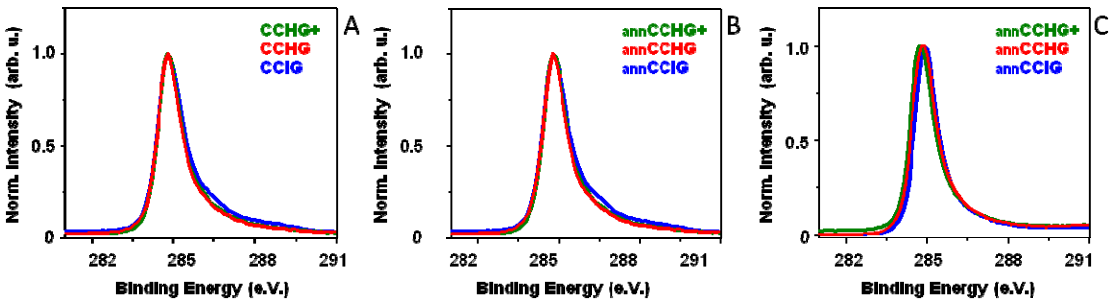

Figure 5.10. The C1s XPS spectra of (A) hydrazine reduced (B) further 300 °C/H_2-annealed materials (C) 900 °C/H_2-annealed materials. The annealed materials in panels B and C are designated by the prefix "ann" to differentiate them from the materials in A that were only hydrazine reduced.

In order to estimate the degree of graphitization with greater precision for each material after being reduced, electrical conductivities were measured. Figure 5.11 displays scanning electron microscopy (SEM) images of typical CCIG flakes, which were deposited on a Si/SiO_2 substrate and then reduced by hydrazine vapor. For the hydrazine vapor reduction, Si/SiO_2 substrates coated with GO were deposited inside a beaker with 0.5 mL of hydrazine hydrate and covered with foil. The system was heated using a water bath at 95 ºC for 45 min. The material was well-exfoliated; the majority of the flakes on the chip were only a few layers thick and several tens of microns in diameter. As an example, Figure 5.11A shows an individual flake, which is 60 µm in diameter and, based on AFM data, is only 2 nm thick. Typically, the thicknesses of monolayer GO flakes are

in the range of 0.7 – 1 nm,[11,41-44] so the shown flake most likely consists of 2 layers. The largest flake in Figure 5.11B is 160 μm in diameter.

As-prepared HGO, HGO+ and IGO flakes were deposited on Si/SiO_2 substrates (heavily doped p-type Si with a 500 nm thermal SiO_2 layer), dried in air and then reduced by hydrazine vapor in the same flask so that they were exposed to identical reaction conditions. Individual flakes of reduced graphene materials with thicknesses ranging from 1 - 3 nm were selected for device fabrication. Electronic devices were patterned by standard e-beam lithography (we used PMMA as a positive resist), and then 20-nm-thick Pt contacts were formed by e-beam evaporation and lift-off process. Figure 5.11C shows a SEM image of a typical electronic device.

The electrical measurements were performed using a probe station (Desert Cryogenics TT-probe 6 system) under vacuum with chamber base pressure below 10^{-5} Torr. Normally, the devices were kept under vacuum for at least 2 d before the measurements. The current-voltage (*IV*) data were collected on an Agilent 4155C semiconductor parameter analyzer. All CCG flakes in the fabricated electronic devices exhibited qualitatively the same electrical properties. They behaved as p-type semiconductors in air, but exhibited ambipolar electric field effect in vacuum after several days of evacuation in the probe station chamber at ~10^{-5} Torr (Figure 5.11D).[32,45-47] This effect can be attributed to the desorption of the atmospheric adsorbates that are known to cause doping effects in graphene.[48] This effect was completely reversible; after exposure to air the CCG flakes again behaved as p-type semiconductors. For the monolayer (with thickness of about 1 nm) CCHG, CCHG+ and CCIG flakes, we also compared electrical properties. CCHG and CCHG+ devices exhibited approximately the

same conductivity values ~ 0.05 S/cm, whereas CCIG monolayers were about twice as conductive (~ 0.1 S/cm); the above numbers were averaged for 3-5 devices. However, considering significant variability in conductivities, found by us for each set of the devices and also reported elsewhere,[43] it is difficult to conclude whether or not hydrazine-reduced IGO flakes are indeed more conductive than their HGO and HGO+ counterparts. Importantly, these numbers where obtained by 4-probe technique for the flakes that were hydrazine-reduced from the original materials under the same conditions.

Since the hydrazine reduction was not sufficient to achieve high conductivities of the flakes, we further reduced the CCG materials by annealing in Ar/H_2 at high temperatures. Additionally, we fabricated electronic devices based on monolayer CCHG, CCHG+ and CCIG flakes annealed in Ar/H_2 at 300 or 900 ºC for 0.5 h. For these thermally annealed materials, we measured at least 6 devices for each material. We found that after the thermal treatment at 300 ºC, the conductivities of the annCCG materials dramatically increase up to 2.1 ± 1.4 S/cm (annCCHG), 6.8 ± 4.4 S/cm (annCCHG+) and 3.5 ± 2.5 S/cm (annCCIG); the scatter plot is shown in Figure 5.11E. The annCCHG is statistically significantly less conductive than the other two samples ($p < 0.05$, t-test assuming equal variance), but due to the small number of devices for annCCHG+ it is difficult to determine if the annCCHG+ and annCCIG are significantly different. The statistical significance of the increase in conductivity for annCCHG+ compared to annCCIG is marginal ($p = 0.04$, t-test assuming equal variance) and completely driven by the outlier point at 15.0 (removing this point, $p = 0.24$, t-test assuming equal variance). Here, as well as in other cases, the conductivities were calculated assuming the thicknesses of the flakes to be 1 nm. CCG materials annealed at even higher temperature

of 900 ºC exhibit further increases in conductivities up to 375 ± 215 S/cm (annCCHG), 350 ± 125 S/cm (annCCHG+) and 400 ± 220 S/cm (annCCIG) (Figure 5.11F). There is no statistically significant difference between any of the samples after annealing at 900 °C, suggesting that high temperature annealing eliminates most of the differences in composition and structure present in the three samples.

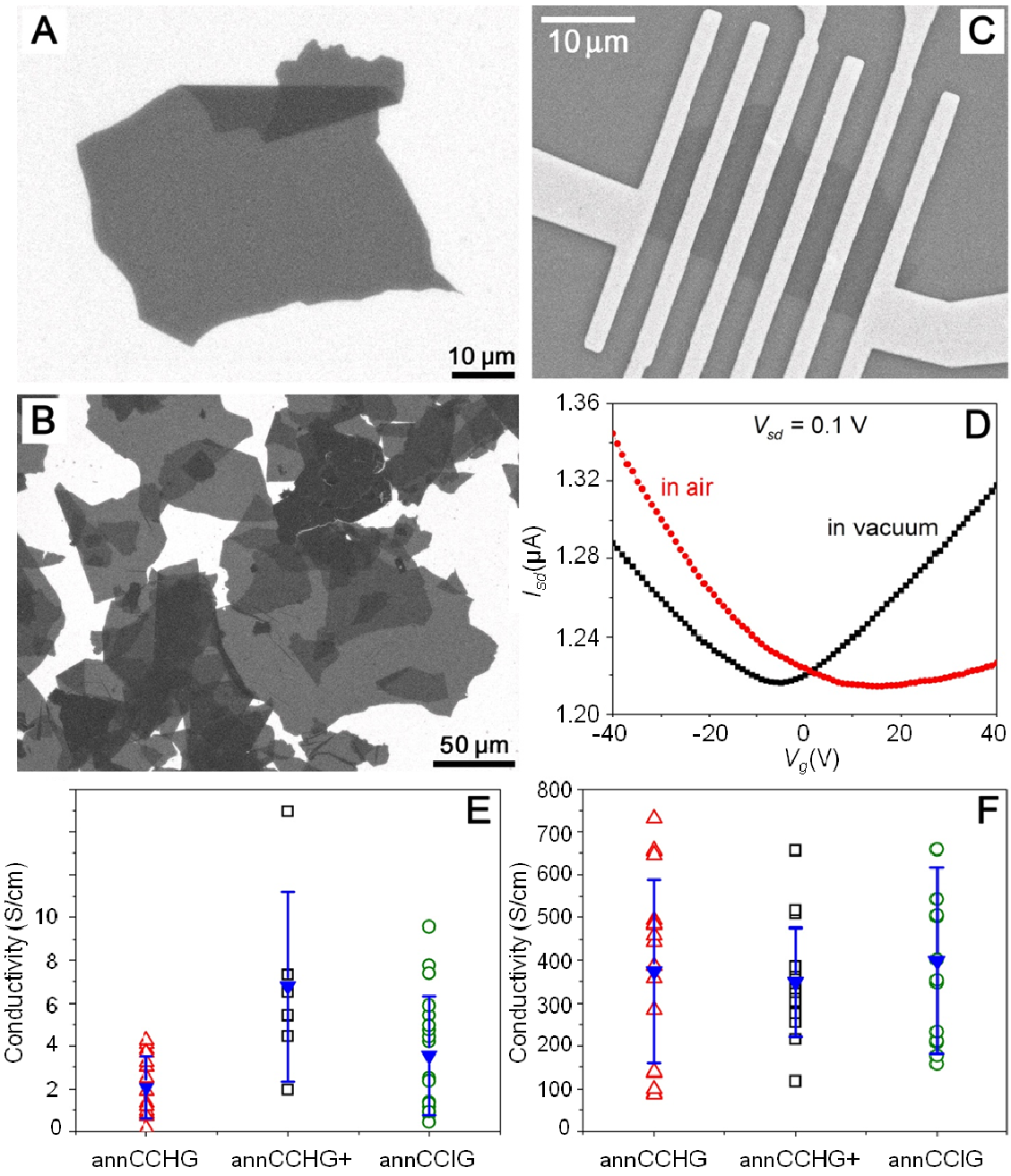

Figure 5.11. Images and conductivities of the CC flakes. (A) and (B) show SEM images of CCIG flakes on Si/SiO_2 substrate. (C) SEM image of a typical electronic device for a hydrazine-reduced CCIG flake. (D) Source-drain current (*Isd*) – gate voltage (*Vg*) characteristics of the same electronic device based on a few-layer CCIG flake measured in air and in vacuum after 3 d evacuation in the probe station chamber at the pressure of $\sim 10^{-5}$ Torr. (E) Plot of the mean conductivities for the monolayer annCCHG, annCCHG+ and annCCIG flakes annealed in Ar/H_2 at 300 ºC for 0.5 h. (F) Plot of the mean conductivities for the monolayer annCCHG, annCCHG+ and annCCIG flakes annealed in Ar/H_2 at 900 ºC for 0.5 h.

5.4. Conclusions

The improved method for producing GO has significant advantages over Hummers' method. The protocol for running the reaction does not involve a large exotherm and produces no toxic gas. Moreover, the improved method yields a higher fraction of well-oxidized hydrophilic carbon material. This IGO is more oxidized than HGO and slightly more oxidized than HGO+. The IGO possesses a more regular structure than the other materials. An increased number of isolated aromatic rings could be a component of this more regular framework structure. This suggests that the improved method might disrupt the basal plane of the graphite less than Hummers' method. The mechanism for producing IGO with a more regular structure could be based on the formation of five-membered cyclic phosphate groups between the phosphoric acid and two vicinal diols formed on the graphite basal plane.[33] Taken together, this data

suggests that the improved method could be advantageous for large-scale production of GO.

5.5. Acknowledgments

We thank the Alliance for Nanohealth (W8XWH-07-2-0101), M-I-SWACO, Air Force Research Laboratory through University Technology Corporation, 09-S568-064-01-C1, US Department of Energy's Office of Energy Efficiency and Renewable Energy within the Hydrogen Sorption Center of Excellence, DE-FC-36-05GO15073, the Office of Naval Research MURI program on graphene, the AFOSR, FA9550-09-1-0581 and the Federal Aviation Administration (2007G010) for financial support.

5.6. References

1. Marcano, D. C.; Kosynkin, D. V.; Berlin, J. M.; Sinitskii, A.; Sun, Z.; Slesarev, A.; Alemany, L. B.; Lu, W.; Tour, J. M. Improved synthesis of graphene oxide. *ACS Nano,* **2010**, *4*, 4806-4814.
2. Geim, A. K.; Novoselov, K. S. The rise of graphene. *Nature Mater.,* **2007**, *6*, 183-191.
3. Novoselov, K. S.; Geim, A. K.; Morozov, S. V.; Jiang, D.; Zhang,Y.; Dubonos, S. V.; Grigorieva, I. V.; Firsov, A. A. Electric field effect in atomically thin carbon films. *Science,* **2004**, *306*, 666-669.

4. Berger, C.; Song, Z.; Li, X.; Wu, X.; Brown, N.; Naud, C.; Mayou, D.; Li, T.; Hass, J.; Marchenkov, A. N.; Conrad, E. H.; First, P. N.; de Heer, W. A. Electronic confinement and coherence in patterned epitaxial graphene. *Science,* **2006**, *312*, 1191-1196.

5. Ruoff, R. Graphene calling all chemists. *Nat. Nanotechnol.,* **2008**, *3*, 10-11.

6. Chakraborty, S.; Guo, W.; Hauge, R. H.; Billups, W. E. Reductive alkylation of fluorinated graphite. *Chem. Mater.,* **2008**, *20*, 3134-3136.

7. Schniepp, H. C.; Li, J. L.; McAllister, M. J.; Sai, H.; Herrera-Alonso, M.; Adamson, D. H.; Prud'homme, R. K.; Car, R.; Saville, D. A.; Aksay, I. A. Functionalized single graphene sheets derived from splitting graphite oxide. *J. Phys. Chem. B,* **2006**, *110*, 8535-8539.

8. Si, Y.; Samulski, E. T. Synthesis of water soluble graphene. *Nano Lett.,* **2008**, *8*, 1679-1682.

9. Lomeda, J. R.; Doyle, C. D.; Kosynkin, D. V.; Hwang, W. F.; Tour, J. M. Diazonium functionalization of surfactant-wrapped chemically converted graphene sheets. *J. Am. Chem. Soc.,* **2008**, *130*, 16201-16206.

10. Behabtu, N.; Lomeda, J. R.; Green, M. J.; Higginbotham, A. L.; Sinitskii, A.; Kosynkin, D. V.; Tsentalovich, D.; Parra-Vasquez, A. N. G.; A. Schmidt, J.; Kesselman, E.; Cohen, Y.; Talmon, Y.; Tour, J. M.; Pasquali, M. Spontaneous high-concentration dispersions and liquid crystals of graphene. *Nat. Nanotech*., **2010**, *5*, 406-411.

11. Stankovich, S.; Dikin, D. A.; Piner, R. D.; Kohlhaas, K. A.; Kleinhammes, A.; Jia, Y.; Wu, Y.; Nguyen, S. B. T.; Ruoff, R. S. Synthesis of graphene-based nanosheets via chemical reduction of exfoliated graphite oxide. *Carbon,* **2007**, *45*, 1558-1565.

12. Xu, Y.; Bai, H.; Lu, G.; Li, C.; Shi, G. Flexible graphene films via the filtration of water-soluble noncovalent functionalized graphene sheets. *J. Am. Chem. Soc.,* **2008**, *130*, 5856-5857.

13. Li, D.; Mueller, M. B.; Gilje, S.; Kaner, R. B.; Wallace, G. G. Processable aqueous dispersions of graphene nanosheets. *Nat. Nanotechnol.,* **2008**, *3*, 101-105.

14. Lotya, M.; Hernandez, Y.; King, P. J.; Smith, R. J.; Nicolosi, V.; Karlsson, L. S.; Blighe, F. M.; De, S.; Wang, Z.; McGovern, I. T.; Duesberg, G. S.; Coleman, J. N. Liquid phase production of graphene by exfoliation of graphite in surfactant/water solutions. *J. Am. Chem. Soc.,* **2009**, *131*, 3611-3620.

15. Higginbotham, A. L.; Lomeda, J. R.; Morgan, A. B.; Tour, J. M. Graphite oxide flame-retardant polymer nanocomposites. *App. Mater. Interfac*. **2009**, *1*, 2256-2261.

16. Hummers, W. S.; Offeman, R. E. Preparation of graphitic oxide. *J. Am. Chem. Soc.,* **1958**, *80*, 1339.

17. Lerf, A.; He, H.; Forster, M.; Klinowski, J. Structure of graphite oxide revisited. *J. Phys. Chem. B,* **1998**, *102*, 4477-4482.

18. Dreyer, D. R.; Park, S.; Bielawski, C. W.; Ruoff, R. The chemistry of graphene oxide. *Chem. Soc. Rev*., **2010**, *39*, 228–240.

19. He H.; Klinowski J.; Forster M. A New structural model for graphite oxide. *Chem. Phys. Lett.,* **1998**, *287*, 53-56.

20. Uhl, F.; Wilkie, C. Preparation of nanocomposites from styrene and modified graphite oxides. *Polym. Degrad and Stab*., **2004**, *84*, 215-226.

21. Stankovich,, S.; Piner, R.; Chen, X.; Wu, N.; Nguyen, S.; Ruoff, R. Stable aqueous dispersions of graphitic nanoplatelets via the reduction of exfoliated graphite oxide in the presence of poly(sodium 4-styrenesulfonate). *J. Mater. Chem*., **2006**, *16*, 155-158.

22. Hontoria-Lucas ,C.; López-Peinado, A.; López-González, J.; Rojas-Cervantes, M.; Martín-Aranda, R. Study of oxygen-containing groups in a series of graphite oxides: physical and chemical characterization. *Carbon,* **1995**, *33*, 1585-1592.

23. Brodie, B.C. On the atomic weight of graphite. *Phil Trans Roy Soc. London,* **1859**, *14*, 249-59.

24. Staudenmaier, L. Verfahren zur darstellung der graphitsäure. *Ber. Dtsch. Chem. Ges*., **1898**, *31*, 1481-1487.

25. Wissler, M. Graphite and carbon powders for electrochemical applications. *J. Power Sources,* **2006**, *156*, 142-150.

26. Ishikawa, T.; Nagaoki, T. Shin tanso kogyo (New carbon industry) 2nd ed. Tokyo: Kindai hensyusya; 1986, 125–36.

27. Maire, J.; Colas, H.; Maillard, P. Membranes de carbone et de graphite et leurs proprieties. *Carbon,* **1968**, *6*, 555–560.

28. Ishikawa, T.; Kanemaru, T.; Teranishi, H.; Onishi, K. Composites of oxidized graphite material and expanded graphite material. US. Patent 4094951, June 13, 1978.

29. Touzain, P.; Yazumi, R.; Maire J. Insertion compounds of graphite with improved performances and electrochemical applications of those compounds. US Patent 4584252, April 22, 1986.

30. Mkhoyan, K.; Contryman, A.; Silcox, J.; Stewart, D.; Eda, G.; Mattevi, C.; Miller, S.; Chhowalla, M. Atomic and electronic structure of graphene-oxide. *Nano Lett*., **2009**, *9*, 1058-1063.

31. Kosynkin, D.; Higginbotham, A.; Sinitskii, A.; Lomeda, J.; Dimiev, A.; Price, K.; Tour, J. Longitudinal unzipping of carbon nanotubes to form graphene Nanoribbons. *Nature,* **2009**, *458*, 872-876.

32. Eda, G.; Fanchini, G.; Chhowalla, M. Large-area ultrathin films of reduced graphene oxide as a transparent and flexible electronic material. *Nat. Nanotechnol.,* **2008**, *3*, 270-274.

33. Gomez-Navarro, C.; Meyers, J. C.; Sundaram, R. S.; Chuvilin, A.; Kurash, S.; Burghard, M.; Kern, K.; Kaizer, U. Atomic Structure of Reduced Graphene Oxide. *Nano Lett*., **2010**, *10*, 1144-1148.

34. Higginbotham, A.; Kosynkin, D.; Sinitskii, A.; Sun, Z.; Tour, J. M. Lower-defect graphene oxide nanoribbons from multiwalled carbon nanotubes. *ACS Nano*, **2010**, *4*, 2059-2069.

35. Shen, J.; Hu, Y.; Shi, M.; Lu, X.; Qin, C.; Li, C.; Ye, M. Fast and facile preparation of graphene oxide and reduced graphene oxide nanoplatelets. *Chem. Mat.,* **2009**, *21*, 3514-3520.

36. Gao, W.; Alemany, L.; Ci, L.; Ajayan, P. New insights into the structure and reduction of graphite oxide. *Nat. Chemistry,* **2009**, *1*, 403-408.

37. Cai, W.; Piner, R.; Nguyen, S.; Stadermann, S.; Shaibat, Y.; Yang, D.; Velamakanni, S.; Stoller, M.; An, J.; Chen, D.; Ruoff, R. Synthesis and solid-state NMR structural characterization of ^{13}C-labeled graphite oxide. *Science,* **2008**, *321*, 1815-1817.

38. Stankovich, S.; Piner, R.; Nguyen, S.; Ruoff, R. Synthesis and exfoliation of isocyanate-treated graphene oxide nanoplatelets. *Carbon,* **2004**, *44*, 3342-3347.

39. Aoi, Y.; Ono, K.; Kamijo, E. Preparation of amorphous CNx thin films by pulsed laser deposition using a radio frequency radical beam source. *J. Appl. Phys.,* **1999**, *86*, 2318-2322.

40. Jeong, H.; Lee, Y.; Lahaye, R.; Park, M.; An, K.; Kim, I.; Yang, C.; Park, C.; Ruoff, R.; Lee, Y. Evidence of graphitic AB stacking order of graphite oxides. *J. Am. Chem. Soc*., **2008**, *130*, 1362-1366.

41. Gao, X.; Jang, J.; Nagase, H. Hydrazine and thermal reduction of graphene oxide: reaction mechanisms, product structures, and reaction design. *J. Phys. Chem C,* **2010**, *114*, 832-842.

42. Gilje, S.; Han, S.; Wang, M.; Wang, K. L.; Kaner R. B. A Chemical route to graphene for device applications. *Nano Lett*., **2007**, *7*, 3394-3398.

43. Gómez-Navarro, C.; Weitz, R. T.; Bittner, A. M.; Scolari, M.; Mews, A.; Burghard, M.; Kern, K. Electronic transport properties of individual chemically reduced graphene oxide sheets. *Nano Lett*., **2007**, *7*, 3499-3503.

44. Sinitskii, A.; Fursina, A. A.; Kosynkin, D. V.; Higginbotham, A. L.; Natelson, D.; Tour, J. M. Electronic transport in monolayer graphene nanoribbons produced by chemical unzipping of carbon nanotubes. *Appl. Phys. Lett.,* **2009**, *95*, 253108.

45. Jung, I.; Dikin, D. A.; Piner, R. D.; Ruoff, R. S. Tunable electrical conductivity of individual graphene oxide sheets reduced at low temperatures. *Nano Lett.,* **2008**, *8*, 4283-4287.

46. Sinitskii, A.; Dimiev, A.; Kosynkin, D. V.; Tour, J. M. Graphene nanoribbon devices produced by oxidative unzipping of carbon nanotubes. *ACS Nano,* **2010**, *4*, 5405-5413.

47. Sinitskii, A.; Dimiev, A.; Corley, D. A.; Fursina, A. A.; Kosynkin, D. V.; Tour, J. M. Kinetics of diazonium functionalization of chemically converted graphene nanoribbons. *ACS Nano,* **2010**, *4*, 1949-1954.

48. Schedin, F.; Geim, A. K.; Morozov, S. V.; Hill, E. W.; Blake, P.; Katsnelson, M. I.; Novoselov, K. S. Detection of individual gas molecules adsorbed on graphene. *Nat. Mater*., **2007**, *6*, 652-655.

5.7. Experimental Contributions

I prepared all the graphene oxide compounds. Also, I characterized the material by UV/Vis, Raman, AFM, FITR-ATR, TGA, and XPS. Solid ^{13}C NMR was obtained by Dr. Alemany, XRD measurements by Wei Lu, TEM images by Dr. Sun, and conductivity measurements by Dr. Sinitskii and Alxander Slesarev. Dr. Berlin and Dr. Kosynkin assisted with the material preparation and data analysis.

Appendix A

The appendix corresponds to the supporting information of Chapter 1

Characterization of the PEG-HCCs

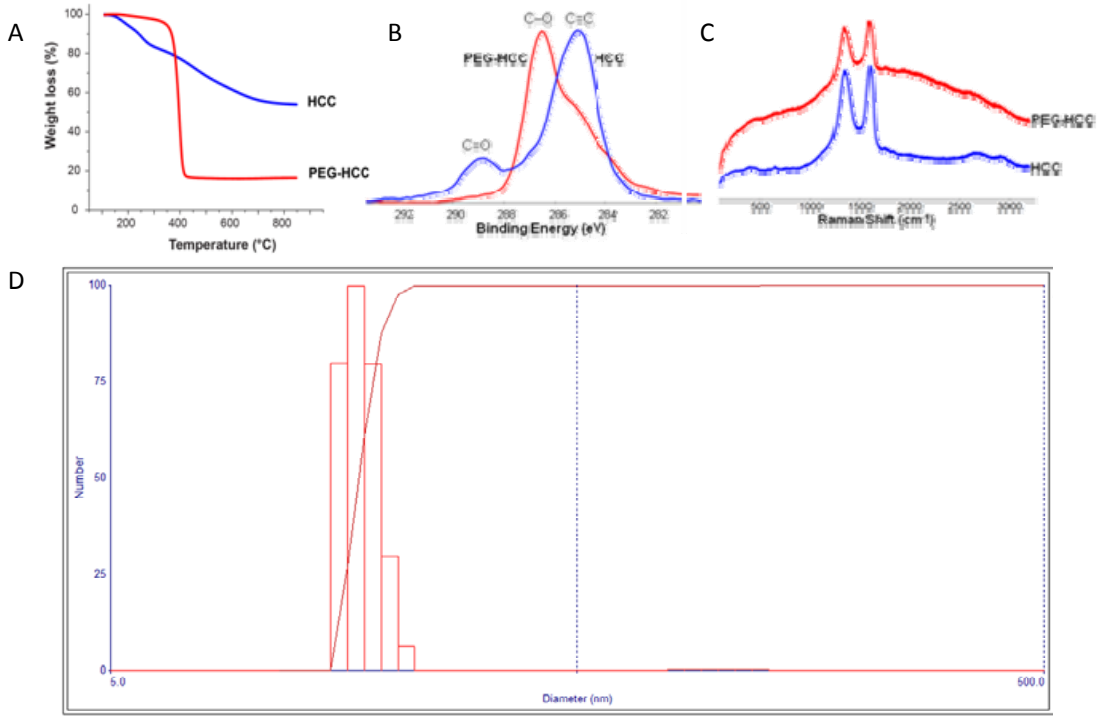

Figure A1. HCC and PEG-HCC characterization by (A) thermogravimetric analysis, (B) X-ray photoelectron spectroscopy, (C) Raman spectroscopy, and (D) dynamic light scattering.

EPR control samples for $O_2^{\bullet-}$ scavenging evaluation

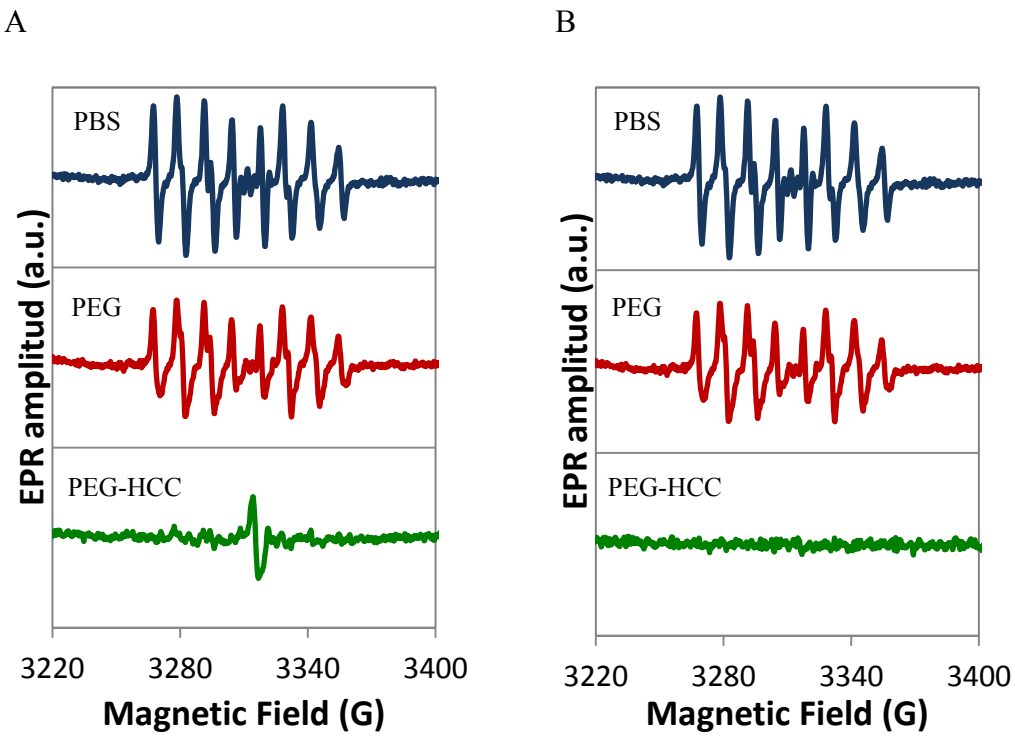

Figure A2. Uncorrected (A) and corrected (B) EPR spectra at pH 7.4 and room temperature corresponding to the $O_2^{\bullet-}$ and $^{\bullet}OH$ experiments. (A) EPR spectra obtained from the $O_2^{\bullet-}$ system or DEPMPO-OOH adduct. Spectra were recorded after 70 s of the KO_2 addition. PEG-HCCs spectrum was corrected by subtracting the signals of the PEG-HCCs alone (Figure 1.1A). (B) EPR spectra obtained from the $^{\bullet}OH$ system or DEPMPO-OH. Spectra were recorded after 90 s of the H_2O_2 addition. No correction was necessary for the $^{\bullet}OH$ scavenging experiments.

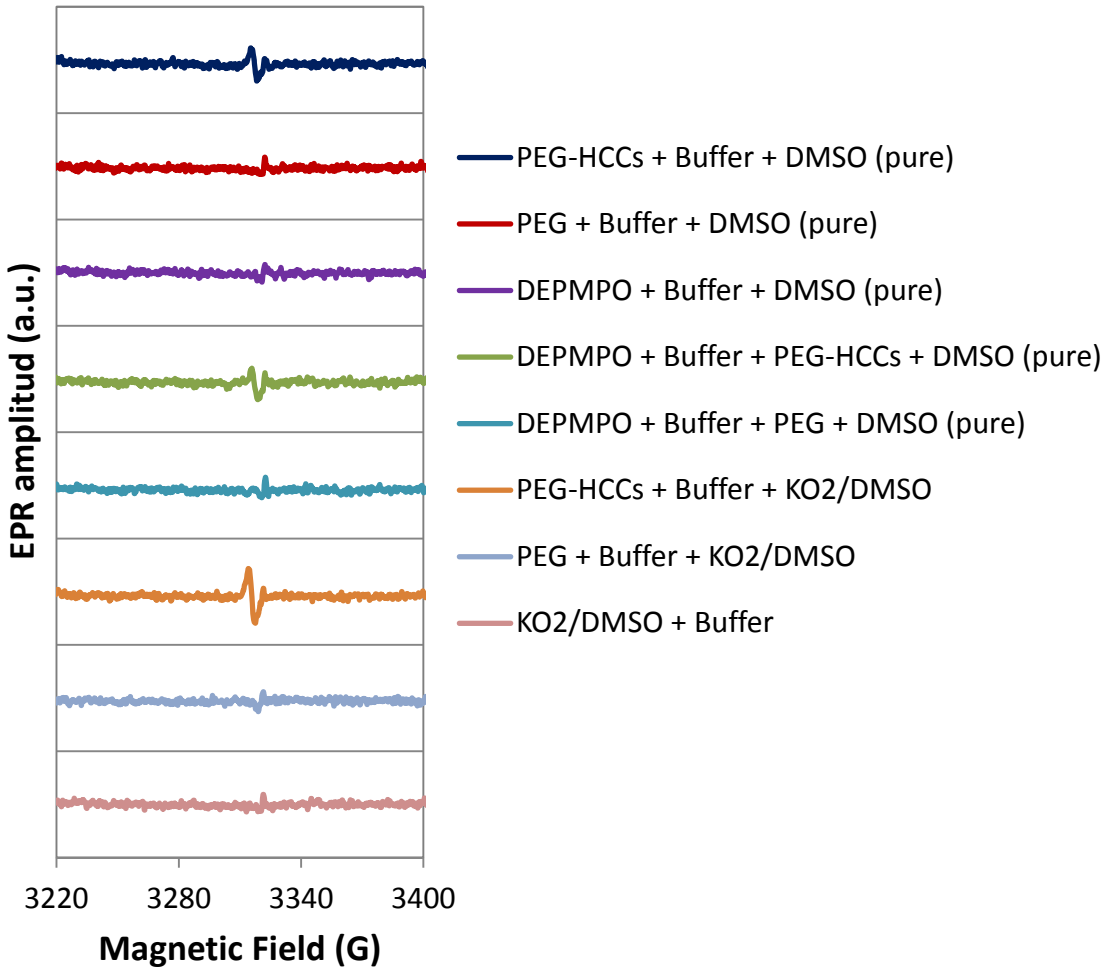

Figure A3. EPR spectra of a set of control samples corresponding to the $O_2^{\bullet-}$ experiments.

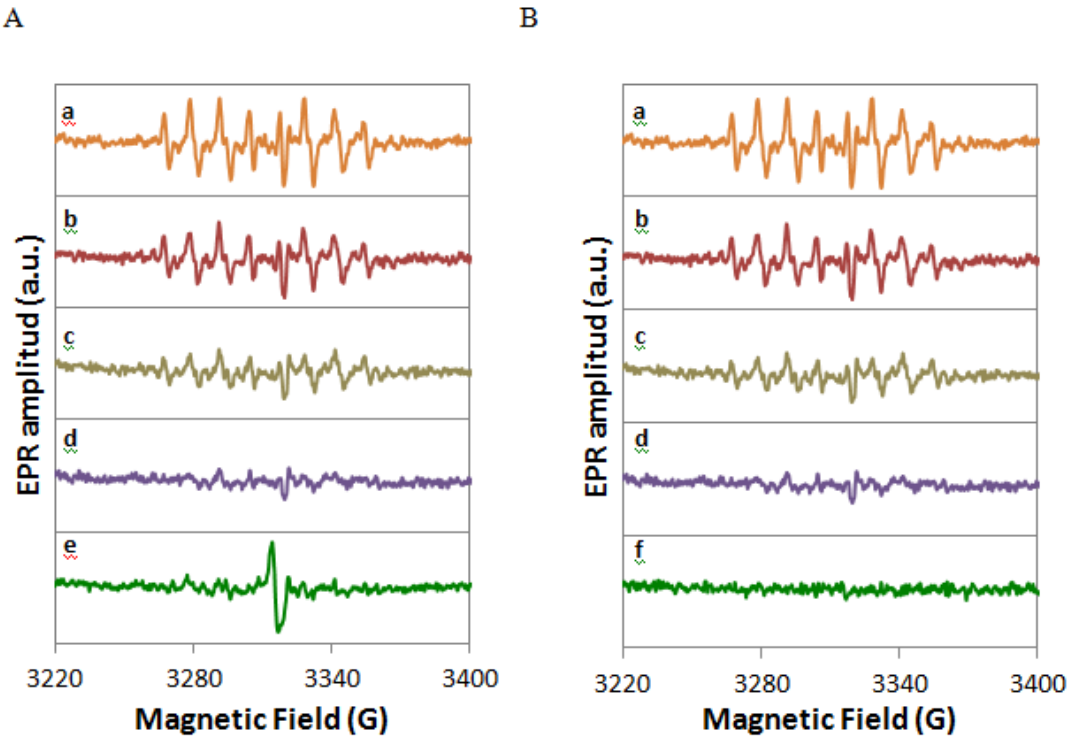

Figure A4. Uncorrected (A) and corrected (B) EPR spectra of the samples treated with SOD instead of the PEG-HCCs. The dismutation of the $O_2^{\bullet-}$ radicals is being catalyzed by SOD causing a signal drop. (A) SOD 0.01 U/mL (B) SOD 0.10 U/mL (C) 1.00 U/mL (D) SOD 10.00 U/mL (E) PEG-HCCs (0.07 mg/mL, which is the same concentration used in Figure 1.1A). Spectrum E was corrected by subtracting the EPR signal of the PEG-HCCs.

Decomposition of the DEPMPO-OH adduct

If the PEG-HCCs are interacting with the DEPMPO-OH after 90 s, the *k* of the adduct decomposition reaction will change. Therefore, the spin-adduct decay was followed for 30 min, using the signal amplitude of the peak localized at 3281.080 G as a reference (Figure A5). The adduct decomposition behaves as a 1st order reaction (Equation A1).

$$-\frac{d[\text{DEPMPO}-\text{OH}]}{dt} = k[\text{DEPMPO}-\text{OH}] \qquad \text{(Equation A1)}$$

$$\ln[\text{DEPMPO}-\text{OH}] = -kt + \ln[\text{DEPMPO}-\text{OH}]_{t_0} \qquad \text{(Equation A2)}$$

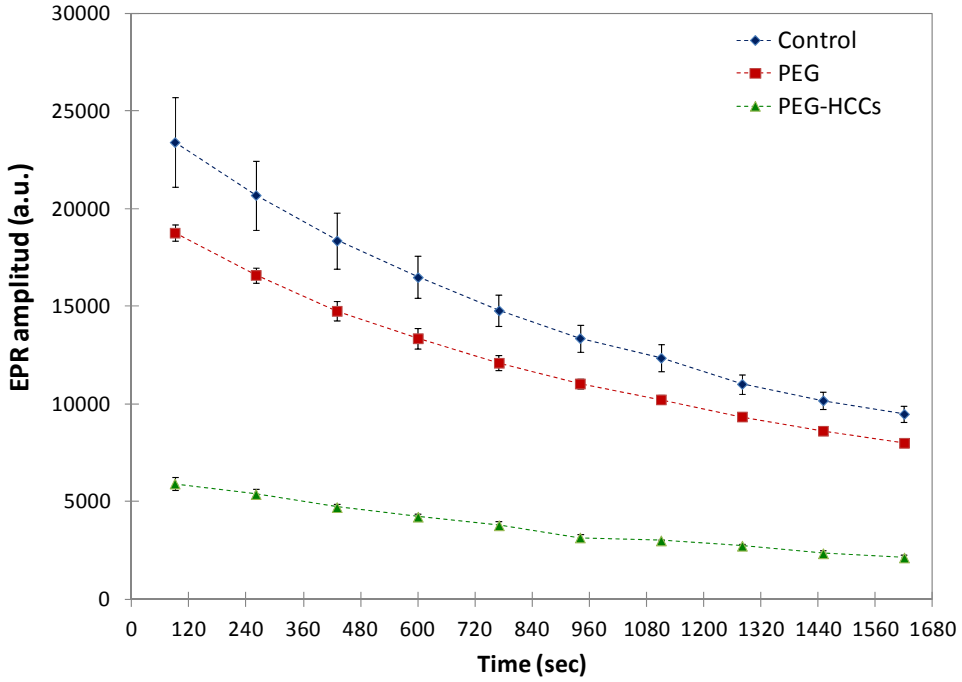

Figure A5. EPR signal decay of the DEPMPO-OH adduct. Each point represents the average of the signal intensities at 3281.080 G corresponding to 3 independent

experiments for Control and PEG-HCCs treatment, and, 2 independent experiments for PEG treatment. Error bars correspond to the standard error (SE).

Figure A6 displays the integrated 1st order curves. (Equation A2). The *k* values obtained were 0.0006, 0.0005, and 0.0007 s^{-1} for the control, PEG, and PEG-HCCs treatment respectively. These values indicate that neither PEG-HCCs nor PEG promote the decomposition of DEPMPO-OH after 90 s.

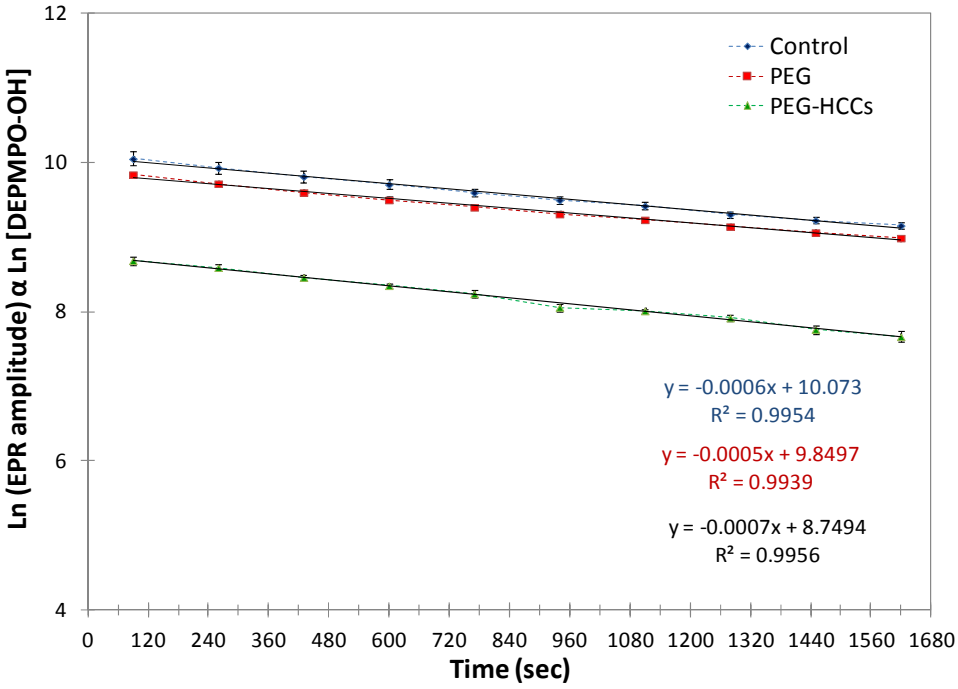

Figure A6. Linear regression corresponding to the 1st order law (Equation A2). The slope of each curve represents –*k*. 3 independent experiments were run for Control and PEG-HCCs treatments and, 2 independent experiments for PEG treatment. Error bars correspond to the standard error (SE).

EPR control samples for $^{\bullet}$OH scavenging evaluation

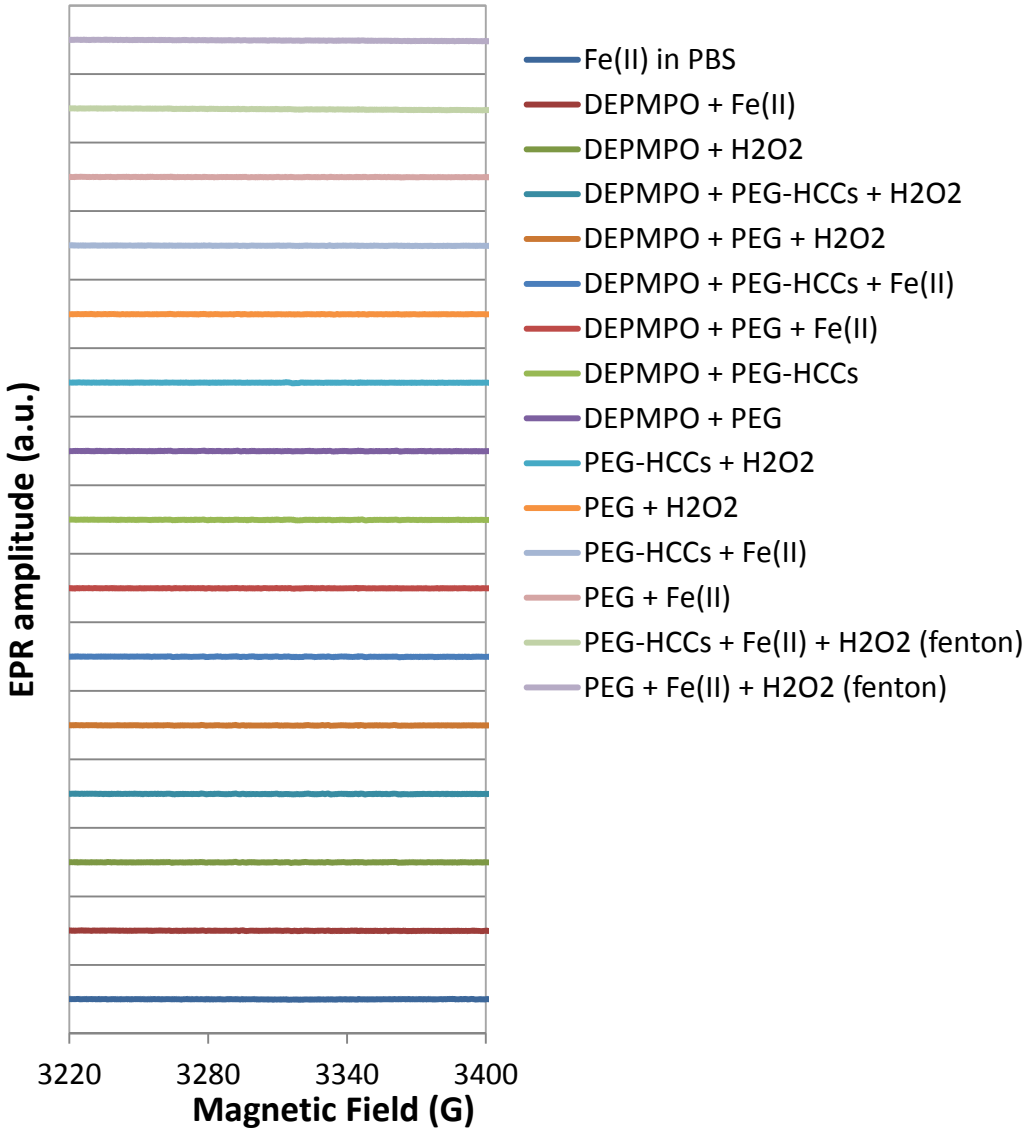

Figure A7. EPR spectra of a set of control samples corresponding to the $^{\bullet}$OH experiments.

Stability of the EPR signal of the PEG-HCCs in different buffers

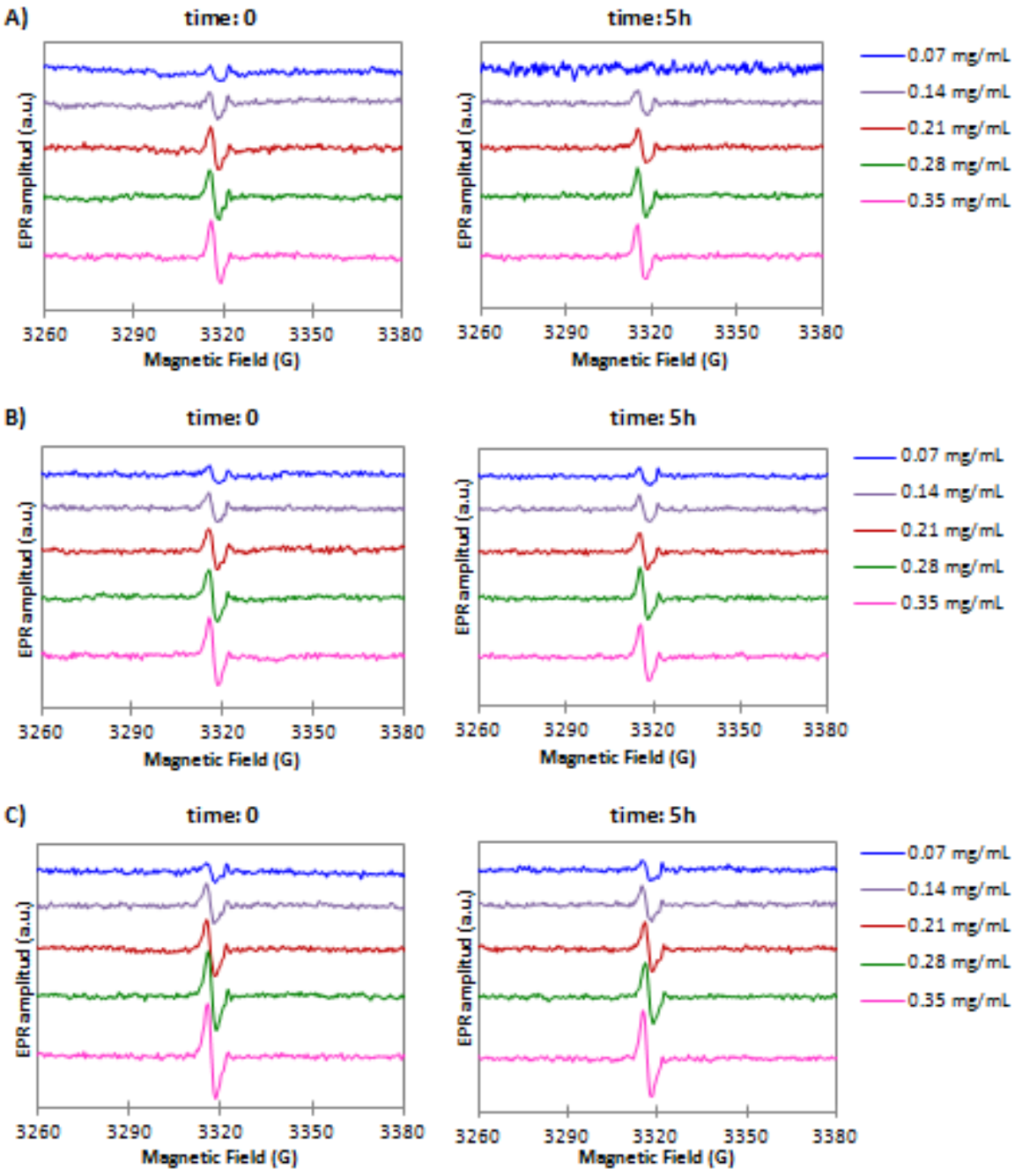

Figure A8. EPR spectra of the PEG-HCCs at different pHs. A) pH 4 (citrate buffer). B) pH 7.4 (PBS). C) pH 9 (borate buffer).

NO• scavenging assay

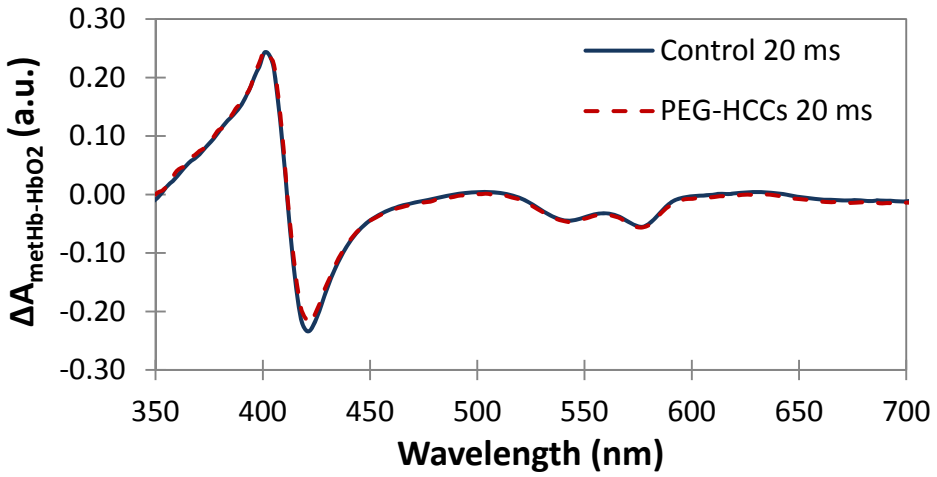

Figure A9. Difference spectrum of metHb and HbO_2 in the absence (blue) and presence of the PEG-HCCs (red) after being incubated with NO• for 20 ms. The difference between the $\Delta A_{401\text{-}411nm}$ values of the control and the $\Delta A_{401\text{-}411nm}$ values of PEG-HCCs treated system is lower than the experimental error. Experiment was carried out in triplicate.

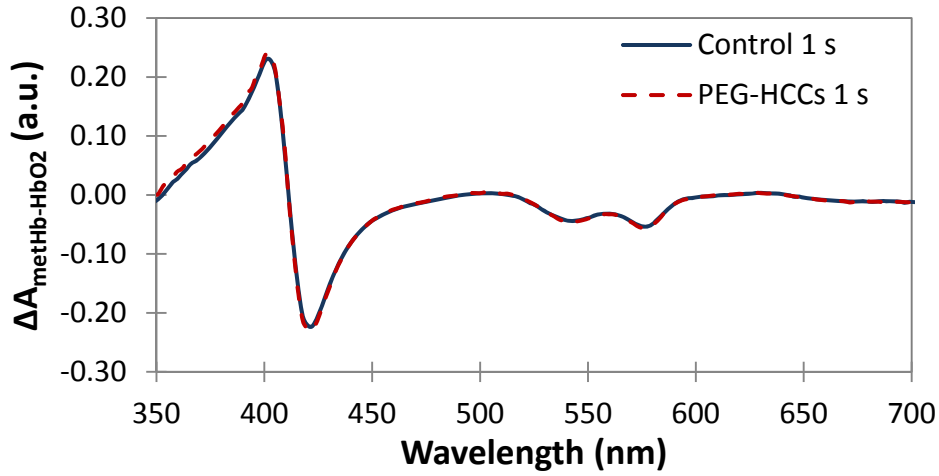

Figure A10. Difference spectrum of metHb and HbO_2 in the absence (blue) and presence of the PEG-HCCs (red) after being incubated with $NO^{\bullet}$ for 1 s. The difference between the $\Delta A_{401\text{-}411nm}$ values of the control and the $\Delta A_{401\text{-}411nm}$ values of PEG-HCCs treated system is lower than the experimental error. Experiment was carried out in triplicate.

Supplementary tables

Table A1. Evaluation of the EPR signals of a set of control samples corresponding to the $O_2^{\bullet-}$ experiments.

Samples	**Observations**
PEG-HCCs + Buffer + DMSO (pure)	PEG-HCCs signal at ~ 3317 G
PEG + Buffer + DMSO (pure)	-
DEPMPO + Buffer + DMSO (pure)	-
DEPMPO + Buffer + PEG-HCCs + DMSO (pure)	PEG-HCCs signal at ~ 3317 G (higher intensity)
DEPMPO + Buffer + PEG + DMSO (pure)	-
PEG-HCCs + Buffer + KO_2/DMSO	PEG-HCCs signal at ~ 3315 G
PEG + Buffer + KO_2/DMSO	-
KO_2/DMSO + Buffer	-

Table A2. Evaluation of the EPR signals of a set of control samples corresponding to the $^{\bullet}OH$ experiments.

Samples	**Observations**
Fe^{+2} in PBS	No signal
DEPMPO + Fe^{+2}	No signal
DEPMPO + H_2O_2	No signal
DEPMPO	No signal
DEPMPO + PEG-HCCs + H_2O_2	No signal
DEPMPO + PEG + H_2O_2	No signal
DEPMPO + PEG-HCCs + Fe^{+2}	No signal
DEPMPO + PEG + Fe^{+2}	No signal
DEPMPO + PEG-HCCs	No signal
DEPMPO + PEG	No signal
PEG-HCCs + H_2O_2	Depreciable (3312-3320 G)
PEG + H_2O_2	No signal
PEG-HCCs + Fe^{+2}	No signal

PEG + Fe^{+2}	No signal
PEG-HCCs + Fe^{+2} + H_2O_2 (nanoparticle + Fenton rxn)	No signal
PEG + Fe^{+2} + H_2O_2 (polymer + Fenton rxn)	No signal

Appendix B

The entirely appendix was copied from the supporting information of reference #1 of this section (Chapter 2)

Protection of b.End3 Cells from Oxidative Stress-Induced Death - Intracellular Superoxide Cell Culture Model

bEnd.3 cells (~200,000/well, passaged less than 10 times) were plated in 6-well plates. To each well was added 2 ml of ATCC complete growth medium (Dulbecco's modified Eagle's medium with 4 mM L-glutamine adjusted to contain 1.5 g/l sodium bicarbonate and 4.5 g/l glucose, 90%; fetal bovine serum, 10%). Cells were incubated at 37 °C with 5% CO_2 for 72 h. Media was removed and replaced with 1 ml fresh media. Cells were then treated with 15 μl/well 3mM Antimycin A or 1 × PBS. This dose was selected empirically to provide a midrange toxicity of the bEnd.3 cells. Cells were incubated at 37 °C with 5% CO_2 for 10 min then one of the following was added: 40 μl/well of 100 mg/l PEG-HCCs, or 40 U/well PEG-SOD. Cells were then incubated at 37 °C with 5% CO_2 for 24 h. Cells were washed twice with 1 × PBS, removed from wells with 0.5 ml trypsin, suspended in 2 ml PBS with 2% fetal calf serum, and washed twice. Cells were resuspended in 0.5 ml 1 × PBS and counted on a Vi-Cell XR Analyzer (Beckman Coulter, Brea, CA). Viable cells/ml was recorded and the percent relative to control was calculated from the PBS-treated control cells.

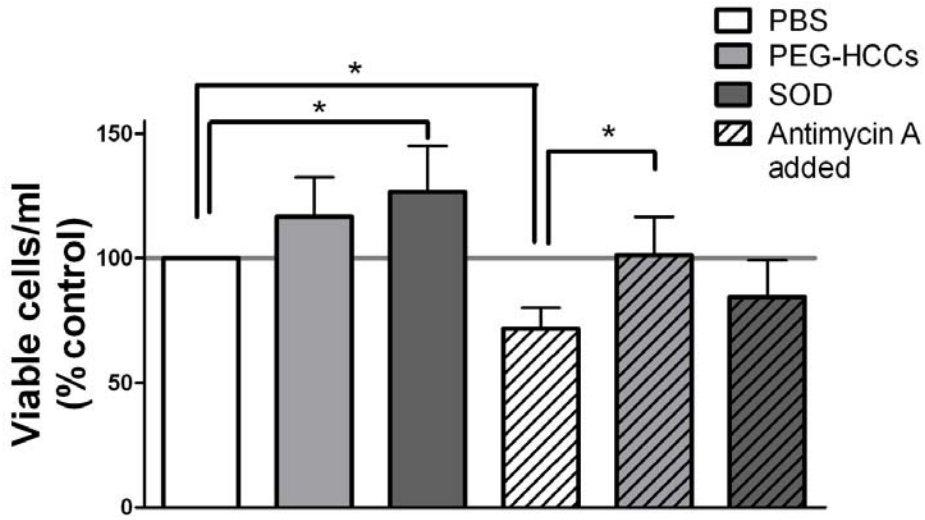

Figure B1. Cell survival with antioxidant treatment. Antimycin A was used to induce cell death (~30% mortality) in bEnd.3 cells. Cells were then treated with PEG-HCCs or the known antioxidant PEG-SOD (SOD). After 24 hours, cell survival was determined with a trypan blue assay and the antimycin A-treated cells (striped bars) were compared to cells not stressed with Antimycin A (solid bars). * p-value <0.05.

ORAC assay

The antioxidant capacity of the PEG-HCCs was compared by ORAC to known antioxidants vitamin C, caffeic acid, and catechin. The linear relationship between the net area and antioxidant concentration was evaluated by using a set of trolox and PEG-HCCs standards (Figures B2- B4). Table B1 summarizes the correlation coefficient, slope, and intercept of the trolox standard curves obtained in each run. The assay was consistent for all concentrations tested. For comparison and TME calculations, the concentrations of

vitamin C, caffeic acid, catechin, trolox, and PEG-HCCs were kept constant at 1.6 µg/mL (Figure 3A, Table B2).

Table B1. Summary of Trolox Calibration curve for each run related to known antioxidants evaluation $\boldsymbol{Y}(Net.\ AUC) = a + b\ \boldsymbol{X}(mg/mL)$. Accepted R^2 >0.9900. Slope and intercept errors calculated at 95% confidence.

Run	R^2	Slope (*b*)	Intercept (*a*)	Observations
1	0.9982	424.9 ± 18.1	0.677 ± 0.599	3 standards
2	0.9991	399.9 ± 12.1	-0.325 ± 0.399	3 standards
3	0.9991	431.0 ± 32.5	3.364 ± 0.439	3 standards
4	0.9998	387.1 ± 5.4	2.980 ± 0.179	3 standards
Average	**0.9990**	**410.7 ± 20.7**	**1.674 ± 1.784**	

Table B2. TME corresponding to the known antioxidants evaluation. The concentration of each compound was the same 1.6µg/mL. Quality control samples were also run for each set indicating a (%RSD) of 35% and (%REC) of 95%.

Run	Vitamin C	Caffeic Acid	Catechin	Trolox	PEG-HCCs
1	1.02	7.04	5.68	1.00	2.96
2	0.78	9.68	7.58	1.00	3.73
3	0.30	5.38	4.25	1.00	2.07

4	0.22	6.43	4.78	1.00	2.24
Average	**0.58**	**7.13**	**5.57**	**1.00**	**2.75**
SD	0.38	1.83	1.46	n.a	0.76
SE	0.19	0.92	0.73	n.a	0.38

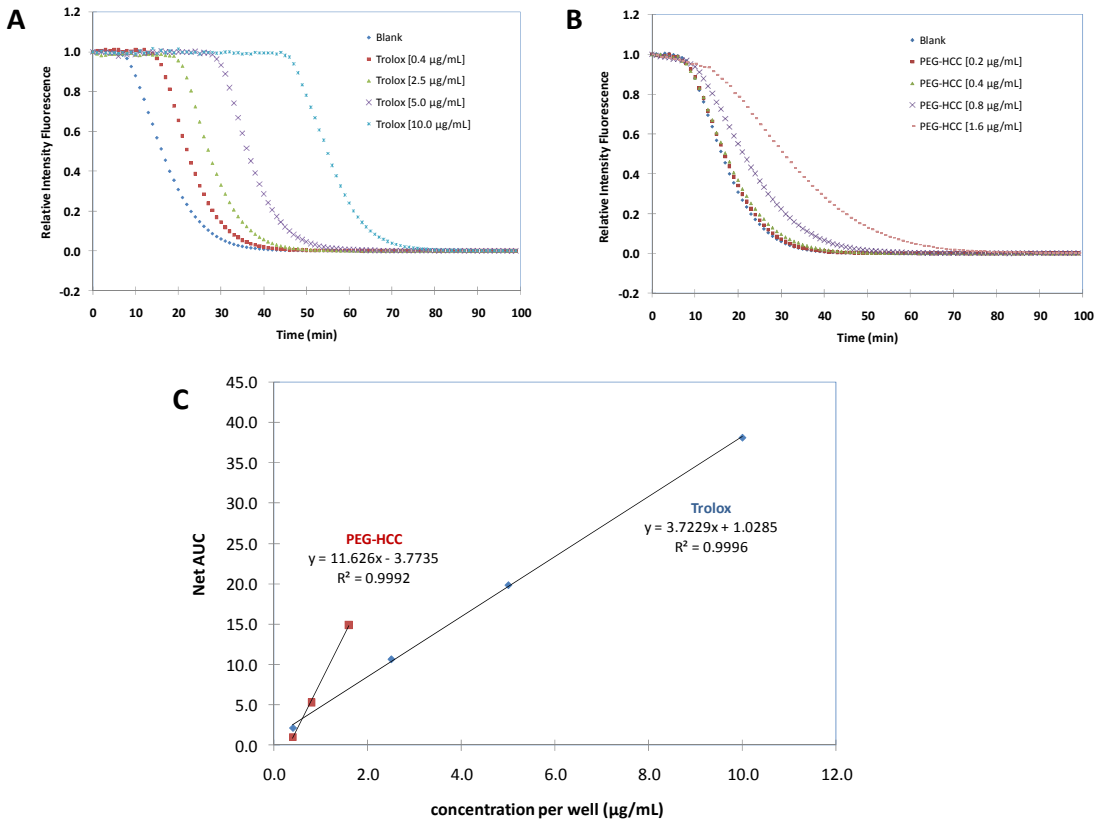

Figure B2. Fluorescence decay and calibration curves. (A) Trolox concentration effect on fluorescence decay curve induced by AAPH. (B) PEG-HCCs concentration effect on fluorescence decay curve after AAPH addition. (C) Liner regression of Net AUC of trolox and PEG-HCC. An approximation of the Trolox mass equivalent can be estimated dividing the slope of the sample by the trolox slope ($TME_{PEG\text{-}HCC}$ = 3.12)

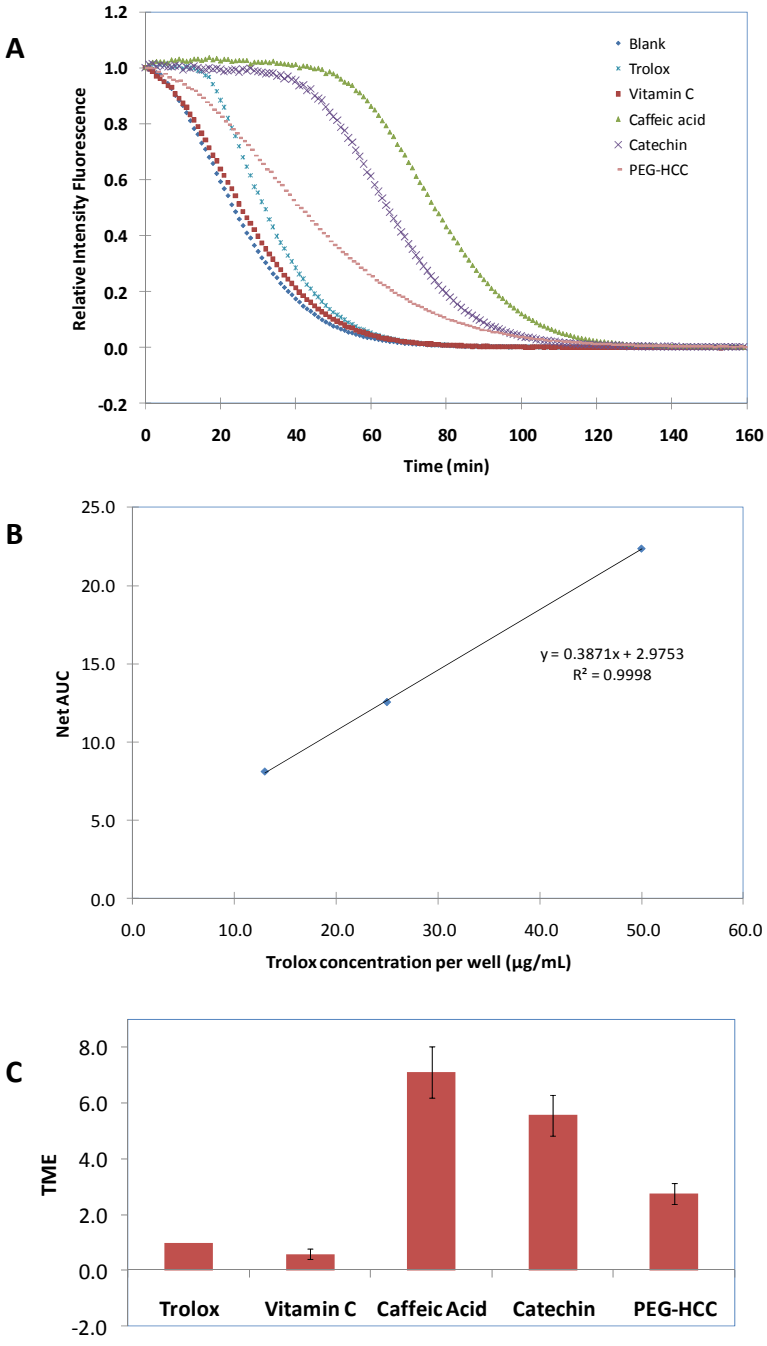

Figure B3. Typical fluorescence decay and calibration curves obtained from different antioxidants. (A) Fluorescence decay curve obtained during the vitamin C, caffeic acid, catechin, and PEG-HCC evaluation. (B) Liner regression of Net AUC of trolox corresponding to the decay curve A. (C) Curve C represents the TME values

corresponding to the different knownantioxidants and carbon nanoparticles respectively. Trolox is the reference compound (TME_{trolox}=1).

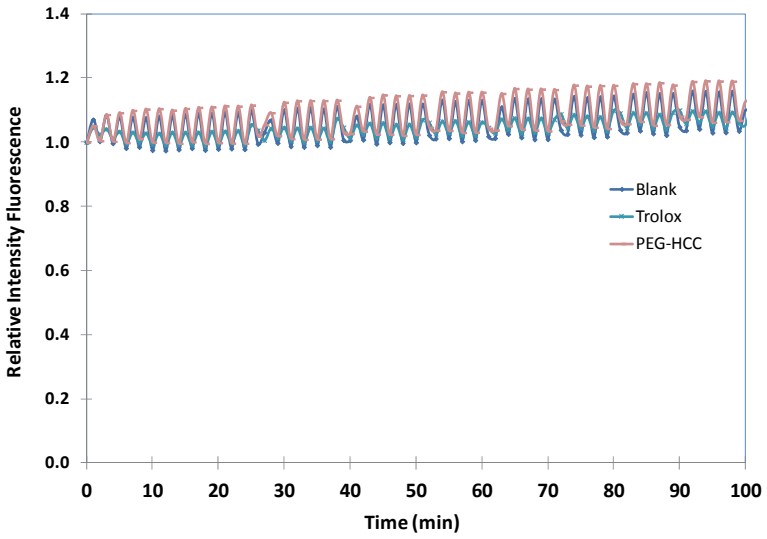

Figure B4. Typical fluorescence curves obtained when PBS, Trolox, PEG-HCCs, and the fluorescent probe were not mixed with AAPH (control 1). Note that fluorescent intensity remained stable during the experiment and the intensity is not affected by the nanoparticles.

References

1. Marcano, D. C.; Bitner, B. R.; Berlin, J. M.; Jarjour, J.; Lee, J. M.; Jacob, A.; Fabian, R. H.; Kent, T. A.; Tour, J. M. Design of poly(ethylene glycol)-functionalized hydrophilic carbon clusters for targeted therapy of cerebrovascular dysfunction in mild traumatic brain injury. *J. Neurotrauma*, **2012**, accepted.

Appendix C

The entirely appendix was copied from the supporting information of reference #1 of this section (Chapter 3)

Supplementary figures

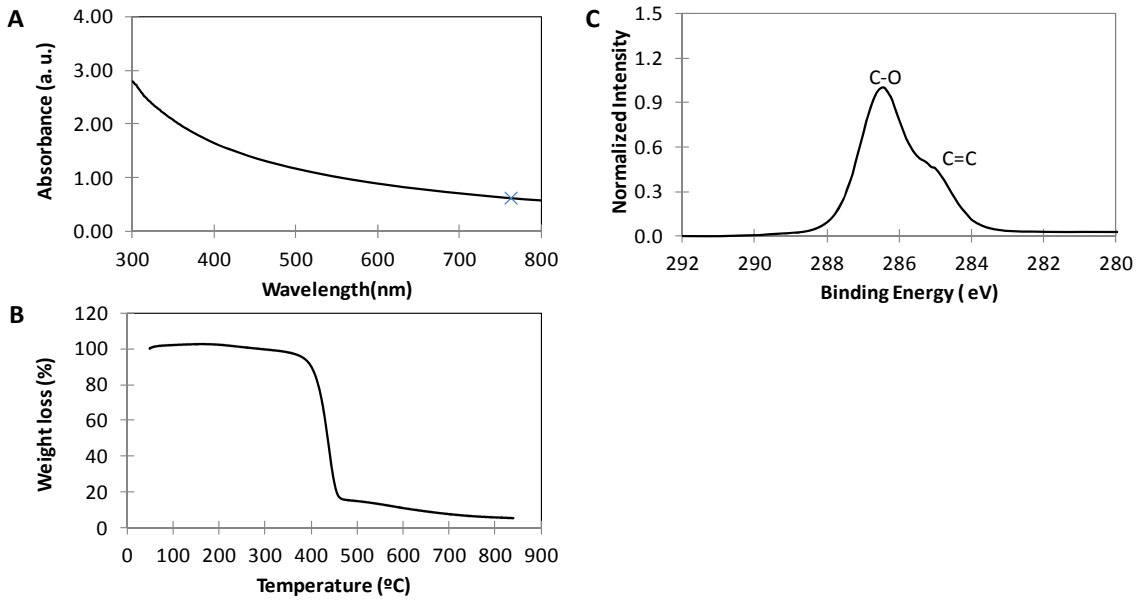

Figure C1. Characterization of the PEG-HCCs. (A) UV- spectrum of the PEG-HCCs in water. Concentration of the particles is estimated based on the carbon core absorbance at 763 nm using ε = 0.01040 mL/µg (indicated with a X).This wavelength is not used for biological assays. (B) TGA shows a 95% weight loss (50 – 850 ºC at 10 ºC/min rate under Ar). The pronounced weight loss around 400 ºC (84%) corresponds to the C-O functionalities of the PEG. (C) XPS spectrum of C(1s) reflects the signal corresponding

to C=C at 284.5 eV as well as the strong signal corresponding to the C-O functionalization at 286.0 eV related to the PEG chains.

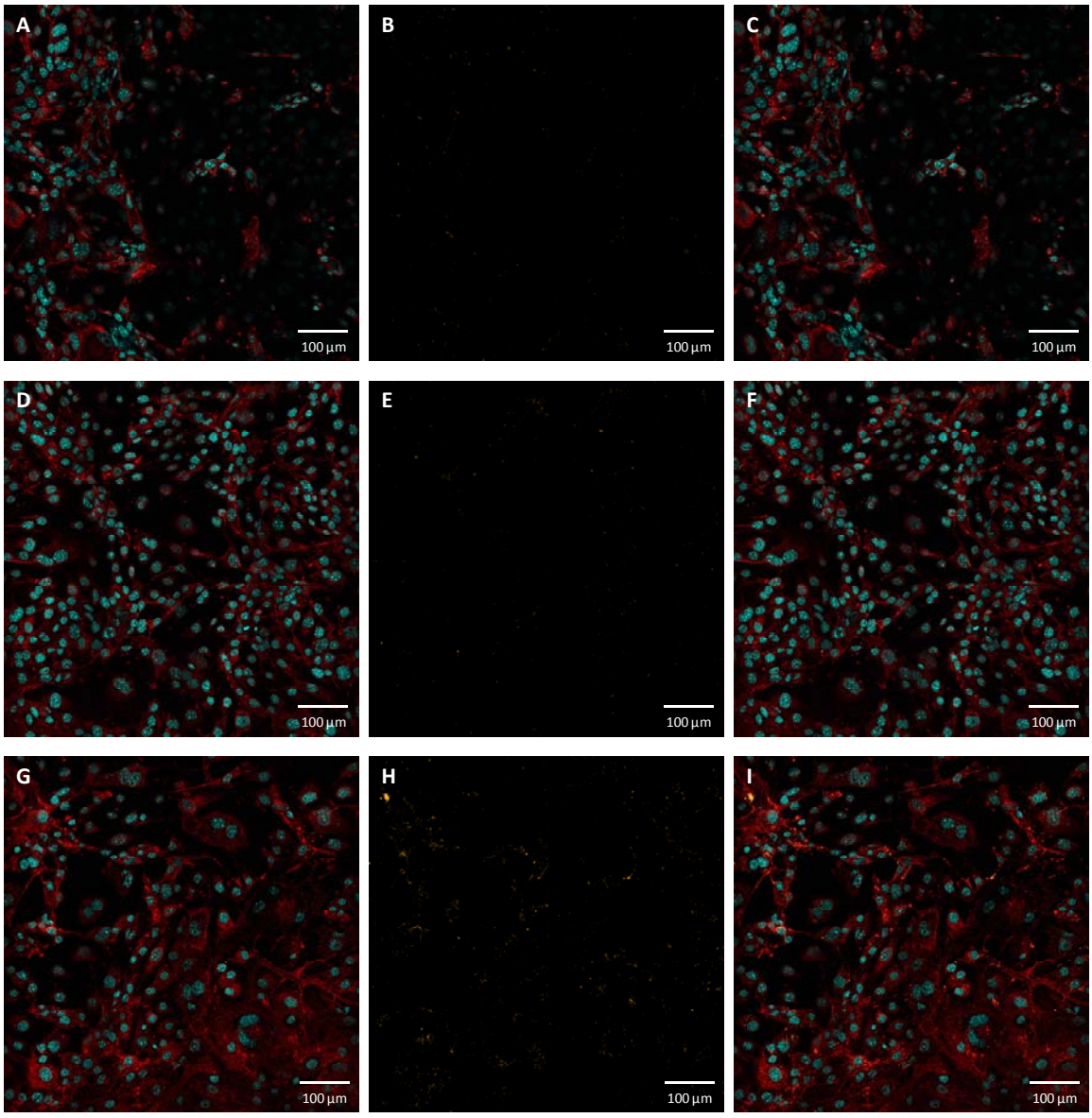

Figure C2. Images of mock, PEG and PEG-HCC-treated b.End.3 cells. Cell nuclei were stained with DAPI (blue), cell membranes with Wheat Germ Agglutinin 594 (red), and PEG and PEG-HCCs were stained using a primary antibody against PEG with an Alexa-

633 conjugated secondary antibody (orange). Each set of images was taken with the same settings on a Zeiss LSM 510 confocal microscope, and are shown at the same brightness/contrast levels. (A) The membrane and nuclei stained cells, (B) PEG-stained, and (C) the overlapped images of the mock treated cells. (D) The membrane and nuclei stained cells, (E) PEG-stained, and (F) overlapped images of the PEG-treated cells. (G) The membrane and nuclei stained cells, (H) PEG-stained, and (I) overlapped images of the PEG-HCC-treated cells. When PEG-HCC-treated cells were stained with the secondary antibody only, no signal was observed indicating that there is no non-specific antibody staining.

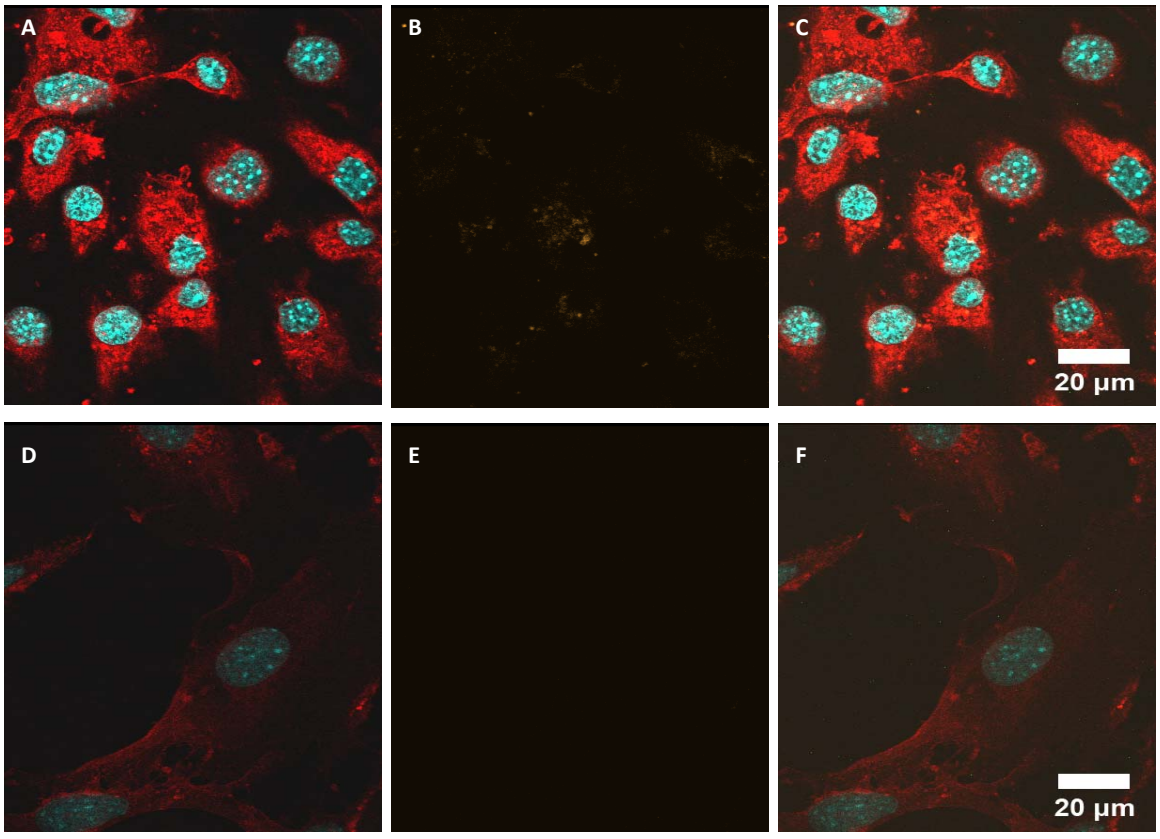

Figure C3. High resolution images of PEG-HCC-treated and PEG b.End.3 cells. Cell nuclei were stained with DAPI (blue), cell membranes with Wheat Germ Agglutinin 594 (red), and PEG and PEG-HCCs were stained using a primary antibody against PEG with an Alexa-633 conjugated secondary antibody (orange). Each set of images were taken with the same settings on a Zeiss LSM 510 confocal microscope, and are shown at the same brightness/contrast levels. (A) The membrane and nuclei-stained cells, (B) PEG-stained, and (C) overlapped images of the PEG-HCC-treated cells. (D) The membrane and nuclei stained cells, (E) PEG-stained, and (F) overlapped images of the PEG-treated cells.

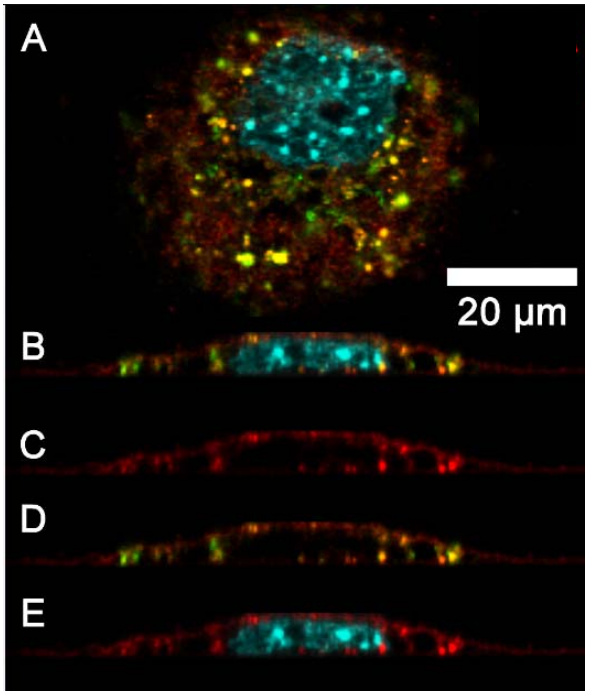

Figure C4. Fine optical sectioning and orthogonal rendering of z-stacks is required in order to resolve the cytoplasm from the cell membrane, which is stained with Wheat

Germ Agglutinin (WGA) 594 (red). Shown in (A) is a section through a cell stained with WGA (red), DAPI (blue), and an antibody against PEG to visualize the internalized PEG-HCCs (green). Panels (B) through (E) show an orthogonal slice through the same cell shown in (A), with the following stains: (B) WGA (red), DAPI (blue), and PEG (green); (C) WGA (red); (D) WGA (red) and PEG (green); (E) WGA (red) and DAPI (blue). Visualizing the cell in this way verifies that the WGA staining is specific to the membrane, and that the PEG-HCCs are located intracellularly.

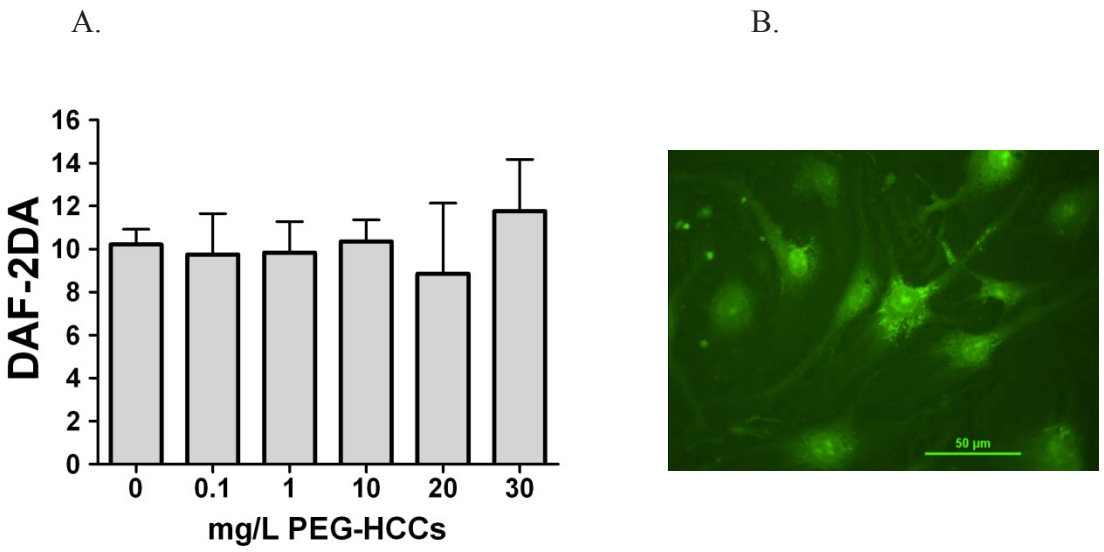

Figure C5. DAF-2DA intensity in bEnd.3 cells that spontaneously generate NO after treatment with increasing concentrations of PEG-HCCs. DAF-2DA is a NO sensitive dye. (A) Concentrations of PEG-HCCs up to 30 mg/L did not quench NO dye fluorescence ($p>.05$ for all comparisons). (B) Fluorescent microscope image of bEnd.3 cells with DAF-2DA. Error bars are s.e.m. Scale bar is 50 µm . Statistics are described in Supplementary Methods section.

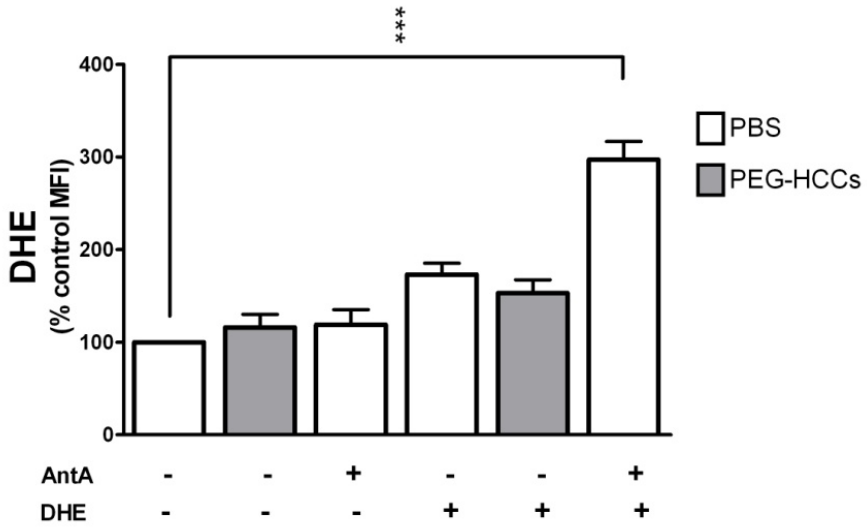

Figure C6. Controls for intracellular SO assay to determine whether there is direct interference between the PEG-HCCs and the fluorescent assay. Cells were treated with or without antimycin A (a mitochondrial toxin that induces SO production). PEG-HCCs were added 15 min later (grey bars) followed by DHE (SO-specific dye) where indicated by +. There was no reduction in either non-specific fluorescence (first three bars) or background fluorescence after addition of DHE (bars 4 and 5). The last combination (bar 6), DHE and antimycin A-treated cells demonstrated, as expected, a significantly higher DHE staining compared to the untreated control (first bar). Statistics are the same as Figure 3.2 and error bars are s.e.m. Means are the results of a minimum of 5 separate experiments.

A.

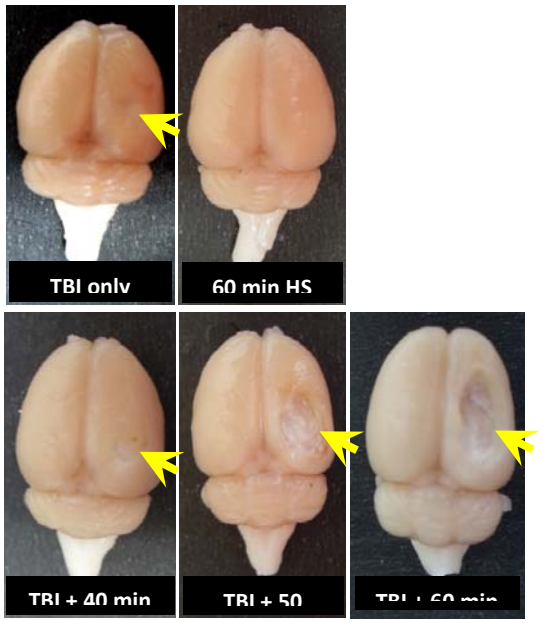
TBI only
60 min HS
TBI + 40 min
TBI + 50

B.

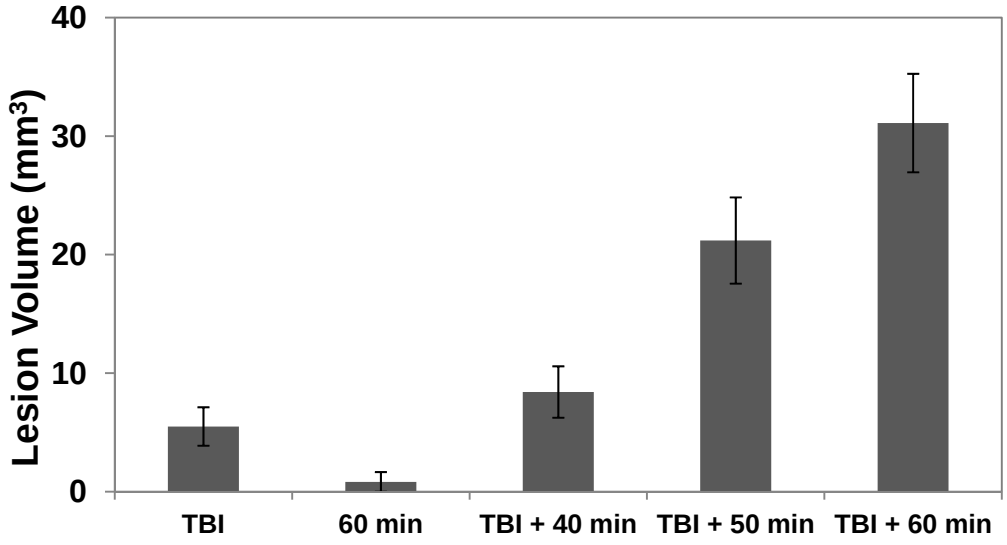
Lesion Volume (mm³)
40
30
20
10
0
TBI
60 min
TBI + 40 min
TBI + 50 min
TBI + 60 min

C.

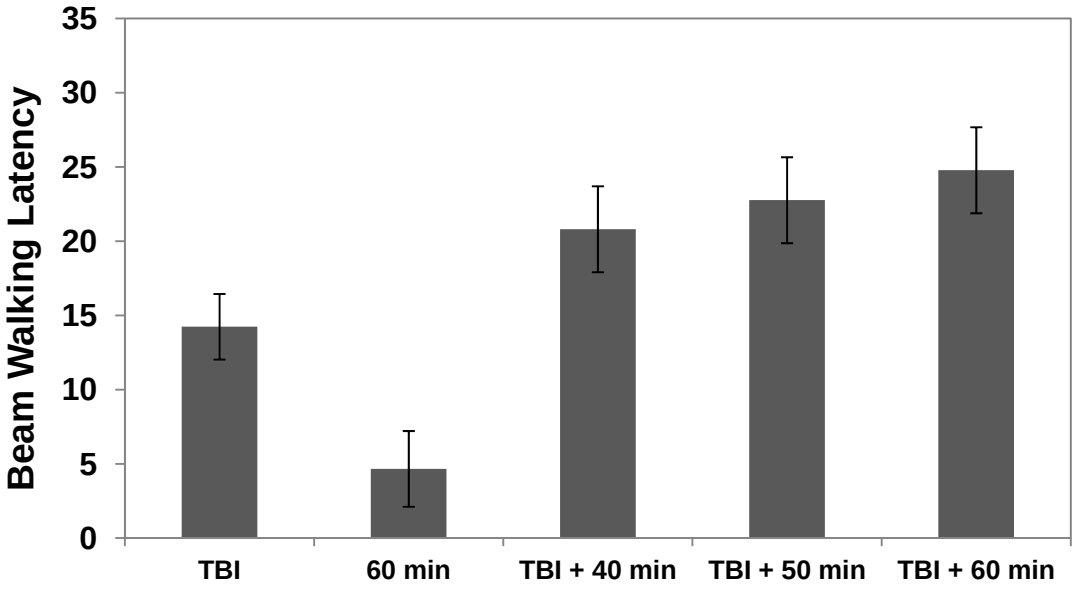

Figure C7. Histological and behavioral evidence that the combination of TBI and hypotension worsens outcome. (A, B) The large change in lesion volume (noted with yellow arrows in A) if TBI is associated with hypotension for 40, 50 and 60 min; recorded 14 days post TBI/ hypotension. (C) The decline of behavioral abilities tracks with increased duration of hypotension. Reproduced from ref 30 of main paper.

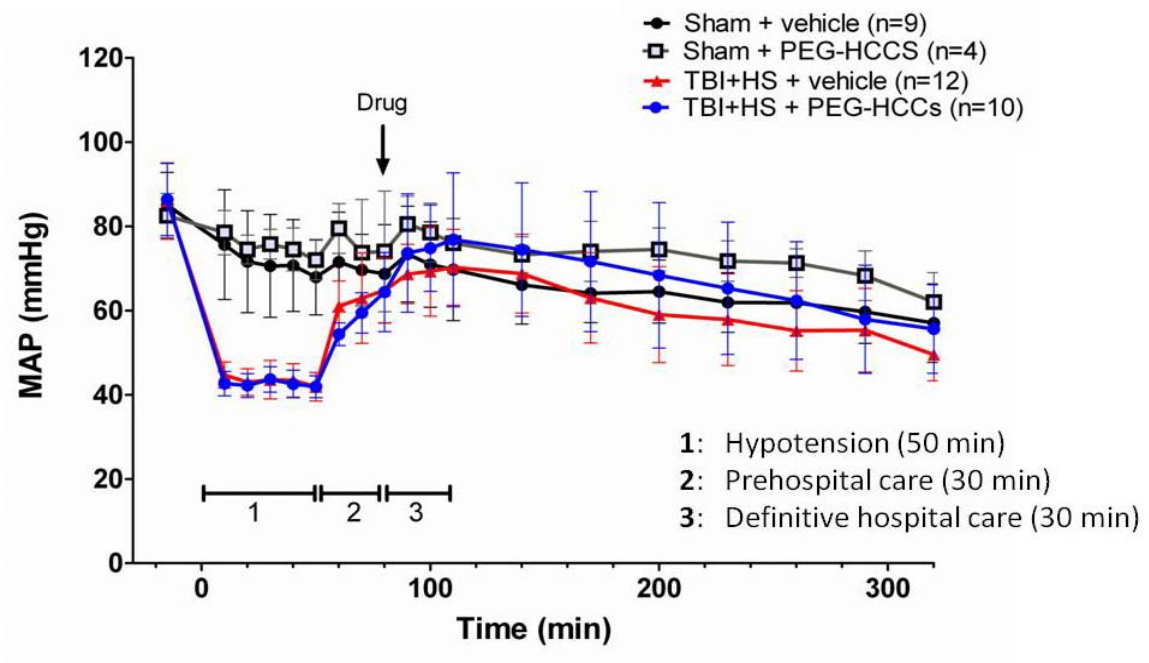

Figure C8. MAP for rats undergoing sham surgery or TBI and hemorrhagic shock (TBI + HS). Drugs (PEG-HCC or PBS vehicle) were given where indicated. Time 0 min indicates when the TBI was performed. Phase 1 = TBI + hypotension; Phase 2 = PBS during "prehopital-ambulance phase"; Phase 3 = blood reinfusion during "definitive-hospital phase". No statistical differences (p-value >0.05) seen with data calculated with repeated measures; ANOVA with Bonferroni post-test. Error bars are s.e.m.

Supplementary tables

Table C1. TBI impact characteristics and rat weights

Mean ± SD	Vehicle	PEG-HCCs	p -value
Rat weight (grams)	287.1 ± 27.0	279.0 ± 16.0	0.3955
Impact characteristics			
Velocity (m/s)	3.29 ± 0.41	3.25 ± 0.49	0.8388
Duration (ms)	79.0 ± 8.9	80.8 ± 5.7	0.5733

Statistics: Repeated measures ANOVA

Table C2. Arterial blood gases in the TBI and hypotension model at baseline, end of hypotension and during the hospital phase.

Arterial blood gases (mean ± SD)		Vehicle	PEG-HCCs	p -value
Baseline	pH	7.44 ± 0.06	7.45 ± 0.07	0.775
	pCO_2	41.46 ± 4.07	39.08 ± 7.4	0.8425
	pO_2	300.9 ± 80.7	309.5 ± 87.6	0.9144
Hypotension	pH	7.39 ± 0.01	7.30 ± 0.05	
	pCO_2	41.85 ± 1.06	47.83 ± 4.99	
	pO_2	139.1 ± 48.7	101.2 ± 36.4	

Hospital	pH	7.29 ± 0.11	7.40 ± 0.09
	pCO_2	41.77 ± 1.99	37.73 ± 9.44
	pO_2	249. 9 ± 100.3	295.9 ± 85.7

pCO_2 is the partial pressure of CO_2
pO_2 is the partial pressure of O_2
Statistics: Repeated measures ANOVA

References

1. Bitner, B. R.; Marcano, D. C.; Berlin, J. M.; Fabian, R. H.; Cherian, L.; Culver, J. C.; Dickinson, M. E.; Robertson, C. S.; Pautler, R. G.; Kent, T. A.; Tour, J. M. Antioxidant carbon particles improve cerebrovascular dysfunction following traumatic brain injury. *ACS Nano*, **2012**, accepted.

Appendix D

The entirely appendix was copied from the supporting information of reference #1 of this section (Chapter 4)

Supplementary figures

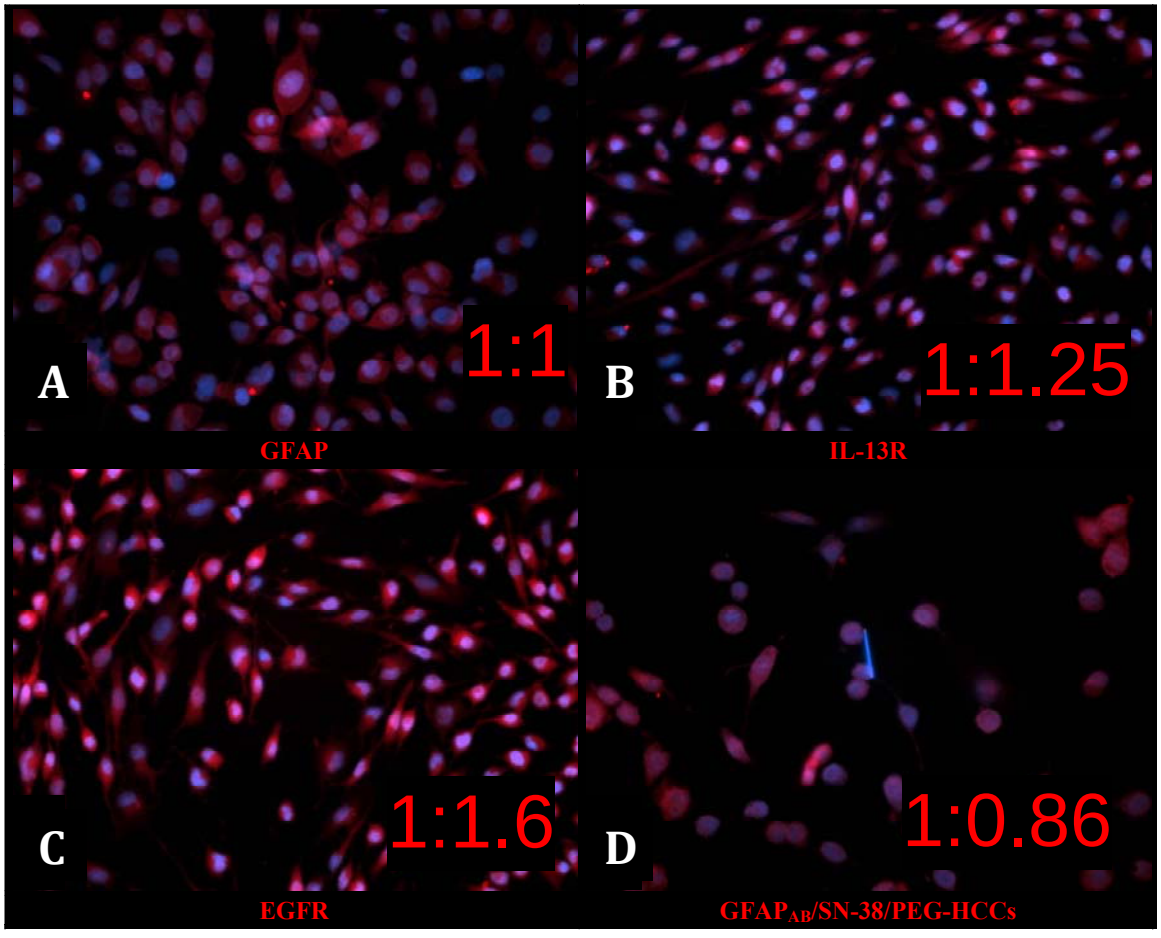

Figure D1. Antigenic mapping of GBM cultures can be used to determine the levels of surface antigens allowing IgG selection for optimization of hydrophilic carbon cluster antibody enhancement system (HADES) anti-cancer therapy. Three control cultures of

GBM with Hoechst prior to fixation in paraformaldehyde (PFA). The washed cells/blocked cells were initially incubated with monoclonal antibodies to (**a**) GFAP, (**b**) IL-13R and (**c**) EGFR and then with a red fluorescently labeled anti-mouse antibody. The ratios of red fluorescence, per cell, are indicated in the red text. The final panel (**d**) shows the binding of $GFAP_{AB}$/SN-38/PEG-HCCs to these cells. This panel shows that anti-GFAP IgG adsorbed to PEG-HCCs are co-localized with the GBM cell surface, after 1 h incubation, as in (**a**). We used the same conditions as used in Figure 4.2, with 5 μM SN-38 as GFAPAB/SN-38/PEG-HCCs, with cells fixed after 1 h incubation and then labeled with a secondary. All figures are at 20× magnification. All figures are at 20× magnification.

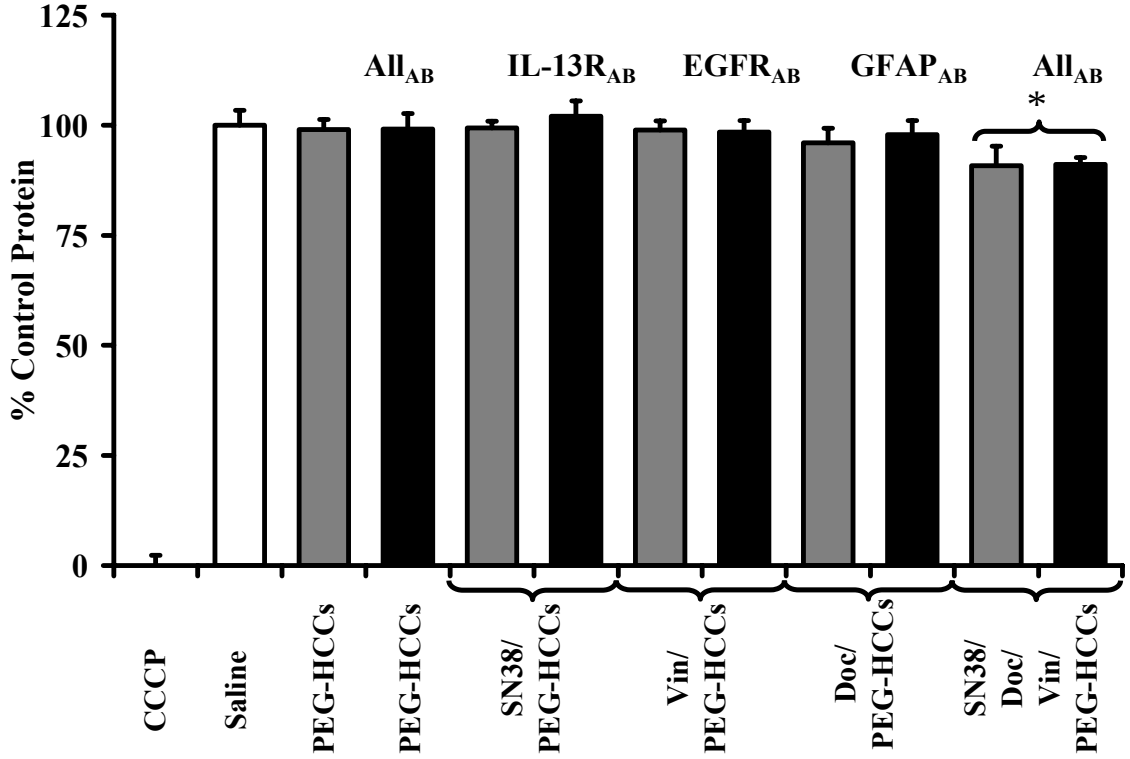

Figure D2. The effects of 24 h treatments of HADES and trident therapy treatments in HCN, measured using the bicinchoninic acid (BCA) protein method. On the left are four HCN controls: 100 µM carbonyl cyanide *m*-chlorophenyl hydrazone (CCCP) (100% cell death), saline vehicle, PEG-HCCs and IgG/PEG-HCCs using monoclonal antibodies toward GFAP, IL-13R or EGFR.. Three HADES treatments are then shown where PEG-HCCs loaded with the drugs Vin, Doc, or SN-38 were added to HCN without antibodies (black) or with antibodies (gray). The final pairing shows that trident therapy without antibodies (black) is no more toxic than when Drug/PEG-HCCs is presented to cells with all three antibodies. Protein levels were measured in 7 wells ± SD, only in the CCCP positive control and the untargeted/targeted trident therapy were the HCN protein levels less than the control levels; $p<0.05$, ANOVA and Tukey post-hoc test.

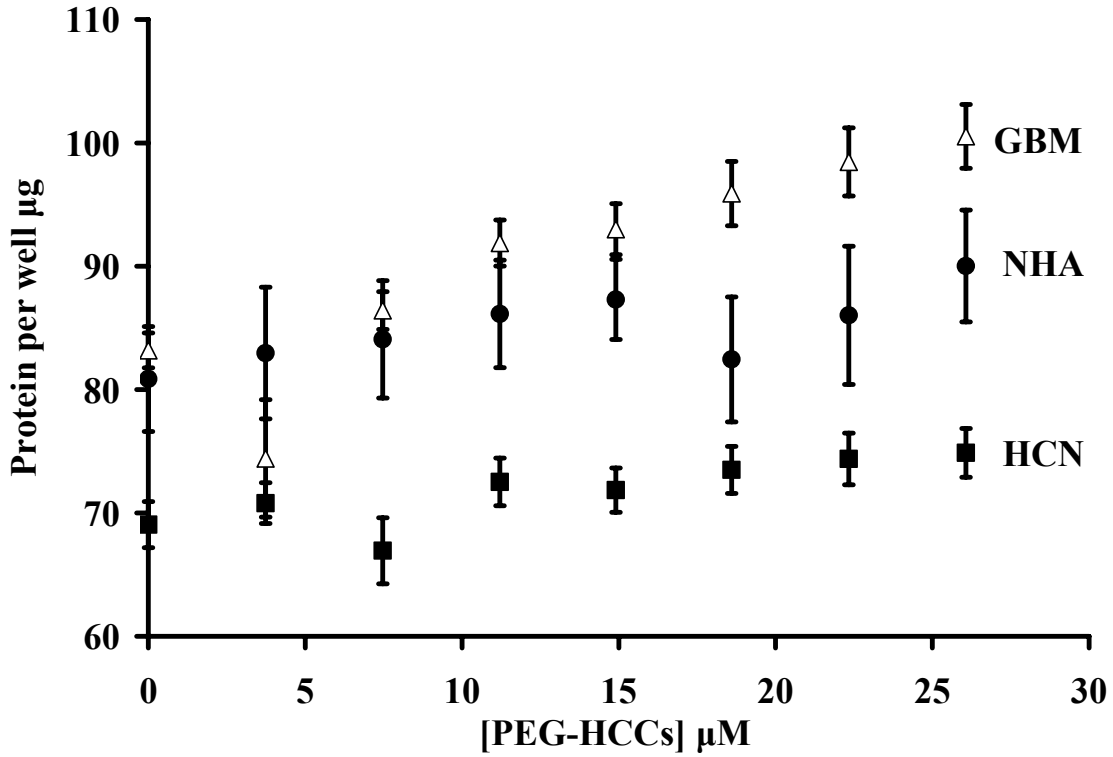

Figure D3. PEG-HCCs are not toxic towards confluent cultures of human cortical neurons (HCN), normal human astrocytes (NHA), and glioblastoma multiforme (GBM) following 24 h exposure to high very concentrations of PEG-HCCs as shown by cell protein levels (n = 8 wells; error bars SD).

A

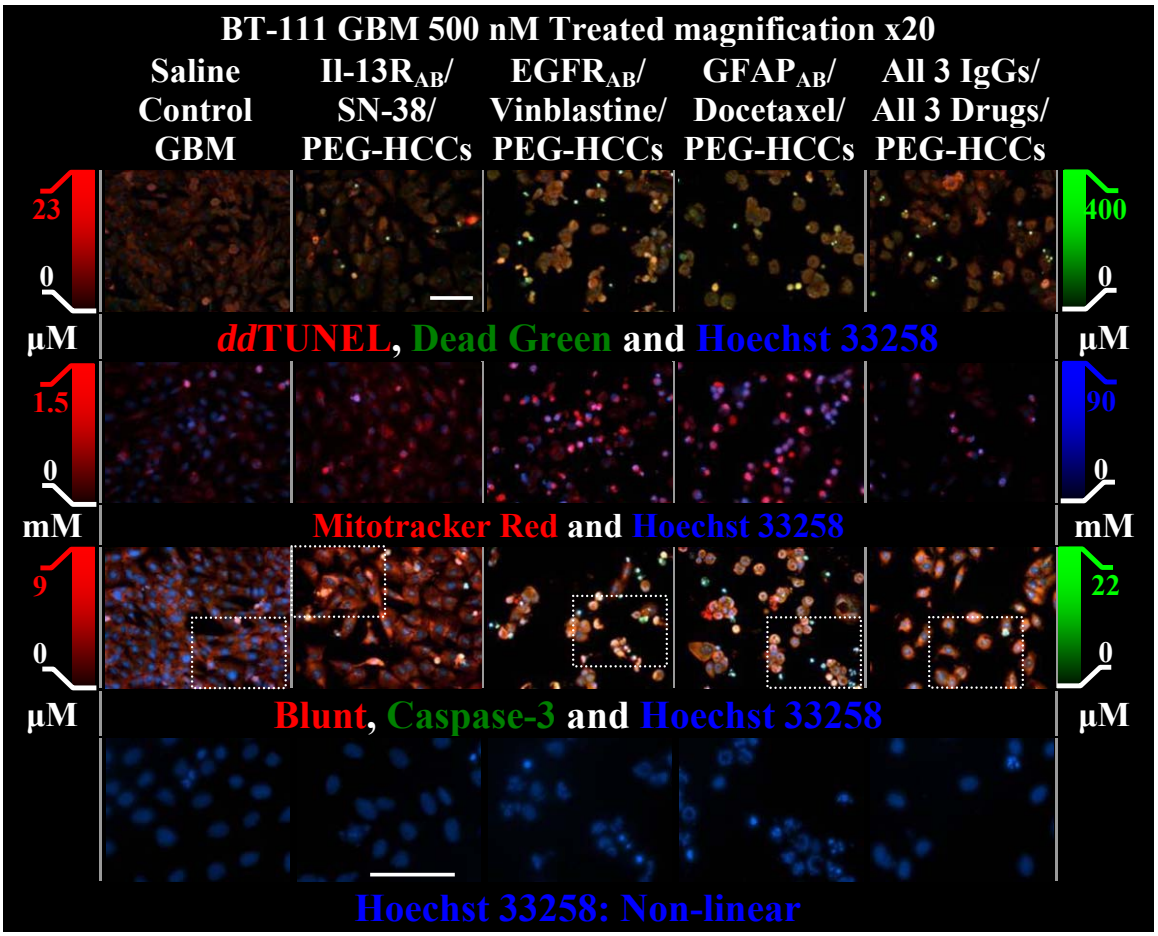
BT-111 GBM 500 nM Treated magnification x20
Saline Control GBM
Il-13R$_{AB}$/ SN-38/ PEG-HCCs
EGFR$_{AB}$/ Vinblastine/ PEG-HCCs
GFAP$_{AB}$/ Docetaxel/ PEG-HCCs
All 3 IgGs/ All 3 Drugs/ PEG-HCCs
23
0
µM
400
0
µM
ddTUNEL, Dead Green and Hoechst 33258
1.5
0
mM
90
0
mM
Mitotracker Red and Hoechst 33258
9
0
µM
22
0
µM
Blunt, Caspase-3 and Hoechst 33258
Hoechst 33258: Non-linear

B

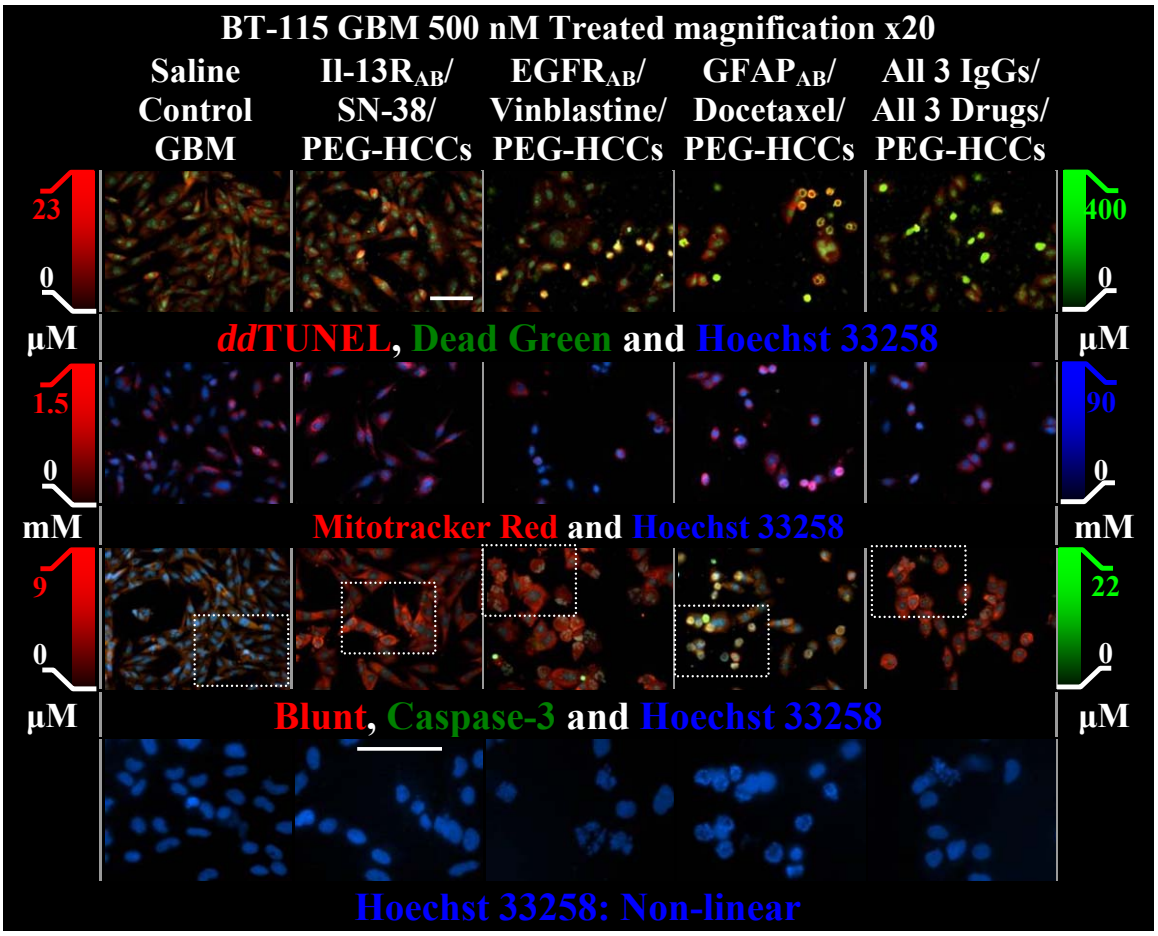
BT-115 GBM 500 nM Treated magnification x20
Saline Control GBM
Il-13R$_{AB}$/ SN-38/ PEG-HCCs
EGFR$_{AB}$/ Vinblastine/ PEG-HCCs
GFAP$_{AB}$/ Docetaxel/ PEG-HCCs
All 3 IgGs/ All 3 Drugs/ PEG-HCCs
23
0
µM
400
0
µM
ddTUNEL, Dead Green and Hoechst 33258
1.5
0
mM
90
0
mM
Mitotracker Red and Hoechst 33258
9
0
µM
22
0
µM
Blunt, Caspase-3 and Hoechst 33258
Hoechst 33258: Non-linear

C

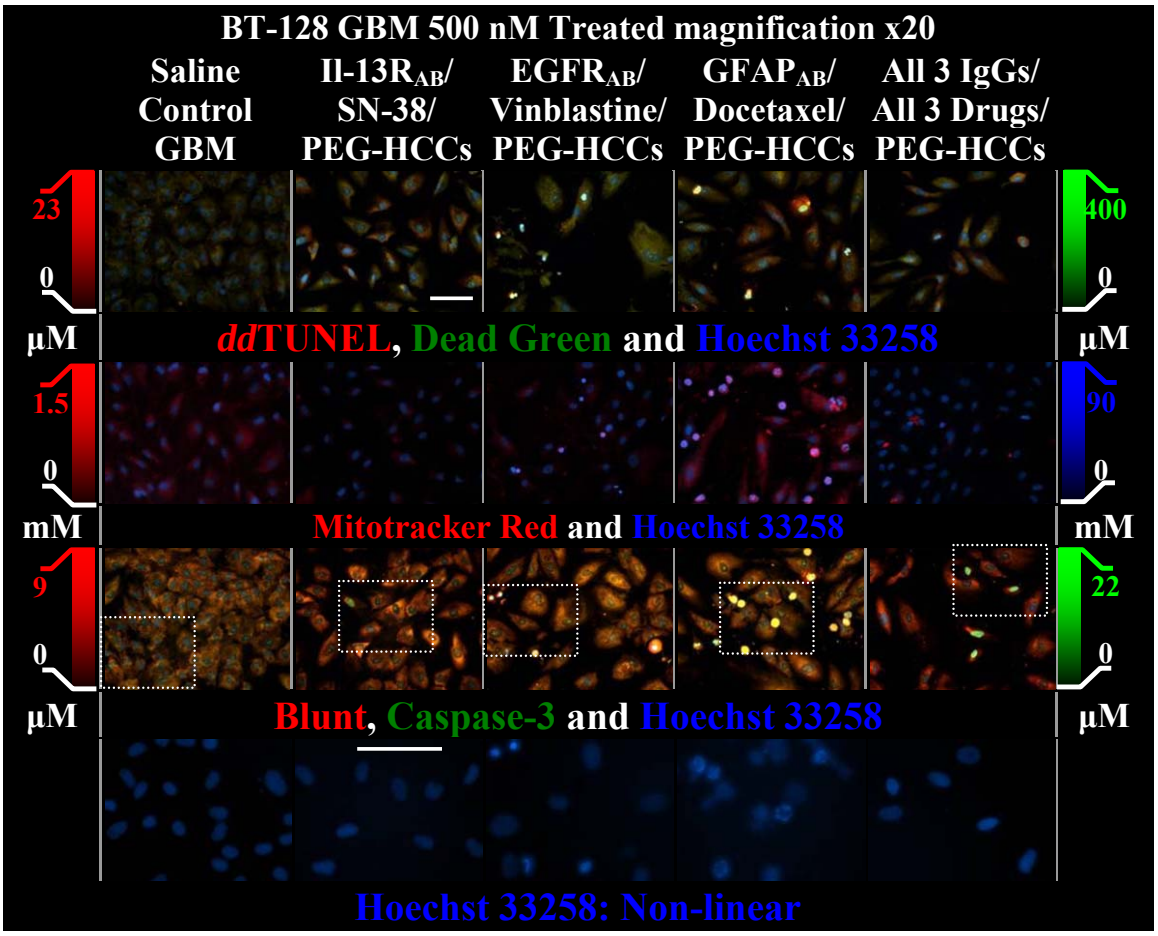
BT-128 GBM 500 nM Treated magnification x20
Saline Control GBM
Il-13R$_{AB}$/ SN-38/ PEG-HCCs
EGFR$_{AB}$/ Vinblastine/ PEG-HCCs
GFAP$_{AB}$/ Docetaxel/ PEG-HCCs
All 3 IgGs/ All 3 Drugs/ PEG-HCCs
23
0
µM
400
0
µM
ddTUNEL, Dead Green and Hoechst 33258
1.5
0
mM
90
0
mM
Mitotracker Red and Hoechst 33258
9
0
µM
22
0
µM
Blunt, Caspase-3 and Hoechst 33258
Hoechst 33258: Non-linear

D

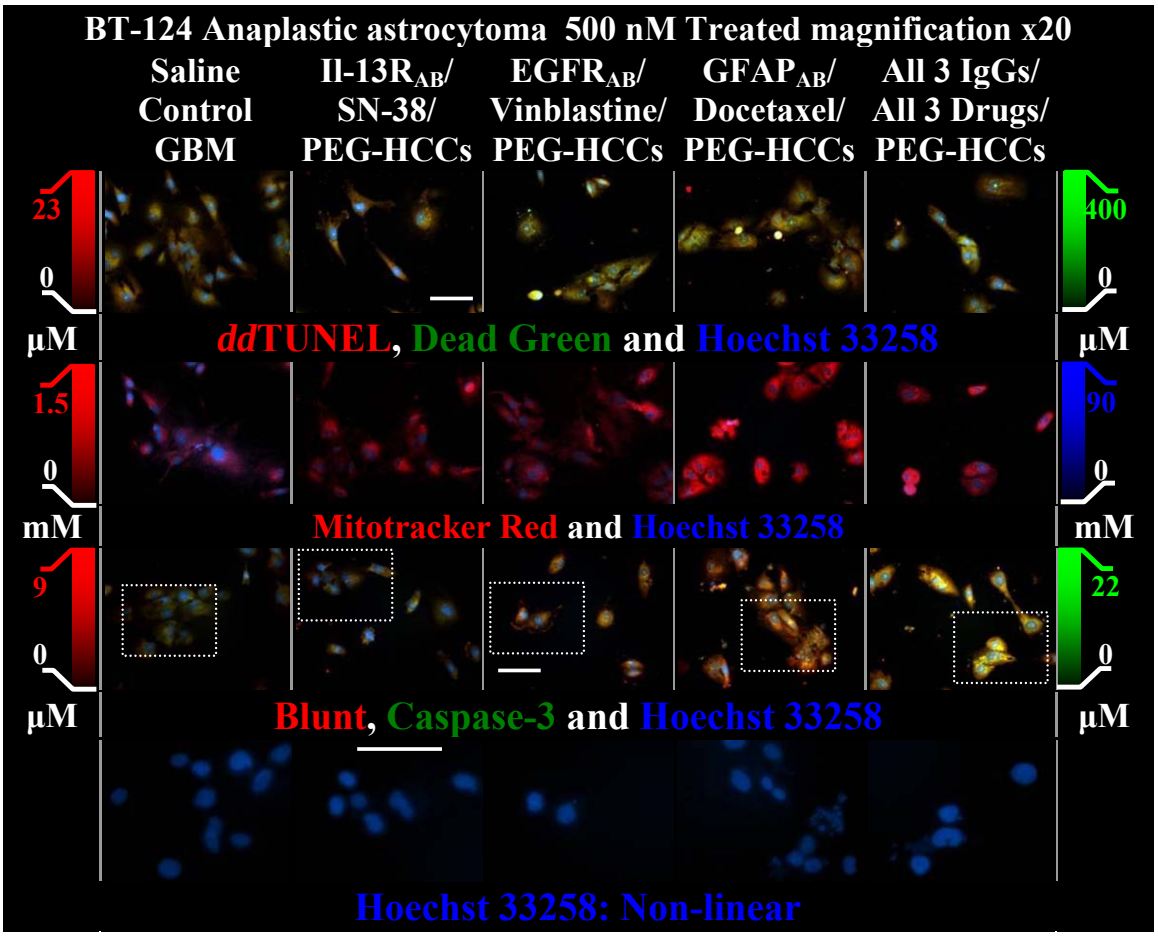
BT-124 Anaplastic astrocytoma 500 nM Treated magnification x20
Saline Control GBM
Il-13R$_{AB}$/ SN-38/ PEG-HCCs
EGFR$_{AB}$/ Vinblastine/ PEG-HCCs
GFAP$_{AB}$/ Docetaxel/ PEG-HCCs
All 3 IgGs/ All 3 Drugs/ PEG-HCCs
23
0
µM
400
0
µM
ddTUNEL, Dead Green and Hoechst 33258
1.5
0
mM
90
0
mM
Mitotracker Red and Hoechst 33258
9
0
µM
22
0
µM
Blunt, Caspase-3 and Hoechst 33258
Hoechst 33258: Non-linear

E

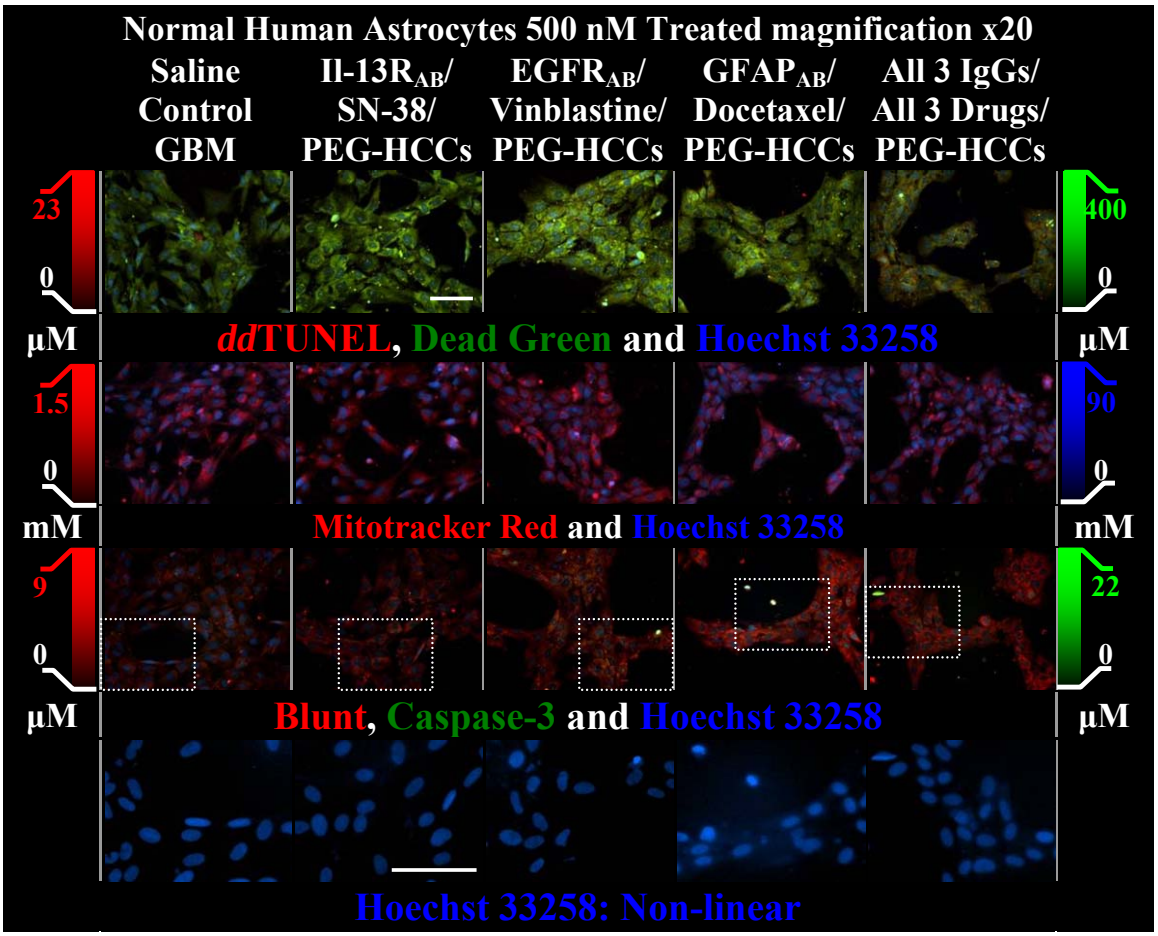
Normal Human Astrocytes 500 nM Treated magnification x20
Saline Control GBM
Il-13R$_{AB}$/ SN-38/ PEG-HCCs
EGFR$_{AB}$/ Vinblastine/ PEG-HCCs
GFAP$_{AB}$/ Docetaxel/ PEG-HCCs
All 3 IgGs/ All 3 Drugs/ PEG-HCCs
23
0
µM
400
0
µM
ddTUNEL, Dead Green and Hoechst 33258
1.5
0
mM
90
0
mM
Mitotracker Red and Hoechst 33258
9
0
µM
22
0
µM
Blunt, Caspase-3 and Hoechst 33258
Hoechst 33258: Non-linear

F

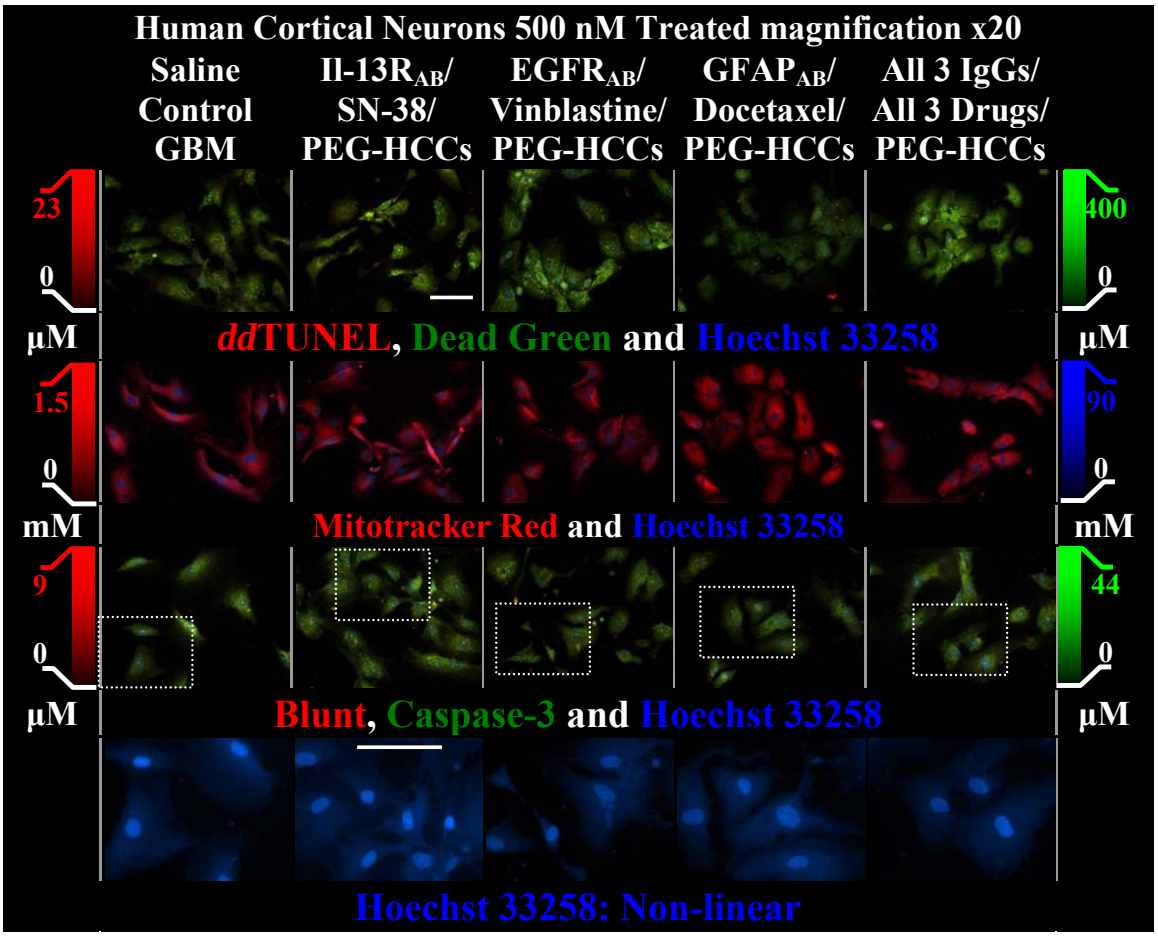

Figure D4. The pattern of cell death in (A-C) three GBMs, (D) one anaplastic astrocytoma, (E) NHA and (F) HCN cell cultures treated as in Figure 4.3. The upper three rows of A-F are all at 20× magnification. However, the bottom row of A-F is expanded further by 4× using a non-linear scale (G = 0.5), showing DNA staining by Hoechst at higher magnification, which allows easier identification of the known outcomes of the microtubule disrupting drugs; Docetaxel (Doc) and Vinblastine (Vin). Mitotic catastrophe

is found using both drugs, with many nuclei having atypical morphology.[2,3] The distorted/cog wheel shaped nuclei, indicative of cell cycle arrest at the G2/M phase, are clearly visible in the Doc treated cancer cells.[4]

References

1. Sharpe, M. A.; Marcano, D. C.; Berlin, J. M.; Widmayer, M. A.; Baskin, D. S.; Tour, J. M. Antibody-targeted nanovectors for the treatment of brain cancers. *ACS Nano*, **2012**, *6*, 3114-3120.
2. Maurya, D.; Ayuzawa, R.; Doi, C.; Troyer, D.; Tamura, M. Topoisomerase I Inhibitor SN-38 effectively attenuates growth of human non-small cell lung cancer cell lines *in vitro* and *in vivo*. *J. Environ. Pathol. Toxicol. Oncol.,* **2011**, *30*, 1-10.
3. Upreti, M.; Lyle, C. S.; Skaug, B.; Du, L.; Chambers, T. C. Vinblastine-induced apoptosis is mediated by discrete alterations in subcellular location, oligomeric structure, and activation status of specific Bcl-2 family members. *J. Biol. Chem.,* **2006**, *281*, 15941-15950.
4. Hoshino, T.; Wilson, C. B.; Muraoka, I. The Stathmo kinetic (mitostatic) effect of vincristine and vinblastine on human gliomas. *Acta Neuropathologica,* **1979**, *47*, 21-25.